December 2020

Surface Alteration in the Ölkelduháls, Nesjavellir, and Geysir Hydrothermal Systems, Iceland: Implications for Mars

Jordan Ludyan
University of Wisconsin-Milwaukee

SURFACE ALTERATION IN THE ÖLKELDUHÁLS, NESJAVELLIR,

AND GEYSIR HYDROTHERMAL SYSTEMS, ICELAND:

IMPLICATIONS FOR MARS

by

Jordan Ludyan

A Thesis Submitted in
Partial Fulfillment of the
Requirements for the Degree of

Master of Science
in Geosciences

at

The University of Wisconsin-Milwaukee
December 2020

ABSTRACT

SURFACE ALTERATION IN THE ÖLKELDUHÁLS, NESJAVELLIR, AND GEYSIR
HYDROTHERMAL SYSTEMS, ICELAND: IMPLICATIONS FOR MARS

by

Jordan Ludyan

The University of Wisconsin – Milwaukee, 2020
Under the Supervision of Dr. Lindsay McHenry

Silica- and sulfate-rich deposits observed by Mars Exploration Rover (MER) Spirit near Home Plate, Gusev crater, Mars, indicate alteration of Mars basalt by a diverse array of hydrothermal fluids and processes. Constraining the precise fluid conditions present at the time of deposition for these deposits on Mars relies on investigations of terrestrial hydrothermal systems that produce similar mineral assemblages. Alteration products and fluids collected from the Ölkelduháls, Nesjavellir, and Geysir hydrothermal areas in southern Iceland cover a wide range of end-member and intermediate fluid and alteration environments, and provide a means to compare the secondary minerals produced from different hydrothermal processes. Altered sediments, precipitates, and thermal fluids were collected from hot springs with pH ranging from 2.15 – 8.70 and one active fumarole and analyzed for their geochemical and mineral composition. Pyrite was abundant throughout all three field sites indicating highly reducing conditions up to very shallow depths. Phyllosilicates were dominated by smectite and kaolinite, and smectite was associated with both acidic and alkaline hot springs, demonstrating that its formation may not be impeded by acidic conditions. Patterns of enrichment in leached rocks indicate that TiO_2 and Zr follow a nearly linear trend of residual accumulation in rocks subjected to acidic fluids, consistent with their low solubility. This relationship was used to assess the behavior of trace elements in altered solids. Vanadium and Cr were found to be most resistant to acid leaching, with other elements likely incorporated into secondary minerals that could lead to depletion or enrichment depending on the mineral assemblage. In surface waters, Mg, Fe, Al, Ca, Mn, Cr, Ni, Ti, V, and Zr were found to be mobile only at very low pH, with a downward exponential trend at pH > 3. Chloride, K, Na, Ge, B, As, and Rb displayed the opposite trend and were scavenged from rocks at depth and incorporated into neutral to alkaline hot springs at the surface. These results support the findings of other studies indicating that the sulfur-rich Paso Robles class soils observed by MER Spirit near Home Plate, Gusev crater likely formed through fumarolic processes. The extensive diagenetic maturation and advanced alteration observed in Iceland in relatively young (~ 10,000 yrs) hydrothermal deposits has implications for the length of time hydrothermal processes may have been active near Home Plate, Mars, where evidence of diagenetic maturation and long-term accumulation of alteration products is minimal.

TABLE OF CONTENTS

LIST OF FIGURES

LIST OF TABLES

ACKNOWLEDGEMENTS

1. Introduction

Hydrothermal systems have been present on the Earth's surface since the crust stabilized and are thought to have existed on the surface of Mars throughout the Noachian (>3.7 Ga) and possibly well into the Hesperian (3.0 – 3.7 Ga). On Mars, orbital evidence indicates a heavily bombarded and volcanically active early planetary surface that preserves evidence of surface and/or subsurface water, suggesting that hydrothermal alteration was once widespread. Accordingly, mineral and geochemical evidence of hydrothermal alteration is distributed across the surface at both orbital- and rover-scale. Understanding the nature of hydrothermal alteration products on Mars has astrobiological implications, as such environments provide zones of localized habitability (heat source and microbially exploitable energy gradient) and a means of preservation (rapid mineralization and subsequent micro- and macrofossil preservation; e.g. Jones and Renaut 2003; Mountain et al. 2003; Tobler et al. 2008; Tobler and Benning 2011; Djokic et al. 2017; McMahon et al. 2018) on/in an otherwise potentially inhospitable planetary surface/interior.

Due to the complexity of hydrothermal processes and the limitations of orbital and rover instrumentation, studies of terrestrial hydrothermal systems are useful for testing hypotheses regarding the aqueous alteration history of Martian deposits. Terrestrial magmatic hydrothermal systems are characterized by a variety of surface environments, ranging from hyper-acid hot springs and fumaroles that leach soluble phases from host rocks, to neutral/alkaline hot springs actively precipitating silica (as sinter) or carbonate (as travertine). Both end-member hydrothermal environments are known to host thermophilic chemolithotrophic life in terrestrial systems, although phylogenetic diversity and microbial abundance is significantly more

restricted in acidic surface hydrothermal systems (Marteinsson et al. 2001; Tobler and Benning 2011; Cockell et al. 2019). Conversely, Tobler et al. (2008) note that dilute, sinter-depositing alkaline hot springs host robust chemolithotrophic communities, and that the slow but consistent rate of silica precipitation in such systems often leads to complete entombment of microbial structures in sinters (e.g. bacillus, cocci, filaments). Such observations highlight the significance of differentiating these deposits to assess past habitability on the surface of Mars.

On Earth, surface hydrothermal systems are the expression of deep aquifer fluids that have undergone boiling and phase segregation during upflow. As magmatically heated aquifer fluids convectively rise and begin to boil, volatile phases including H_2S, CO_2, and minor H_2 are partitioned into steam. The residual boiled and gas-depleted thermal fluids are then free to ascend along permeable subsurface zones and may eventually emerge as neutral to alkaline hot springs that can be variably mixed with meteoric water (Markússon and Stefánsson 2011; Scott et al. 2014; Ingebritsen et al. 2016). The volatile-rich steam segregated from the boiling process will also ascend towards the surface, where it may mix with oxygenated shallow ground and/or meteoric water. The result is oxidation of H_2S to H_2SO_4 which supplies a continuous flux of protons to the fluid and drives host rock dissolution, liberating metals into solution. Alternatively, the segregated steam fraction may emerge at the surface directly, forming fumaroles. In either case, previous investigations of terrestrial hydrothermal environments indicate that these two end-member processes yield distinct but overlapping mineralogical and geochemical signatures (e.g. Pirajno 2010; Hynek et al. 2013, McCollom et al. 2013; Björke et al. 2015; Rodríguez and van Bergen 2015; McHenry et al. 2017 and many others).

To better understand the processes controlling deposition of minerals in terrestrial and inferred Martian hydrothermal systems, the goals of this research are to: (1) quantify elemental

compositions and mineral assemblages of hydrothermal alteration products and fluids collected in August, 2019 during field work in southern Iceland through detailed geochemical analysis; (2) determine the geochemical indicators best suited for assessing aqueous conditions (e.g. fumarolic leaching vs. precipitation from near-neutral fluids) at the time of deposition by linking the elemental compositions and mineral assemblages of alteration products with associated fluids; and (3) use these findings to develop a conceptual model that accounts for the observations and builds upon the framework for interpreting alteration histories on the Martian surface based on geochemical/mineral composition. The results of this study will refine our understanding of aqueously-derived deposits on Mars and aid future terrestrial studies of hydrothermal systems, while also offering the first detailed integrated mineral and geochemical investigation of surface alteration in the Ölkelduháls hydrothermal system and building upon previous work at Nesjavellir and Geysir.

2. Mars: geologic context & relevant observations

Interpreting ancient Mars environmental conditions and assessing the past habitability of those environments is a key goal of any Mars orbiter or rover mission. Remote sensing data provided by the Observatoire pour la Mineralogie, l'Eau, les Glaces et l'Activité (OMEGA) instrument and the Compact Reconnaissance Imaging Spectrometer for Mars (CRISM) instrument on board the Mars Express and Mars Reconnaissance Orbiter (MRO), respectively, indicate globally dispersed sulfates, Fe/Mg smectites, and Al-phyllosilicates across the predominantly basaltic crust, implying aqueous alteration (Schulze-Makuch et al. 2007; Bishop et al. 2013; Ehlmann and Edwards 2014). Morphological evidence of surface water is also widespread and includes interconnected valley and drainage networks (Craddock and Howard 2002; Irwin et al. 2002; Hynek et al. 2010), paleolake basins (Fassett and Head 2008; Goudge et

al. 2016), and fan deltas (Goudge et al. 2015, 2017; Hynek 2016). Crater dating constraints on lava flow and caldera ages indicate that major Martian igneous provinces were largely in place by the end of the Noachian period, concurrent with a 'wet' Mars (Schulze-Majuch et al., 2007; Robbins, 2011). Accordingly, numerous studies have tentatively identified hydrothermally-derived alteration products at orbital scales (e.g. Schulze-Makuch et al. 2007; Skok et al. 2010; Weitz et al. 2014; Singh et al. 2019). However, conclusive identification of relict hydrothermal systems using remote sensing is challenging. Hydrothermal alteration products form intimate mixtures of minerals that can vary at cm-scales. The highest resolution orbital mineralogical datasets provided by CRISM spectra are constrained to ~20 m/pixel, making such mineral assemblages difficult or impossible to resolve.

2.1 Possible Martian hydrothermal activity

2.1.1 Home Plate, Gusev crater

Considering the limits of orbital datasets, identification and interpretation of relict hydrothermal activity on Mars relies primarily on rover instrumentation coupled with terrestrial analog and experimental studies. In 2006-2007, Mars Exploration Rover (MER) Spirit explored what is now widely believed to be a relict hydrothermal system near Columbia Hills, Gusev crater associated with a pyroclastic deposit dubbed 'Home Plate' (Figure 1A; Squyres et al. 2008; Yen et al. 2008; Ruff et al. 2011; Ruff and Farmer 2016). Alpha Particle X-ray Spectrometer (APXS) and Mössbauer spectroscopic data from rocks and soils analyzed by Spirit indicate marked enrichment of silica ($\geq$ 90 wt. %), Ti, Cr, and Zn relative to typical unaltered basaltic soils, near ferric Fe-, Mg-, and possible Ca-sulfates (Figure 1B-D; Yen et al. 2008). These geochemical and mineralogical data, along with spectral signatures consistent with opal-

A, represent robust evidence of hydrothermal alteration (Squyres et al. 2007, 2008; Morris et al. 2008; Yen et al. 2008; Ruff et al. 2011). The exact nature of the fluids that produced the deposits observed by Spirit, however, remains unclear. Squyres et al. (2008) note that enrichment of Si and Ti near sulfates is consistent with acidic alteration and residual enrichment of insoluble phases under limited water/rock ratios (i.e. fumarolic alteration) while Ruff and Farmer (2015) and Ruff et al. (2020) argue that the spongy, nodular appearance and spectral signature of opal-A observed by Spirit very closely match silica precipitates (sinter) associated with a near-neutral terrestrial hydrothermal system in Chile, indicating high water/rock ratios and less intensive alteration.
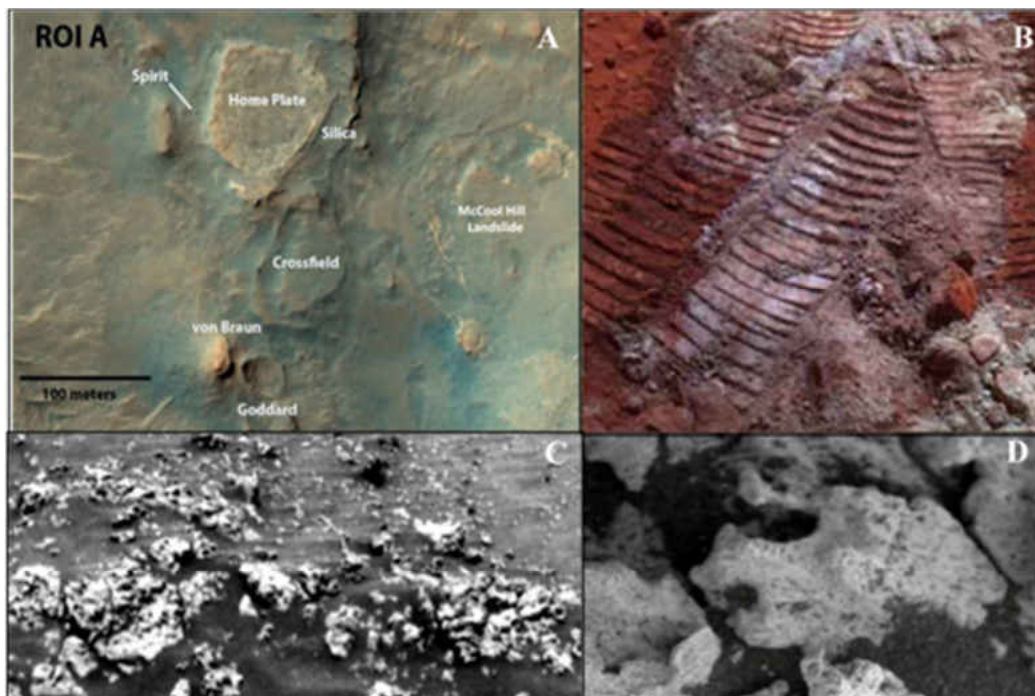
Figure 1: Home Plate, Gusev crater, Mars, and associated outcrops investigated by MER Spirit in 2007-2008. (a) Orbital image of Home Plate, a pyroclastic feature adjacent to silica-rich deposits interpreted as evidence of hydrothermal alteration; (b) sulfate-rich 'Paso Robles' class soils just underneath red surface dust, revealed by Spirit's broken wheel and considered as evidence of fumarolic leaching; (c) composite image of silica-rich outcrop 'Elizabeth Mahon' containing light opal-A nodules; (d) Microscopic Imager (MI) closeup of opal-A digitate nodules exhibiting spongy, sinter-like texture, interpreted as evidence of neutral to alkaline hydrothermal fluids. All images provided by NASA JPL.

Ruff et al. (2020) point out that the coexistence of S-rich soils linked to solfataric processes and sinter deposits associated with neutral to alkaline hot spring fluids is common in terrestrial hydrothermal environments, and suggest that the hydrothermal system associated with

Figure 2: Pancam false-color image of Pioneer mound, considered a candidate hot spring vent mound ~ 50 m west of Eastern Valley adjacent to Home Plate, Gusev crater. Spectral signatures are most consistent with the presence of opal-A, although the target was not reached before MER Spirit became stuck in the Martian sand. Image from Ruff et al. (2019).

Home Plate on Mars may represent a manifestation of both processes. Observations in other recent studies also suggest that both acid leaching and silica precipitating environments may have coexisted near Home Plate. Yen et al. (2019) plotted Si/Ti ratios against Si seen in altered samples from the area finding that one subset of samples maintained relatively constant Si/Ti ratios despite increasing Si concentrations, consistent with residual accumulation of both species via acid leaching. Other Si-rich rocks followed a dilution trend more consistent with silica precipitates (i.e., sinter) added to a host rock.

Ruff et al. (2020) also identified another candidate hydrothermal target based on updated panoramic camera (Pancam) and miniature thermal emission spectrometer (Mini-TES) dust spectra corrections, dubbed Pioneer Mound (Figure 2). This feature is an ~ 2 m high mound <50 m west of Home Plate which displays spectra consistent with the presence of opal-A variably contaminated with basaltic sand. Ruff et al. (2020) propose that this feature's geomorphology along with its opal-A composition imply an extinct hot spring vent. These observations

strengthen the interpretation that the hydrothermal system associated with Home Plate hosted diverse aqueous environments.

2.1.2 Gale crater

Although Gale crater is considered to have been primarily modified through sedimentary/diagenetic processes, mounting evidence points to possible high temperature/hydrothermal alteration dispersed throughout the area. Curiosity has explored variably altered sedimentary deposits through its traverse of Gale crater and Aeolis Mons (informally dubbed Mount Sharp), widely thought to represent a post-impact lacustrine/fluvial-deltaic system (Grotzinger et al. 2015; Rice et al. 2017). Throughout the mission APXS measurements indicate variable enrichments of Zn, Ge, and in some cases Cu in diverse host-rocks such as sandstones, mudstones, and Ca-sulfate veins. On Earth, Zn, Ge, and Cu are mobile in high temperature fluids, and are therefore concentrated near the surface via removal from primary silicates by hydrothermal processes (Arnórsson 1984; Wood and Samson 2006; Yang et al. 2015; George et al. 2016). These observations indicate multiple episodes of aqueous alteration: initial enrichment at the source area via hydrothermal fluids and host-rock dissolution, followed by dissemination and transport by diagenetic fluids (Berger et al. 2017; Yen et al. 2017).

Additional support for hydrothermal processes at Gale crater has been provided by recent studies. Morris et al. (2020) note that accumulations of high sanidine (adularia) as observed in drill sample 'Windjana' near nanophase Fe-oxide/oxyhydroxide (npOx) and phyllosilicate deposits in the Gale crater plains closely match mineral assemblages seen near the summit of Mauna Kea volcano, HI. The Mauna Kea deposits formed through alteration of basaltic precursor rocks through high temperature (250 – 400°C) hydrothermal processes. As with trace

metal enrichments at Gale crater, however, such deposits are dispersed heterogeneously and have not been linked to a single hydrothermal system.

2.2 Future Mars missions

Understanding the distribution of elements and minerals in terrestrial hydrothermal systems will prove useful on future Mars missions. In particular, the micro-XRF instrument PIXL (Planetary Instrument for X-ray Lithochemistry; housed on NASA's Perseverance rover) will allow spatial mapping of elements at < 0.1 wt. % abundance, providing unprecedented high-resolution trace element data at the Martian surface (Allwood et al. 2015; Heirweigh et al. 2018). Additionally, a Raman laser spectrometer system and laser-induced breakdown spectrometer (LIBS) will be included on ESA's ExoMars rover (to be launched in 2021) along with an x-ray diffractometer (XRD), allowing high-resolution geochemical and mineral characterization of aqueously-derived deposits at the Martian surface (Veneranda et al. 2020).

3. Geologic setting – Iceland

3.1 Petrologic conceptual model

Iceland's unique geology is a result of the interaction between the Mid-Atlantic Ridge (MAR) and the Icelandic Mantle Plume. Eastward migration of the mantle plume relative to the Eurasian/North American Plate boundary has led to a complex volcano-stratigraphic sequence along the MAR axis, where crustal thinning drives the plastic asthenosphere towards the surface and resultant partial melting leads to magma recharge. The MAR remains relatively narrow until it reaches Iceland along the Reykjanes Ridge, where the deformation zone becomes much wider and more complex, attributed to the presence of the Icelandic Mantle Plume (Wolfe et al. 1997). There are two major generally NE-SW trending active volcanic belts within Iceland, with magma

8

fed into individual volcanic centers via fissure and fault swarms trending perpendicular to the lithospheric spreading axis (Beblo and Bjornsson 1980; Arnórsson 1995a; Wolfe et al. 1997). Numerous individual volcanic zones have been defined based on the interaction between the volcanic belts; all hydrothermal systems sampled herein lie in the Western Volcanic Zone (WVZ; Einarsson 2008).

3.2 Icelandic hydrothermal systems
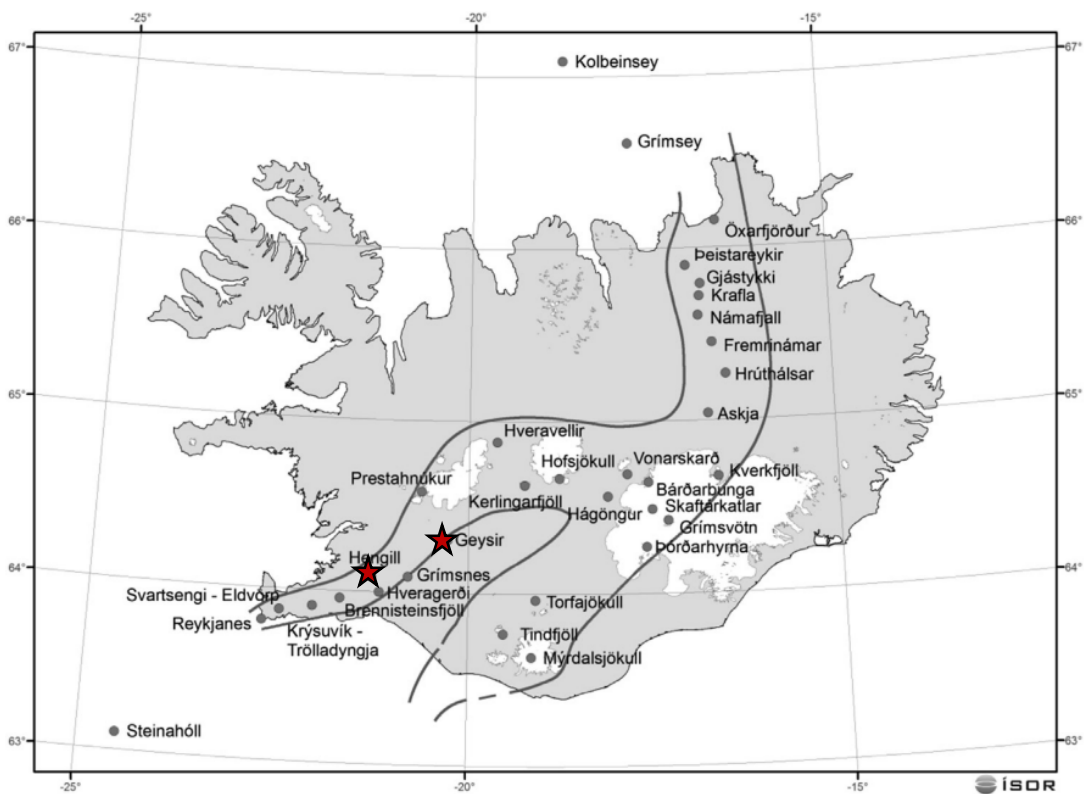
Figure 3: Distribution of Icelandic thermal areas. Only high temperature areas are indicated, all falling directly along the MAR spreading axis. Hengill (Nesjavellir and Ölkelduháls) and Geysir areas are starred. Modified from Ármannsson (2016).

Hydrothermal systems in Iceland are associated with individual volcanic complexes and are typically classified as either high-temperature (aquifer fluids > ~150°C) or low-temperature (aquifer fluids < ~100°C) (e.g. Arnórsson 1995a, 1995b; Markússon and Stefánsson 2011;

Stefánsson et al. 2016). As hydrothermal fluids dissolve soluble phases from host rocks the system tends to become cooler and less active because the residual alteration products and precipitates are generally more impermeable than the unaltered rocks. However, fresh pulses of magma in the subsurface can lead to instantaneous changes in permeability, renewing the vigor of the system and rapidly changing the expression of thermal features at the surface (Ingebritsen et al. 2010). Nevertheless, spreading along the MAR axis concentrates the youngest and highest-temperature hydrothermal systems on-axis in Pleistocene/Holocene volcanic deposits, with increasingly mature and lower-temperature systems occurring further off-axis within fractured and highly altered Tertiary lava sequences (Arnórsson 1995b; Zakharova and Spichak 2012). The general distribution of Icelandic hydrothermal areas is provided in Figure 3.

3.3 Hydrothermal fluid chemistry and characteristics

Geothermal aquifer chemistry is considered to be predominantly controlled via approximate fluid-mineral equilibrium with respect to most major elements during upflow, excluding mobile phases (e.g. chlorine/boron), and this assumption has been shown to be valid in numerous studies (e.g. Arnórsson et al. 1995 *and references therein*). However, rapidly changing conditions near the surface disrupt this equilibrium, leading to mineral precipitation and rock dissolution. Accordingly, surface geothermal waters are classified with respect to major element geochemistry and origin. Common classifications include boiled alkaline waters, steam-heated acid waters, and steam-heated neutral waters (Kaasalainen and Stefánsson 2011; Björke et al. 2015; Stefánsson et al. 2016). Boiled alkaline waters are considered to represent residual, degassed aquifer fluids that flow to the surface along zones of high permeability and have undergone mixing with low-temperature aquifer fluids during upflow. These waters are

characterized mineralogically by deposition of silica sinters and/or travertine and are often accompanied by surficial microbial/algal mats.

Steam-heated acid waters represent the volatile-rich steam fraction (predominantly H_2S, CO_2, H_2; Stefánsson, 2017) partitioned from boiled aquifer fluids. Upon ascent and mixing with oxygenated meteoric water, the steam fraction oxidizes and deprotonates, leading to low-pH hot springs and mud pots that dissolve host rocks (which act as a proton-consuming base) and generate zones of intense surface alteration. Alternatively, the steam fraction can discharge directly at the surface (forming fumaroles) where vapor condensation can also drive rock dissolution (via oxidation of H_2S) and sulfur deposition. The mineral assemblages of steam-heated systems vary depending on the extent of alteration, host rock geochemical composition, and whether the system is overprinting previous alteration episodes, but are characterized by intensive host-rock leaching (residually enriching immobile elements [e.g., silicon and Ti]) and deposition of sulfides (below the oxidation front), npOx, and sulfates (above the oxidation front) along with phyllosilicates (e.g. Markússon and Stefánsson 2011; McHenry et al. 2017).

Steam-heated mixed waters also represent magmatic steam mixed with meteoric fluids, but generally with lower proportions of magmatic steam. Geochemically, they are characterized by less acidic conditions (pH ~ 4 - 7) and lower temperatures (~50-80°C). Nevertheless, their mineralogical output is controlled by acid-leaching and H_2S oxidation. Fumarolic, steam-heated acid, and steam-heated mixed surface alteration can therefore be considered along a spectrum of increasingly intense surface alteration controlled by steam/water ratio, and not necessarily as end-member processes. A general conceptual model is shown in Figure 4 that demonstrates the formation of different surface hydrothermal features, such as those in Iceland.
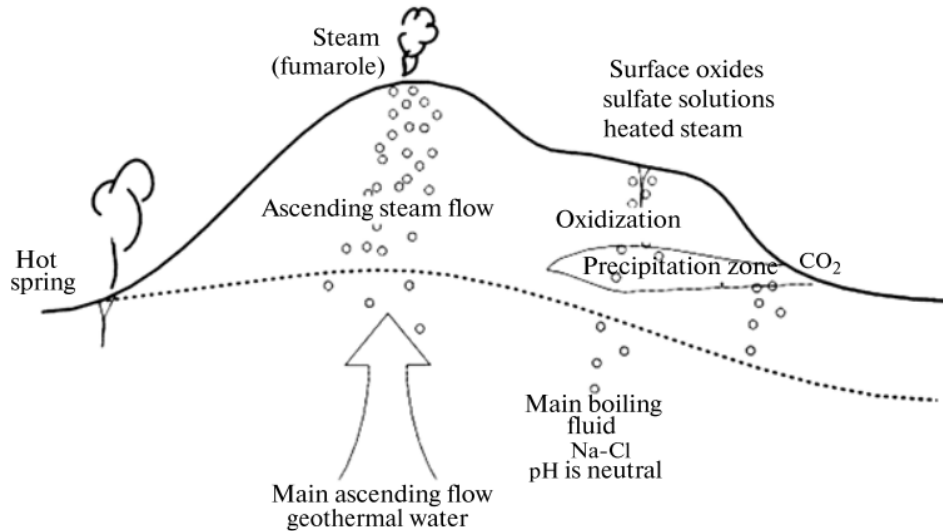
Figure 4: Conceptual model demonstrating formation of surface hydrothermal features, such as those seen in Iceland. The overall expression of the hydrothermal system is governed by boiling and phase separation of volatile-rich, heated aquifer water and mixing/oxidation of volcanic vapors in the subsurface. Figure from Zakharova and Spichak (2012).

3.4 Study areas

3.4.1 Geysir hydrothermal system

The Geysir hydrothermal system is in southern Iceland, adjacent to the Laugarfjall rhyolite dome (Figure 5). The system is actively altering a lower series of rhyolites overlain by more recent basalt, and is thought to be a relatively mature system overprinting previous alteration episodes (Ármannsson 2016). The Icelandic word 'geysir' translates to 'gusher' or 'one who rages,' and is the origin of the English transformation of the term (geyser), to which other features worldwide owe their name. The Geysir geyser itself erupts relatively infrequently, and the nearby Strokkur geyser is much more consistent, erupting a few times per hour. However, the area also hosts numerous hot spring pools with a range of chemical properties, from turbid acid sulfate pools and fumaroles to more neutral/alkaline surface features (Jones et

al. 2007; Ármannsson 2016; Geilert et al. 2016). Most thermal activity is confined to an area of ~ 1 km^2. The diversity of the Geysir system provides a unique opportunity to compare alteration products and fluids produced via distinct alteration styles on a comparable spatial scale to that of Home Plate, Gusev crater, Mars (described in section 2), however, the evolved rhyolitic composition of some of the substrate and maturity of the Geysir hydrothermal system contrast with the likely short-lived nature of hydrothermal alteration near Home Plate on a predominantly basaltic Martian surface.
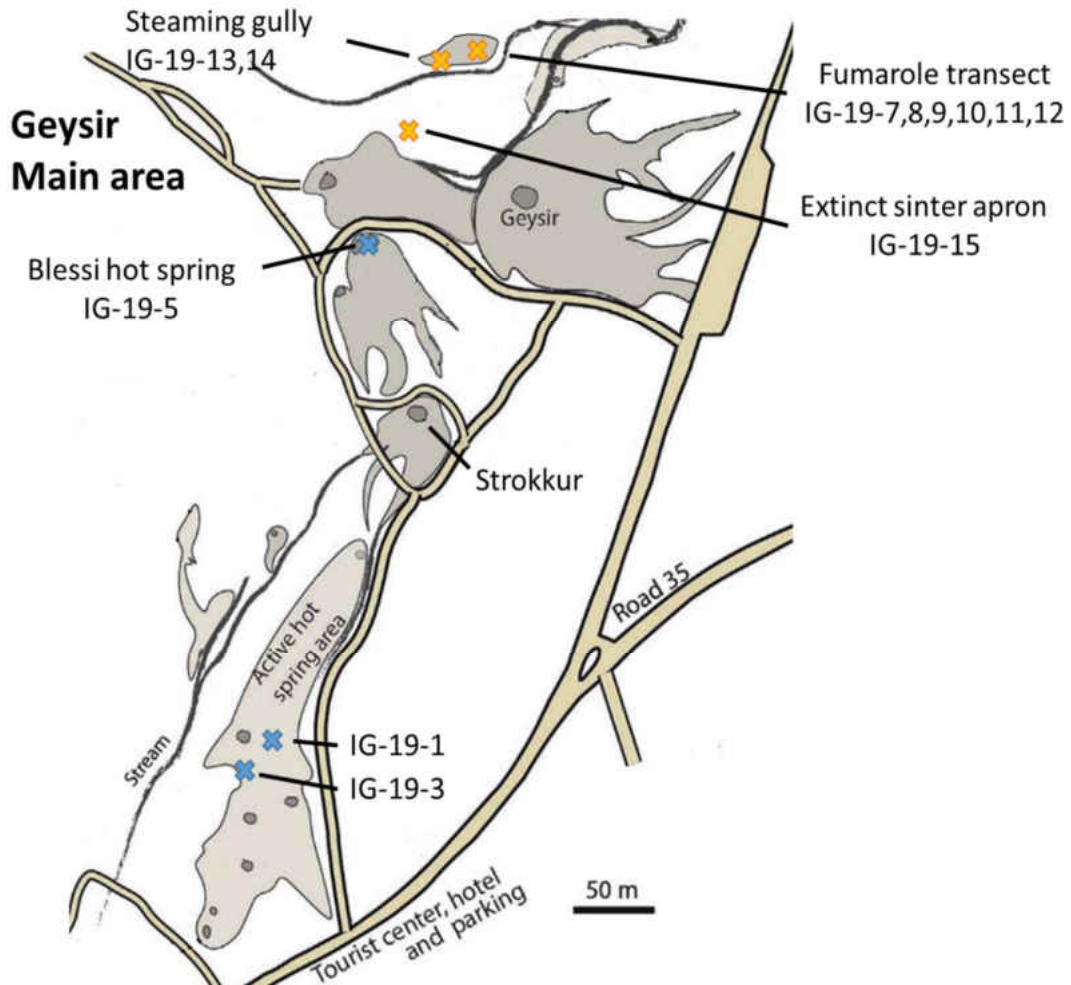
Figure 5: Main Geysir geothermal area indicating distribution of thermal features investigated. Blue X's indicate location of sampled hot springs, and yellow X's indicate sampled solids not associated with an active surface fluid source. North is up. Figure adapted from Kaasalainen et al. (2017).

3.4.2 Hengill Volcanic System (HVS)

The Hengill Volcanic System (HVS) sits upon a triple junction of obliquely twisting crustal blocks extending along the Reykjanes Ridge, where the MAR splits into the two major volcanic belts continuing northeast through Iceland. Hengill itself is the youngest of three volcanoes in the HVS and is considered presently active.
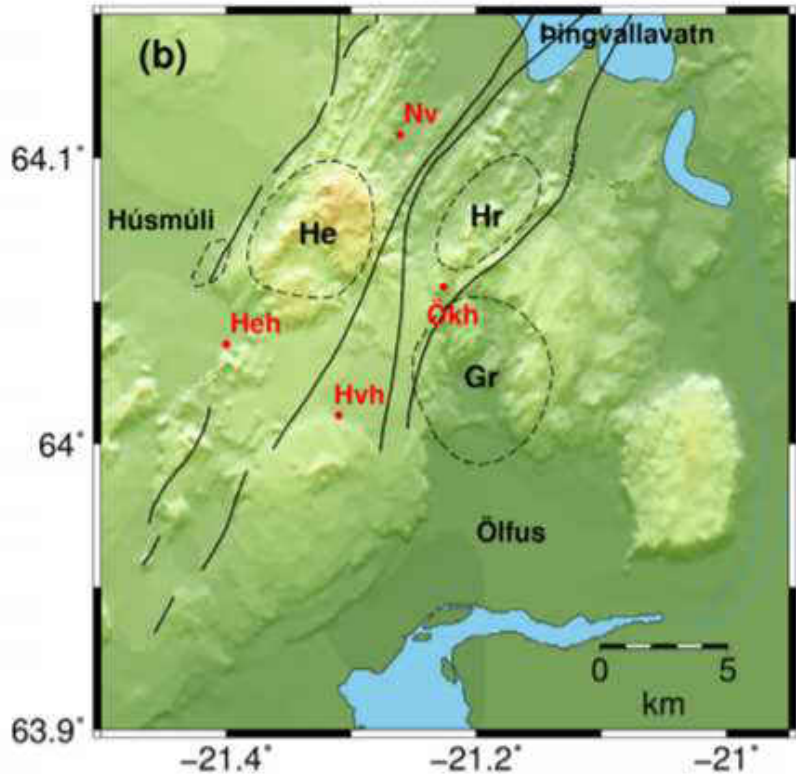
Figure 6: Regional map of the Hengill area. He = Hengill, Hr = Hrómundartindur, Gr = Grensdalur. Hydrothermal areas abbreviated in red; Heh = Hellisheidi, Hvh = Hverahlíd, Nv = Nesjavellir, Ökh = Ölkelduháls. Modified from Jousset et al (2011).

Hrómundartindur lies east of Hengill, with lava flows dating most recently to ~115,000 years. Grensdalur, the oldest volcano, lies the furthest east off the volcanic belt and was active ~300,000 years ago (Ármannsson 2016). Presently, the most intense alteration is associated directly with Hengill itself, with increasingly mature aquifer fluids and less intense alteration eastward towards Hrómundartindur and eventually Grensdalur (Natukunda 2005; Lugaizi 2011).

The HVS hosts four main geothermal areas: Nesjavellir, Hellisheidi, and Hverahlíd (all associated directly with Hengill), and Ölkelduháls (situated on the flanks of Hrómundartindur). All four sites have been thoroughly explored for their production potential, and Nesjavellir and Hellisheidi are currently in production. Exploration and production wells are dotted throughout

the HVS and the subsurface geology and aquifer chemistry is considered to be well understood, especially at Nesjavellir and Hellisheidi (e.g. Arnason et al. 1969; Marty et al. 1991; Jousset et al. 2011; Zakharova and Spichak 2012; Scott et al. 2014; Ármannsson 2016). Hellisheidi and Hverahlíd are not considered in this contribution. A regional map of the Hengill area is provided in Figure 6.

3.4.2.1 Nesjavellir hydrothermal system, HVS

The Nesjavellir hydrothermal system is a high-temperature system situated on the northern flanks of Hengill and is associated with a NE/SW-trending system of faults and fissures, forming a graben structure along the volcanic axis (Figure 6). Geothermal activity is predominantly concentrated along the eastern side of the graben, aligned with Hengill itself, and extends up the mountainside to the south. Host lavas consist of Pleistocene interglacial basalts and subglacial hyaloclastites crosscut by intrusives at variable depth (Arnason et al. 1969; Ármannsson 2016). The carbonate-rich aquifer waters at Nesjavellir reach temperatures exceeding 380°C at 1-1.5 km depth, and have been considered in numerous studies (e.g. Arnason et al. 1969; Zakharova and Spichak 2012; Scott et al. 2014; Ármannsson 2016 and many others). Surface hydrothermal features are variable but are predominantly acid-sulfate. There is one subalkaline CO_3^{2-}-rich hot spring actively precipitating travertine at the south end of the system, likely a surface expression of the deep aquifer fluids circulating at Nesjavellir. This spring was sampled but is excluded from the present contribution. A map of the areas sampled at Nesjavellir is shown in Figure 7.
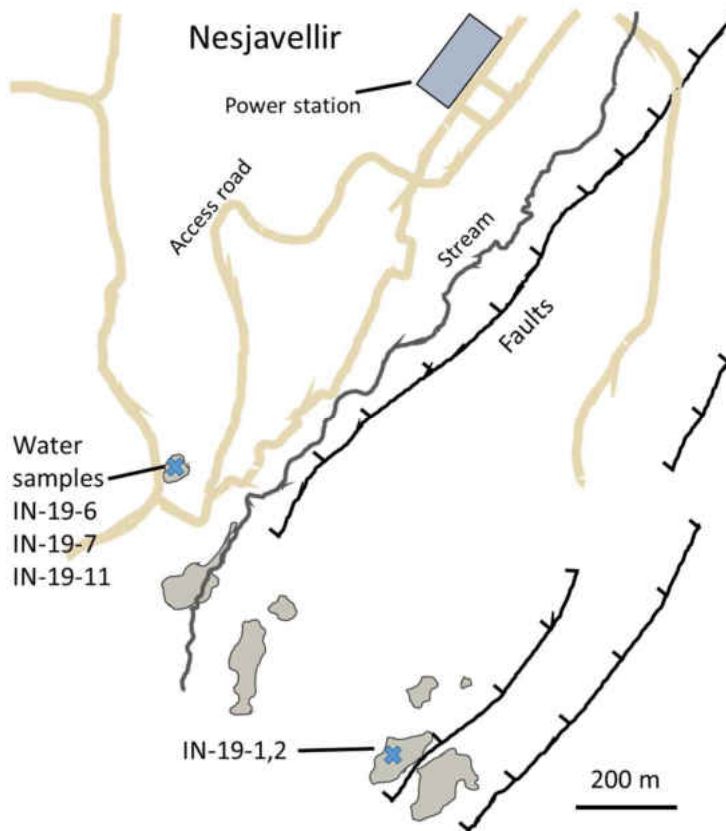
Figure 7: The Nesjavellir geothermal area. Relative location of water samples is indicated. Grey areas represent surface hydrothermal areas. North is up.

3.4.2.2 Ölkelduháls hydrothermal system, HVS

Ölkelduháls is also dominated by relatively acidic alteration at the surface. The geothermal system lies along the axis of Hrómundartindur and is directly adjacent to the eastern flank of the Hengill, with faults and fissures striking along the same NE-SW trend as in Nesjavellir. The area is considered seismically active, and seismic surveys indicate magma at a depth of ~6 km beneath the system (Gebrehiwot 2005). The hydrothermal surface activity at Ölkelduháls has been shown to fluctuate drastically with water table depth (seasonally). During

17

dry periods, hot springs and mud pots revert to fumaroles and steaming ground, returning to hot springs during wet periods. Previous studies of the Ölkelduháls system have focused primarily on production potential of wells in the area (e.g. Marty et al. 1991; Natukunda 2005; Nono et al. 2018). Few detailed geochemical studies have been conducted on the surface fluids and mineralogy present at Ölkelduháls, and this contribution presents the first investigation of surface trace element geochemical composition of the Ölkelduháls hydrothermal system. A map of the study area is provided in Figure 8, along with sample locations.
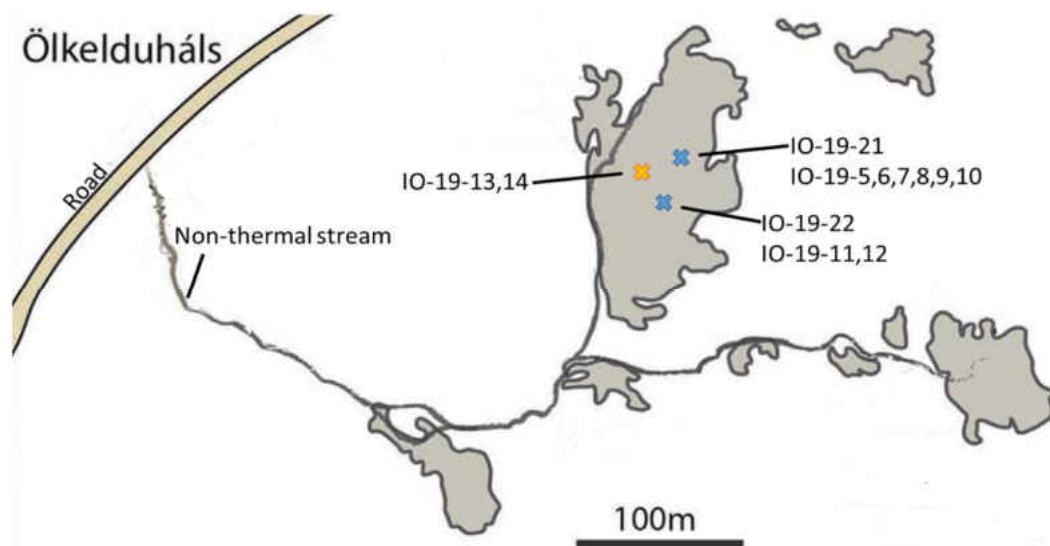
Figure 8: Ölkelduháls geothermal area. As with previous maps, yellow X's indicate location of solid samples not directly associated with a hot spring, blue X's indicate location of the two hot springs sampled; associated sample tags are also indicated. North is up. Figure adapted from Kaasalainen et al. (2017).

4. Methods

4.1 Sample collection

4.1.1 Fluids

Upon arrival at each field area, hot springs were surveyed with pH strips and a temperature probe to prioritize representative thermal features with different conditions. Once a hot spring was selected, a field-portable thermal fluid sampling apparatus was deployed along with a Hydrolab HL4 sonde, following

Figure 9: Fluid sampling set up; numbers in sequence of fluid flow. (1) silicone inlet tubing set under hot spring surface; (2) cooling coil, refilled with cold water as needed; (3) peristaltic pump; (4) in-line filter; (5) outlet tube fitted to luer-lock syringe and sealed sample bottle or flow-through chamber for in situ analysis with Hydrolab sonde, as needed.

modified methods of Arnórsson et al. (2006) (Figure 9). Using a battery-operated peristaltic pump, fluids were directed through a copper cooling coil submerged in cool water, causing the temperature to rapidly drop to $< \sim 50°C$. Fluids were subsequently filtered in-line through 0.2 μm cellulose-acetate filter papers and pumped through the entire system for at least 1 minute to sufficiently pre-contaminate the apparatus. Pre-cleaned, sealed serum bottles fitted with rubber stoppers and filled with N_2 gas were then attached to an outlet tube with a 10 ml luer-lock syringe and fluid samples were pumped directly into sample bottles to minimize atmospheric contact/degassing. Cation and trace metal sample bottles were pre-acidified with $\sim$ 1 ml of 2 N trace metal-grade HNO_3. Anion sample bottles were pre-cleaned and filled only with N_2 gas to

minimize oxidation/reaction following collection. Field blanks were taken with deionized 18.2 MΩ water prior to sampling each day, when analytical-grade water was available.

Fluid properties considered unstable for long-term storage, including total carbonate carbon (TCC), pH, temperature, Fe^{2+} concentration, and total sulfide sulfur (ΣS^{2-}) were either determined in-situ or preserved until laboratory analysis was possible. For TCC determination, field titrations were conducted on all fluid samples. For acidity titrations, 0.2 M NaOH was titrated into a water sample immediately following collection until the equivalence point was reached. Alkalinity titrations were conducted with the aid of a Hach digital titrator, with either 0.14 N or 0.0014 N H_2SO_4 used as the titrant, depending on fluid sample pH. ΣS^{2-} was preserved by precipitating aqueous sulfide as ZnS powder. Samples were then stored under refrigeration and darkness until dissolution of the solid and subsequent spectrophotometric laboratory analysis was possible (following methods of Cline [1969]). Fe^{2+} was determined on-site with Hach ferrous iron reagent ampules and a visual comparator. For in-situ determination of oxidation-reduction potential (ORP), specific conductivity (SpCon), pH, dissolved oxygen (DO), salinity (sal), and total dissolved solids (TDS), a sealed flow-through chamber fitted to the Hydrolab HL4 sonde was deployed.

4.1.2 Solids

Hard rock, altered sediment, and precipitate samples were collected from active surface geothermal areas, typically associated with the hot spring waters selected for analysis, except for alteration products associated with active fumaroles/steaming ground. Surface precipitates and sediments were differentiated based on physical appearance (e.g. color/texture) and were collected with increasing distance from the margin of a hot spring where there was visible interaction with water and/or steam. If a shallow redox gradient was visible (based on changing

color/texture with depth), samples were also collected from shallow depths (up to a few cm). Where steam was in direct contact with sediments and colorful surface encrustations were visible, representative precipitate samples were collected.

Both fluid and solid samples were assigned sample tags to reflect their origin. Samples labeled 'IO' were collected at Ölkelduháls, 'IN' from Nesjavellir, and 'IG' from Geysir. The middle digit refers to the year in which the samples were collected, and the final number refers to the order in which the sample was collected. For example, a sample labeled 'IG-19-5' would refer to the 5th sample collected from the Geysir area in 2019.

4.2 Site & sample selection

GPS coordinates for all samples are provided in Table S1 (Appendix A). Images depicting the layout of each field site and sample relationships/characteristics are provided below in Figures 10 – 13 (and are summarized in Table 1).

Images of most samples from Ölkelduháls, indicating their context in more detail, are

provided in Figure 10 (excluding precipitates collected on a nearby ridge not adjacent to the hot

springs). Two actively steaming hot springs were found on the flanks of a heavily altered hillside

(IO-19-21, pH = 2.15, T = 75.4°C; and IO-19-22, pH = 3.54, T = 54.8°C), and fluid samples

were collected from each, along with associated alteration products including subaqueous muds,

altered wall rocks, and precipitates lining the areas adjacent to the springs.
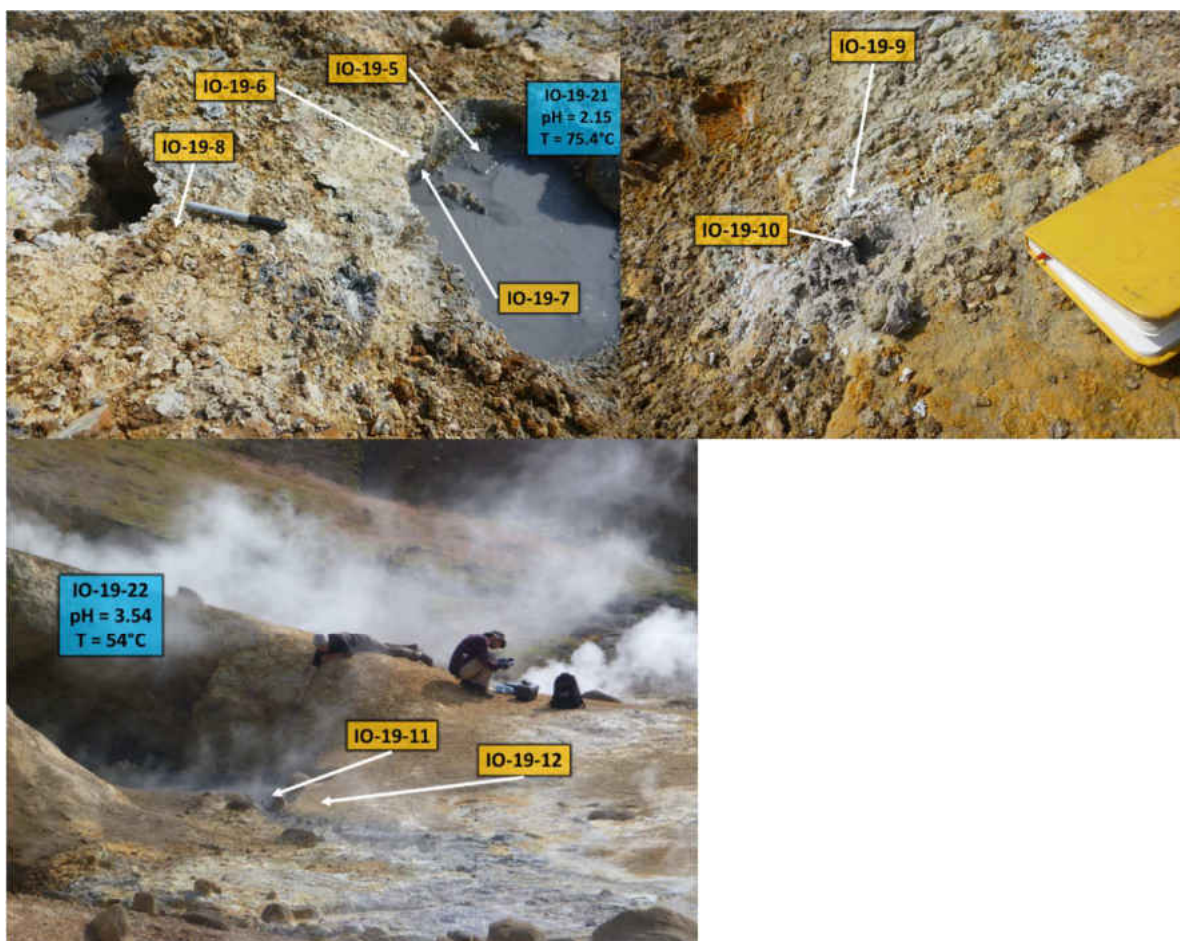
Figure 10: Samples collected at Ölkelduháls. Fluid samples are labeled in blue and include pH and
temperature upon sample collection. Solid samples are indicated in yellow. Marker, field notebook, and
geologists included for scale.

4.2.2 Nesjavellir

Two thermal areas were sampled at Nesjavellir. The first site, to the south, was investigated in detail in Glenister (2018) and Black (2018). Therefore, only a single fluid sample (IN-19-1, pH = 5.27, T = 81.5°C) and associated precipitate (IN-19-2) were collected for analysis (Figure 11).

The second thermal area studied at Nesjavellir (to the north) hosted three hot spring pools within ~ 1 m of each other (IN-19-6, IN-19-7, and IN-19-11) adjacent to a heavily altered cliff face. Each pool flowed into the next and had pH values ranging from acidic to near-neutral. To assess the geochemical differences between them and their associated alteration products, fluids and solids from each hot spring were collected (Figure 12).

Figure 11: Water sample and one associated sulfate-rich precipitate from Nesjavellir.
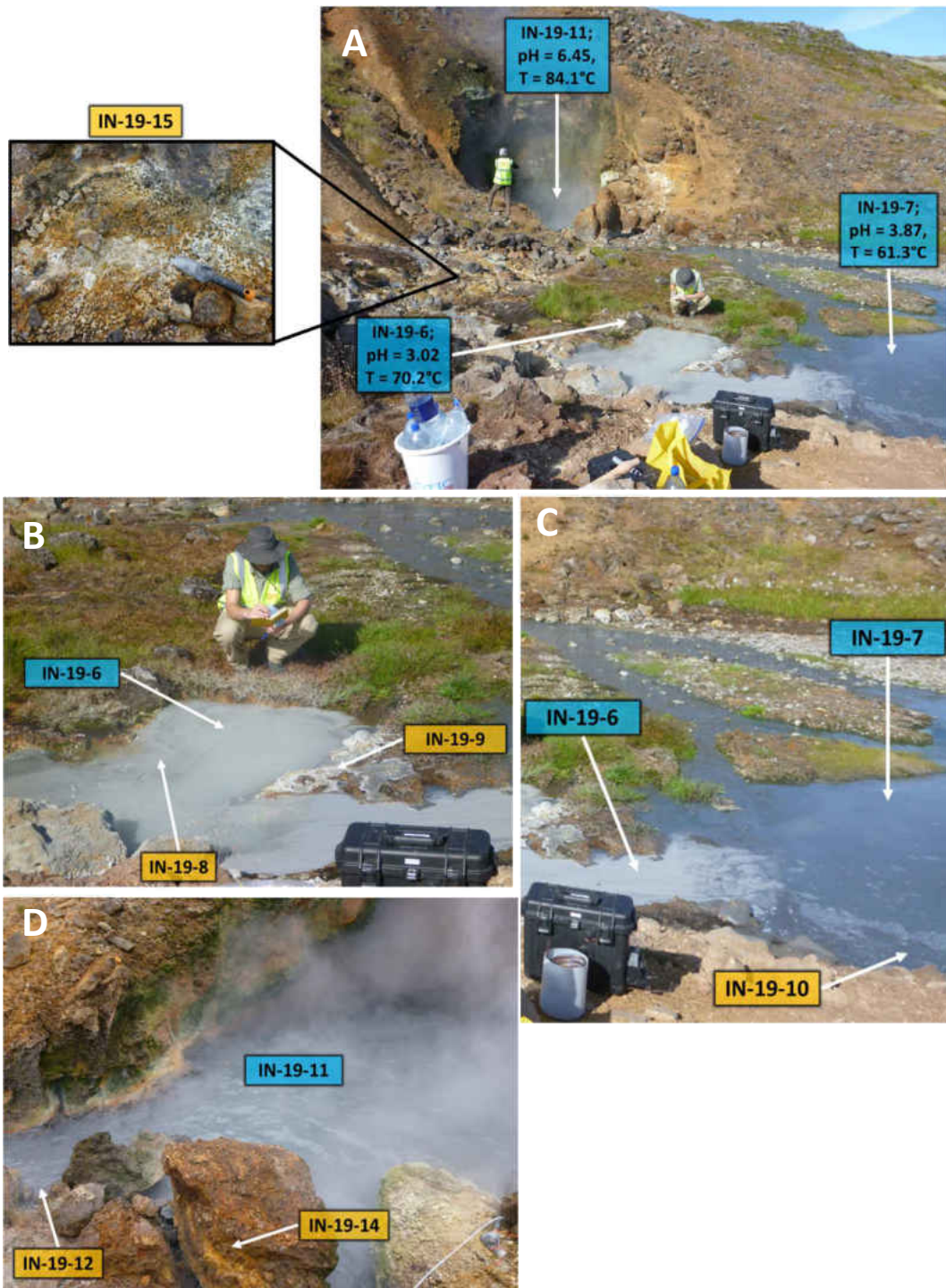
Figure 12: (A) Three hot springs and their associated alteration products at Nesjavellir. Inset shows surface precipitates. (B) IN-19-6 with altered muds and precipitates. (C) IN-19-7 and an altered mud. (D) IN-19-11, an altered mud, and a friable, altered boulder adjacent to the hot spring.

4.2.3 Geysir

Hot springs in the southwest field of Geysir were first surveyed for pH and temperature and two representative near-neutral to subalkaline sites were selected. For those sites, water was sampled and analyzed in situ in more detail (IG-19-01 (pH = 8.34, T = 84.1°C; Figure 10A), and IG-19-03 (pH = 6.01, T = 92.5°C; Figure 10B)). Both hosted extensive sinter aprons and representative sinter pieces were sampled. Water from Blessi hot spring in the main geyser field was also collected (IG-19-05; pH = 8.7, T = 95.6°C; Figure 10C), along with associated sinter. A piece of sinter from a no longer active hot spring to the northeast (IG-19-15) was also collected. A fumarole was identified to the northeast of the main geyser field and was sampled systematically over a transect of 120 cm from the steam vent (samples IG-19-7 through IG-19-12; Figure 13E). A nearby shallow fissure emitting fumarolic vapors and lined with precipitated minerals was also sampled (IG-19-13 and IG-19-14; Figure 13D).
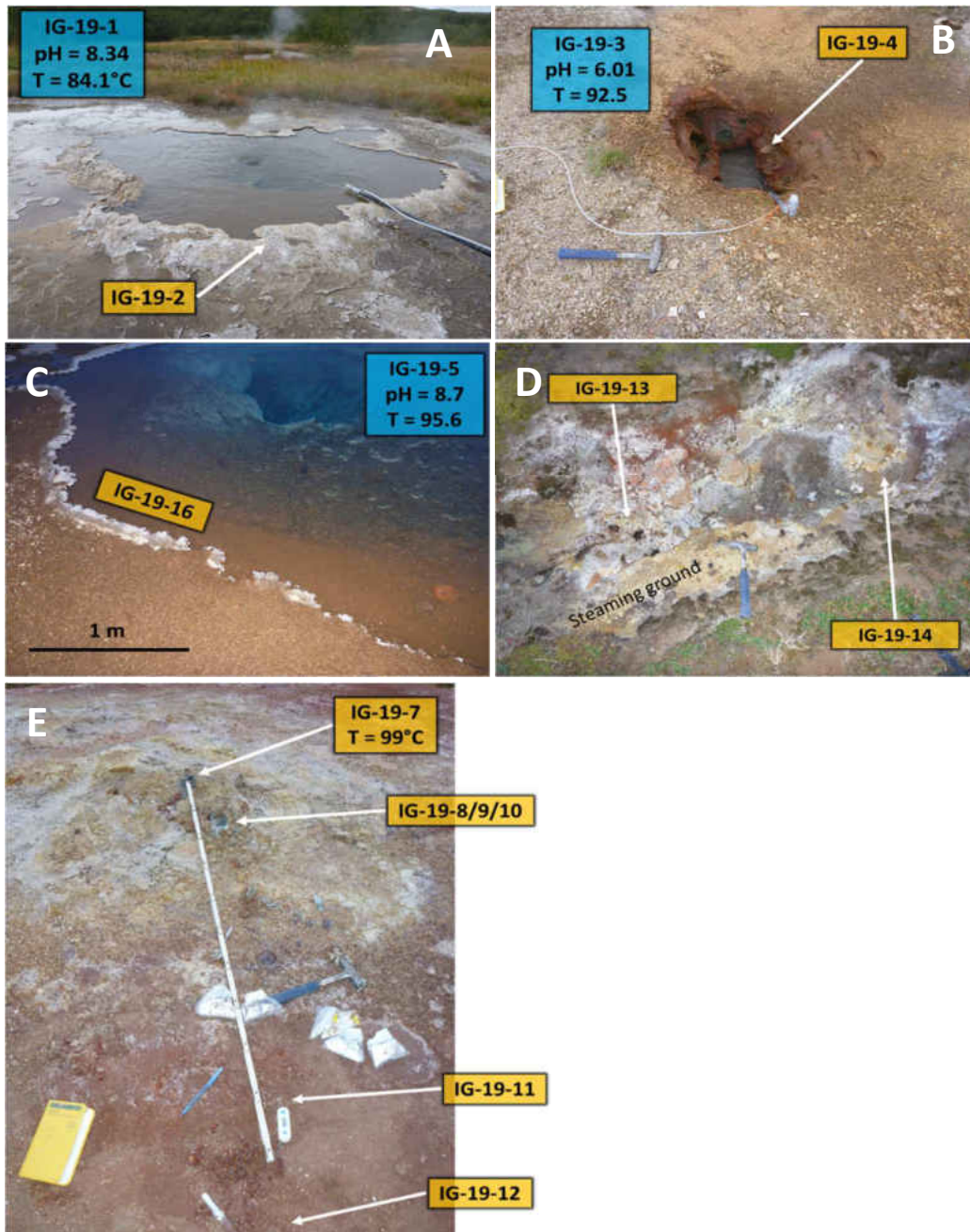
Figure 13: The thermal features sampled at Geysir. (A) IG-19-1, a subalkaline sinter-depositing hot spring in the main thermal field. (B) IG-19-13, near-neutral hot spring recessed in a ~ 1 m deep hole, depositing red-stained sinter. (C) Blessi hot spring (IG-19-5) and sinter. (D) A steaming gully producing colorful surface encrustations. (E) A fumarole mound and associated alteration samples. Ruler is 1.5 meters long.

4.3 Analytical methods

4.3.1 Fluids

Major cations (Ca^{2+}, Mg^{2+}, Na^+, K^+) were measured using a ThermoFisher i-CE 3000 series atomic absorption (AA) spectrometer and major anions (NO_3^-, SO_4^{2-}, Cl^-, PO_4^-) were determined with a ThermoFisher ICS-1000 ion chromatography (IC) system. Total sulfide sulfur (preserved as ZnS) was determined by re-dissolving preserved ZnS in cold v/v 50% HCl followed by immediate spectrophotometric analysis in O_2-free water following methods of Cline (1969). Values were determined by building a calibration curve using a NIST-certified Na_2S laboratory standard, and r^2 values of calibration curves were all > 0.99. All other elements were determined with a ThermoFisher Element 2 inductively coupled plasma mass spectrometer (ICP-MS). Elements analyzed include B, Rb, Sr, Ba, Al, Si, Ti, V, Cr, Mn, Fe, Co, Ni, Ga, Ge, and As. For all major and trace elements and analytical techniques, quantitative results were achieved by developing calibration curves with certified laboratory standards. Relative standard deviation in all duplicate analyses was < 1%, and is therefore excluded from our results. Analytical limits of detection for all instruments is reported in Table S2 (Appendix B).

4.3.2 Solids

Soft precipitate and sediment samples were air-dried (to preserve any potentially heat-sensitive mineral phases) and powdered by hand in an agate mortar and pestle to a suitable grit size for qualitative XRD analysis. Substrate/hard rock samples were powdered in a tungsten-carbide shatterbox and then further ground by hand. Powdered samples were then mounted as random powder mounts and analyzed using a Bruker D8 Focus XRD equipped with a Cu Kα radiation source and scintillation detector, 1s per 0.02° 2θ, 2°-60° range. Mineral phases were

identified using Bruker's EVA software. All XRD methods followed methods of McHenry et al. (2020).

For bulk geochemical analysis, loss on ignition (LOI) was determined by heating ~ 1 g of each sample to 1050°C in a muffle furnace for 15 minutes. Fused beads were then made by mixing 1.0000 g of each sample with ~1 g of NH_4NO_3 as an oxidizer and 10.0000 g of 50:50 lithium metaborate:lithium tetraborate flux with 1% LiBr as a non-wetting agent. Mixtures were fused in a Claisse M4 fluxer. Each bead was then analyzed for major, minor, and some trace elements on a Bruker S4 Pioneer wavelength dispersive x-ray fluorescence (WD-XRF) spectrometer. Calibration curves were constructed from eleven USGS igneous and sedimentary rock standards (analytical LODs reported in Tables S2). All XRF methods followed methods of Byers et al. (2016).

Additional trace element analyses were provided by University of Houston Department of Earth and Atmospheric Sciences. Samples were dual-acid (HF + HNO_3) digested using a Milestone Ultrawave Microwave Digestion System. Resulting solutions were diluted as needed and analyzed on a Varian 810 triple quadrupole ICP-MS for sulfur and titanium, and an Agilent 725 inductively coupled plasma optical emission spectrometer for trace elements V, Cr, Co, Ni, Cu, Zn, Ge, Zr, and Ba. Quantitative results were achieved by running a multi-element internal standard and correcting the results with USGS rock standards BHVO-2 and SCO-1.

4.4 Geochemical calculations

4.4.1 PHREEQC

Calculations of mineral saturation state and aqueous speciation was carried out with PHREEQC version 3 (Parkhurst and Appelo 1999). PHREEQC assumes equilibrium thermodynamics to assess saturation indices (SI; defined in Section 5.4) based on fluid properties measured both in situ and in the lab. For hydrothermal systems, this is a reasonable assumption as fluid chemistry is widely considered to be controlled by a close approach to equilibrium with hydrothermal minerals with the exception of highly mobile elements such as Cl and B, although this assumption is challenged at the surface where rapidly changing conditions may lead to kinetically controlled reactions and redox and thermodynamic disequilibrium. To address this, charge balance was forced with SO_4^{2-} in low pH solutions (< 3), and with CO_2 in all other fluids. The WATEQ4F.dat database was chosen for the calculations, as the minerals included in the database cover a range of hydrothermal minerals found in various environments, although it does not include all the sulfates observed.

5. Results

Brief sample descriptions are summarized in Table 1. Detailed analytical results are reported in Sections 5.1 – 5.4.

5.1 Mineral assemblages

XRD results of unaltered volcanic rocks collected from each field site are provided in Table 2. XRD results of altered materials from Ölkelduháls, Nesjavellir, and Geysir are reported in Table 3, and sulfate minerals identified throughout the study are reported in Table 4. Brief descriptions of sample mineral assemblages relevant to their discussion in subsequent sections are also provided in this section.

Table 1: Sample descriptions

Site	Sample	Description & associated water sample	Temp (°C)	pH
Ölkelduháls	IO-19-21*	small, murky hot spring	75.4	2.15
	IO-19-22*	large, murky hot spring carved into altered sediments	54.8	3.54
	IO-19-5	dark-colored, subaqueous mud; associated with IO-19-21	81.7	2.15
	IO-19-6	thick, hard surface crust; on margin of IO-19-21	81.4	--
	IO-19-7	altered soil; associated with IO-19-21	90.8	--
	IO-19-8	tan/orange precipitate; 70 cm from IO-19-21	50.6	--
	IO-19-9	soft, crenulated surface crust; ~5 m from IO-19-21	43.9	--
	IO-19-10	buff/tan clay directly underlying IO-19-9	58.6	--
	IO-19-11	grey subaqueous mud; on edge of IO-19-22 pool	28.0	3.54
	IO-19-12	colorful beige sediment/mud; adjacent to IO-19-22	27.5	--
	IO-19-13	yellow surface crystals atop altered soil; in occasional contact with steam	--	--
	IO-19-14	euhedral trigonal quartz crystals protruding from altered soil	--	--
Nesjavellir	IN-19-1*	water sample: dark grey heavily steaming hot spring	81.5	5.27
	IN-19-2	light yellow surface crust coating altered rocks adjacent to IN-19-1	43.3	--
	IN-19-6*	water sample: light grey small spring flowing into IN-19-7	70.2	2.73
	IN-19-7*	water sample: dark grey stream mixing with IN-19-6	61.3	3.35
	IN-19-8	light grey subaqueous mud; associated with IN-19-6	29.3	2.73
	IN-19-9	white surface crust on margins of IN-19-6	61.8	--
	IN-19-10	dark-colored subaqueous mud; associated with IN-19-7	47.6	3.35
	IN-19-11*	water sample: large bubbling spring carved into altered wall rock	86.0	6.05
	IN-19-12	dark-colored subaqueous mud; associated with IN-19-11	79.4	6.05
	IN-19-14	friable, altered boulder	--	--
	IN-19-15	crenulated surface crust; in drainage between IN-19-6, IN-19-7, and IN-19-11	68.1	--
Geysir	IG-19-1*	water sample: clear spring with well-developed sinter apron	84.1	8.34
	IG-19-2	sinter from margins of IG-19-1	84.1	8.34
	IG-19-3*	water sample: turbid spring in ~0.5 m hole with red-stained sinter/altered rock	92.5	6.01
	IG-19-4	red-stained sinter from margins of IG-19-3	92.5	6.01
	IG-19-5*	water sample: Blessi hot spring; clear, blue with well-developed sinters	95.6	8.70
	IG-19-15	sinter associated with extinct hot spring	--	--
	IG-19-16	sinter from margins of Blessi hot spring (IG-19-5)	95.6	8.70
	IG-19-7	fumarole - vent; brown dirt coated with thin yellow precipitate	99.8	--
	IG-19-8	fumarole - white/beige surface chips 20 cm from vent	97.3	--
	IG-19-9	fumarole - beige mud directly beneath IG-19-8	97.3	--
	IG-19-10	fumarole - dark grey mud 4 cm below IG-19-9	98.8	--
	IG-19-11	fumarole - dark red/maroon coating mixed with light grey mud; 90 cm from vent	75.6	--
	IG-19-12	fumarole - red soil with flecks of beige clay; 110 cm from vent	51.1	--
	IG-19-13	white dendritic precipitate in steaming gully	99.0	--
	IG-19-14	Soft, wet, white precipitate in steaming gully	98.9	--

*water sample

Table 2: Mineral phases identified in substrate samples from Ölkelduháls, Nesjavellir, and Geysir.

Location	Primary phases	Secondary phases	Classification/description
Ölkelduháls	anorthite, augite, olivine	smectite	basaltic hyaloclastite
Nesjavellir	anorthite, augite	n/a	basalt
Geysir	biotite, albite, sanidine	n/a	rhyolite

Table 3: Alteration products and precipitates detected in XRD scans, listed according to their relative

Site	Sample	Setting	Dominant	Major	Minor
Ölkelduháls	IO-19-5	Steam-heated hot springs; pH = 2.15 - 3.54	Qtz, Py	--	--
	IO-19-6		Qtz, npOx^	--	--
	IO-19-7		Qtz	AmSi, Py	Ana, Smec, Kaol
	IO-19-8		AmSi	Qtz	Ana, Py, Kaol
	IO-19-9		Sulf*	--	Qtz, Smec, Ana
	IO-19-10		Qtz, Kaol	Ana	--
	IO-19-11		Qtz, Smec	Py	--
	IO-19-12		Qtz, Py, Smec	--	Ana
	IO-19-13		Sulf*	S	--
	IO-19-14		Qtz	--	--
Nesjavellir	IN-19-2	Mixed steam-heated hot springs; pH = 2.73 - 6.05	Sulf*	--	--
	IN-19-8		Py	AmSi, Smec	Alb
	IN-19-9		Sulf*	AmSi	--
	IN-19-10		Py, Smec, Kaol	--	--
	IN-19-12		Smec	Py, Kaol	Sulf*
	IN-19-14		ChP	Smec	--
	IN-19-15		Sulf*	--	AmSi
Geysir	IG-19-2	Near-neutral/alkaline hot spring	AmSi	Qtz, Cal, Smec	San
	IG-19-4		AmSi	--	--
	IG-19-16		AmSi	--	--
	IG-19-15	Extinct hot spring	Opal, Qtz	Smec	Trid
	IG-19-7	Fumarole mound	Py, Smec, Kaol	S	--
	IG-19-8		AmSi, Smec	npOx^	Ana
	IG-19-9		npOx^, Ana, Kaol	Smec	AmSi
	IG-19-10		Py, Kaol	--	AmSi, Ana
	IG-19-11		npOx^	Kaol	Smec, AmSi
	IG-19-12		npOx^, Smec	--	AmSi
	IG-19-13	Steaming gully	Sulf*	--	Py
	IG-19-14		AmSi, Sulf*	--	--

Alb - albite; AmSi; amorphous silica; Ana - anatase; Cal - calcite; ChP - chalcopyrite; Kaol - kaolinite; npOx - nanophase iron oxyhydroxides; Opal - opal-A; Py - pyrite; Qtz - quartz; S - native sulfur; San - sanidine; Smec - smectite group minerals; Sulf - sulfate minerals; trid - tridymite

*sulfate minerals listed in Table 3

^Presence of npOx is inferred from high Fe-content determined in XRF and lack of crystalline Fe minerals in diffraction pattern.

Table 4: *Sulfate minerals identified using XRD*

Sample	Major	Minor
IO-19-9	halotrichite group	--
IO-19-13	copiapite, paracoquimbite	rhomboclase
IN-19-2	halotrichite group	--
IN-19-9	anhydrite	--
IN-19-12	--	gypsum
IN-19-15	halotrichite group	--
IN-19-13	hexahydrite	halotrichite group
IN-19-14	anhydrite, bassinite, hexahydrite	--

Chemical formulae of sulfate minerals observed throughout study

Mineral	Chemical formula
anhydrite	$CaSO_4$
bassinite	$CaSO_4 \cdot 0.5H_2O$
copiapite	$Fe^{2+}Fe^{3+}_4(SO_4)_6(OH)_2 \cdot 20H_2O$
gypsum	$CaSO_4 \cdot 2H_2O$
halotrichite group [a]	$(Fe^{2+},Fe^{3+},Mg)Al_2(SO_4)_4 \cdot 22H_2O$
hexahydrite	$MgSO_4 \cdot 6H_2O$
paracoquimbite	$(Fe,Mg)Al_2(SO_4)_4 \cdot 22H_2O$
rhomboclase	$H_5Fe^{3+}O_2(SO_4)_2 \cdot 2H_2O$

[a] halotrichite group minerals include pickeringite, halotrichite, and bilinite, all of which are indistinguishable from one another in XRD

5.1.1 Ölkelduháls

Mineral diversity at Ölkelduháls was somewhat limited. Samples collected within a few meters of both hot springs (water samples IO-19-21 and IO-19-22) commonly contained quartz with anatase, along with pyrite, smectite, and/or kaolinite. Two dark-colored, subaqueous mud samples scooped from just beneath the water surface (IO-19-11 and IO-19-5; Figure 10) contained quartz along with pyrite and smectite. 1-2 cm euhedral trigonal quartz crystals (IO-19-14) were found protruding from altered muds a few meters away from the hot springs sampled. One sample collected on a ridge between the two hot springs (IO-19-13) contained elemental sulfur and a combination of mixed-valence hydrated Fe-sulfates that included copiapite, paracoquimbite, and rhomboclase.

5.1.2 Nesjavellir

At Nesjavellir, the alteration products were more diverse, reflecting more variable environmental conditions. At the northernmost Nesjavellir site, three dark-colored subaqueous muds associated with variably acidic hot spring pools (IN-19-8, IN-19-10, IN-19-12; Figure 12) were found to contain pyrite along with either smectite or kaolinite; IN-19-8 also contained accessory amorphous silica, and IN-19-12 contained accessory gypsum. Precipitates collected in the areas surrounding these hot springs (IN-19-9 and IN-19-15) were occasionally in contact with volcanic vapors/fluids and included amorphous silica, anhydrite, and a halotrichite-group mineral, possibly pickeringite. Pickeringite and halotrichite form a solid solution between Fe-rich and Mg-rich end members, respectively, with further substitution of Fe^{2+} possible for Fe^{3+} in pickeringite (forming mixed-valence bilinite; Geptner et al., 2007; Carson, 2015). Distinguishing between these three minerals based on their XRD pattern alone is problematic given the extensive solid solution possible between end members and the similarity in their diffraction

33

patterns. Thus, minerals identified as halotrichite or pickeringite are subsequently labeled 'halotrichite group'.

5.1.3 Geysir

The three sinters sampled associated with active hot springs at Geysir (IG-19-2, IG-19-4, IG-19-16 Figure 13) were all predominantly composed of amorphous silica. IG-19-2 also contained quartz with accessory calcite, kaolinite, and presumably detrital albite. The sinter piece collected from an extinct hot spring (IG-19-15) contained opal-A, tridymite, and quartz (rather than amorphous silica), along with minor smectite.

The fumarole mound transect at Geysir (IG-19-7 through IG-19-12; Figure 13D) revealed largely consistent mineral patterns controlled by rock leaching/argillic alteration: amorphous silica ± an Fe-bearing phase (pyrite/npOx; depending on whether the sample was collected above or below a shallow redox front) ± anatase ± smectite/kaolinite. Elemental sulfur was detected in the vent sample (IG-19-7). The only other sulfur-bearing phase detected along the fumarole transect was pyrite.

Surface precipitates collected from a steaming gully a few meters from the fumarole mound (IG-19-13 and IG-19-14; Figure 13E) contained a mixture of Ca- and Mg-sulfates including anhydrite, bassinite, and hexahydrite (Table 3). IG-19-13 also contained accessory pyrite.

5.2 Elemental composition of solids

5.2.1 Protolith composition

Major and selected trace element compositions of sampled protoliths are reported in Table 5. Substrates recovered from Ölkelduháls and Nesjavellir were basaltic (SiO_2 43.35 and

47.45 wt. %, respectively). Although no basalt was sampled at Geysir, it has been observed

throughout the area, and chemical analyses from Jakobsson (1972) are reported for comparison

along with original data. A fresh surface lava sample from the Laugarfjall rhyolite dome adjacent

to the Geysir hydrothermal system was confirmed to be a rhyolite, consistent with the presence

of both basalt and rhyolite at Geysir.

Kaasalainen & Stefánsson (2012) compiled and reported median geochemical analyses

including major and trace elements of Icelandic basalts from > 50 previous studies, also reported

in Table 5. To make the comparison between protolith and altered samples consistent throughout

our analyses, their results are referenced in subsequent sections where appropriate.

Table 5: Major and trace element geochemical composition of substrates throughout Iceland

	Ölkelduháls	Nesjavellir	Geysir	Iceland olivine tholeiite[a]	Median Icelandic basalt[b]
SUM (wt. %)	94.35	98.99	99.84	99.92	--[d]
LOI (wt. %)	7.52	-0.49[c]	0.5	--[d]	--[d]
Major elements (wt. %)					
SiO$_2$	43.35	47.45	74.22	48.01	50.00
TiO$_2$	0.99	2.20	0.20	1.87	1.52
Al$_2$O$_3$	16.29	14.76	12.65	14.09	14.90
Fe$_2$O$_3$	10.36	13.15	2.83	12.48	10.80
MnO	0.22	0.20	0.05	0.21	0.19
MgO	5.26	6.48	0.18	8.29	7.86
CaO	9.49	12.20	0.76	11.77	12.30
Na$_2$O	0.65	1.97	4.96	2.17	2.14
K$_2$O	0.06	0.19	3.33	0.29	0.20
P$_2$O$_5$	0.08	0.25	0.02	0.19	0.02
S	0.22	0.13	0.01	--[d]	0.03
Trace elements (ppm)					
Ba	19	14	21	--[d]	55
Co	59	4	30	--[d]	54
Cr	149	54	25	--[d]	187
Cu	127	14	13	--[d]	140
Ge	2	1	6	--[d]	1[e]
Ni	78	6	12	--[d]	96
V	226	264	34	--[d]	198
Zn	67	18	21	--[d]	99
Zr	41	8	26	--[d]	80

[a]Average olivine tholeiite analysis for Icelandic central volcanic zone from Jakobsson (1972) taken to represent basaltic substrate at Geysir

[b]From Kaasalainen and Stefánsson (2012)

[c]Gain on ignition

[d]Not reported

[e]Ge results not reported in Kaasalainen & Stefánsson (2012); Nesjavellir basalt ICP-OES results reported instead

5.2.2 Altered sample major element composition

Major element geochemical compositions of altered samples as determined using XRF are reported in Table 6, and box and whisker plots indicating the general spread of major oxides are shown in Figure 14 (except Na_2O, MnO, and P_2O_5 due to low concentrations). Altered samples followed geochemical trends consistent with their association with either acid leaching-dominant or precipitation-dominant processes, with precipitates further grouped according to their association with acid-sulfate or neutral/alkaline thermal fluids/vapors. Since sulfur is partially (and inconsistently) lost during preparation by fusion for XRF and during LOI heating, samples with abundant sulfur-bearing minerals sometimes yield high (or low) analytical totals when LOI is included as part of the total. Sulfur-rich alteration samples (as determined using XRD) should therefore be considered semi-quantitatively with respect to the major element geochemistry reported. A brief summary of the geochemical compositions of altered samples from each field site follows in this section.

Table 6: Major element geochemical composition of altered samples. All values reported in wt. %. nd = not detected, na = not analyzed

Site	Sample	SUM	LOI	SiO_2	TiO_2	Al_2O_3	Fe_2O_3	MnO	MgO	CaO	Na_2O	K_2O	P_2O_5	S[a]
Ölkelduháls	IO-19-5	96.50	16.20	46.10	1.55	6.18	25.03	0.01	0.46	0.16	nd	0.12	0.56	na
	IO-19-6	94.59	9.52	49.00	1.82	5.52	27.55	0.01	0.38	0.09	0.01	0.13	0.48	na
	IO-19-7	94.09	14.60	48.42	3.59	19.31	6.78	0.01	0.79	0.09	nd	0.08	0.30	4.85
	IO-19-8	104.95	34.70	49.51	1.52	8.08	9.79	0.01	0.74	0.22	0.05	0.07	0.20	4.70
	IO-19-9	101.94	14.76	72.86	2.46	6.23	4.72	0.02	0.57	0.15	nd	0.02	0.06	12.89
	IO-19-10	90.45	12.50	50.11	4.88	20.32	1.35	0.02	0.89	0.07	nd	0.02	0.22	na
	IO-19-11	90.44	16.00	37.52	3.33	14.10	15.43	0.07	2.54	1.06	nd	0.03	0.27	na
	IO-19-12	93.48	5.59	55.31	3.91	15.00	10.49	0.03	2.20	0.42	nd	0.03	0.42	na
	IO-19-14	100.78	0.74	98.29	0.26	0.84	0.32	nd	0.28	0.04	nd	0.01	0.03	na
Nesjavellir	IN-19-9	93.01	12.00	56.03	2.21	8.16	10.18	0.04	1.25	2.32	0.27	0.25	0.20	na
	IN-19-8	96.29	23.30	38.78	3.32	15.22	13.40	0.04	1.29	0.52	0.03	0.05	0.23	na
	IN-19-10	88.04	17.20	33.45	2.77	15.52	16.82	0.06	1.56	0.33	nd	0.02	0.21	na
	IN-19-12	87.62	11.90	37.67	1.76	14.46	14.08	0.14	5.14	2.17	0.04	0.04	0.18	na
	IN-19-14	91.3	4.24	47.95	1.91	13.98	12.69	0.12	5.84	3.75	0.43	0.09	0.18	na
Geysir	IG-19-2	98.51	2.24	90.73	0.15	1.50	1.04	0.02	0.71	0.86	1.09	0.16	0.02	na
	IG-19-4	98.38	3.19	86.72	0.41	3.34	3.18	0.02	0.61	0.62	0.15	0.08	0.05	0.03
	IG-19-15	102.54	2.48	98.32	0.06	1.03	0.11	nd	0.31	0.21	nd	0.02	nd	0.03
	IG-19-16	98.47	3.06	87.38	0.30	2.72	1.87	0.03	0.85	1.17	0.73	0.32	0.03	0.04
	IG-19-7	99.21	22.30	33.64	1.95	24.50	14.47	0.05	2.11	0.03	nd	0.01	0.05	na
	IG-19-8	101.94	14.76	72.86	2.46	6.23	4.72	0.02	0.57	0.15	nd	0.02	0.06	0.62
	IG-19-9	100.53	15.93	42.26	6.70	20.94	13.39	0.06	0.70	0.04	nd	0.04	0.27	0.54
	IG-19-10	96.09	18.18	42.10	1.80	29.17	3.91	0.02	0.65	0.02	nd	0.02	0.06	2.07
	IG-19-11	97.87	16.29	34.41	1.92	20.98	23.25	0.02	0.74	0.03	nd	nd	0.10	na
	IG-19-12	103.30	23.59	43.11	1.41	17.14	15.61	0.03	2.10	0.03	nd	nd	0.19	na
	IG-19-14	87.53	14.85	56.46	0.11	3.19	1.69	0.21	2.88	8.02	nd	0.02	0.10	1.79

[a] Sulfur concentrations determined using ICP-OES on selected samples; all other results determined using XRF

38
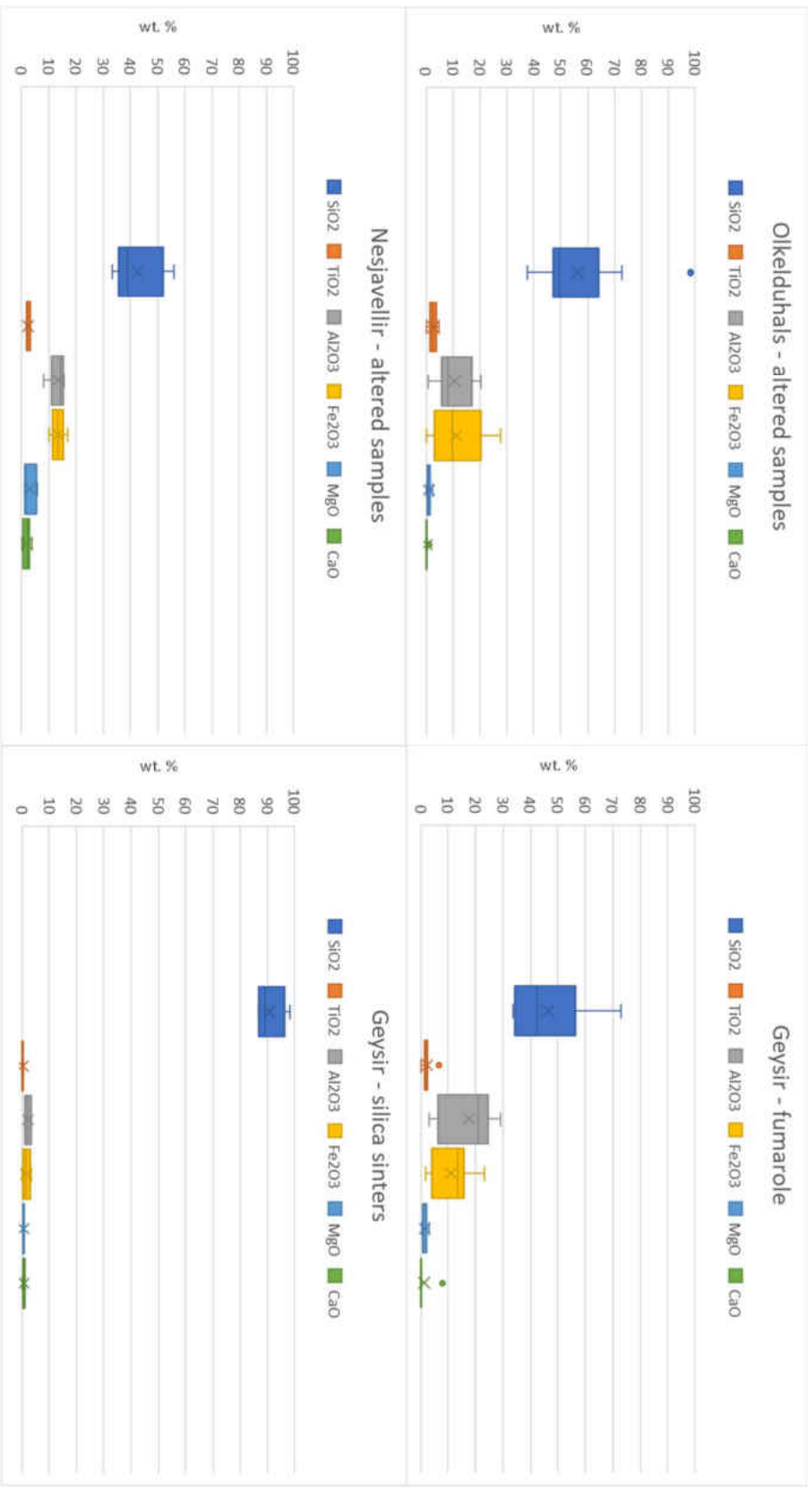
Figure 14: Box and whisker diagrams demonstrating spread of major oxide concentrations for Ölkelduháls and Nesjavellir altered samples, and Geysir fumarole and sinter samples. Na_2O, MnO, and P_2O_5 were omitted from the diagrams because their concentrations were consistently < 1 wt. %. Silica is consistently the oxide with the greatest overall abundance, and SiO_2, Al_2O_3, Fe_2O_3 all showed high variability. Other oxides had generally low concentrations and low variability.

39

5.2.2.1 Ölkelduháls

Alteration samples from Ölkelduháls followed trends of SiO_2 and TiO_2 accumulation consistent with rock leaching in an acidic environment. SiO_2 and TiO_2 concentrations ranged from 37.52 – 72.86 wt. % and 1.52 – 4.88 wt. %, respectively, in altered soils/muds and precipitates collected either adjacent to thermal pools (IO-19-6 through IO-19-10 + IO-19-12) or from beneath the water surface (IO-19-11, IO-19-5). Leached samples displayed consistently low abundances of MnO, MgO, CaO, Na_2O, and K_2O, while Al_2O_3 and Fe_2O_3 displayed more variable behavior. Higher iron contents coincided with samples containing npOx and pyrite, and clay-rich samples (e.g. IO-19-7 and IO-19-10) also contained elevated Al_2O_3 concentrations. Although slightly elevated relative to Ölkelduháls basalts/hyaloclastites, P_2O_5 concentrations were quite low.

5.2.2.2 Nesjavellir

Elemental compositions of altered samples from Nesjavellir followed similar patterns to those from Ölkelduháls, but residual enrichment of SiO_2 and TiO_2 was more subdued, indicating less extensive alteration on average. Fe_2O_3 and Al_2O_3 were highly variable at Nesjavellir, though higher Fe_2O_3 concentrations are observed in samples inferred to contain npOx. Higher Al_2O_3 concentrations again correlated with clay-rich samples. MnO, MgO, CaO, and Na_2O were all present in low concentrations or undetectable in most samples, except for IN-19-12 and IN-19-14 (5.14 and 5.84 wt. % MgO, respectively).

5.2.2.3 Geysir

Concordant with XRD results, SiO_2 concentrations were high in sinter precipitates (87.38 – 98.32 wt. %. Other oxide concentrations were all low in the sinters, with low concentrations of Al_2O_3 (1.03 – 3.34 wt. %) and Fe_2O_3 (0.11 – 3.18 wt. %), presumably related to the presence of minor phyllosilicates.

SiO_2 and TiO_2 concentrations in fumarole samples were variable, as were Al_2O_3 and Fe_2O_3. Other oxide abundances were quite low (generally << 1 wt. %), although the fumarole vent sample (IG-19-7) contained 2.11 wt. % MgO, possibly housed in Mg-smectites.

5.2.3 Trace elements

In total, thirteen solid samples including substrates were digested and analyzed for select trace elements using ICP-OES, including V, Cr, Co, Ni, Cu, Zn, Ge, Zr, and Ba, plus sulfur. The samples included silica sinters (IG-19-4, IG-19-15, IG-19-16), SiO_2-rich leached rocks with or without pyrite, sulfates, and clays (IG-19-8, IG-19-9, IG-19-10, IO-19-7, IO-19-8, IO-19-9, IO-19-10, and IN-19-15), and sulfate-rich precipitates (IG-19-13, IG-19-14, IO-19-13, and IN-19-2). Results are reported in Table 7, along with XRF results for selected trace metals.

Table 7: Trace element results for selected samples throughout the study. All results reported in ppm. nd = not detected, na = not analyzed.

	Sample	Ba	Co	Cr	Cu	Ge	Ni	V	Zn	Zr
Ölkelduháls	IO-19-7	154	82	109	106	0.9	80	386	19	244
	IO-19-8	10	6.6	280	25	1.9	20	309	12	108
	IO-19-9	153	15	51	38	1.5	20	218	13	112
	IO-19-13	30	8.6	12	39	1.0	9.5	39	7.6	80
	IO-19-10	73	1.8	82	15	0.7	2.7	477	19	334
Nesjavellir	IN-19-2	2.0	29	61	14	0.8	61	215	111	7.6
	IN-19-15	51	10	125	27	1.1	22	122	47	55
	IN-19-9[a]	nd	43	171	nd	na	nd	524	na	108
	IN-19-8[a]	nd	76	323	nd	na	150	334	na	155
	IN-19-10[a]	nd	97	282	90	na	245	379	na	128
	IN-19-12[a]	nd	74	267	83	na	157	350	na	89
	IN-19-14[a]	nd	62	279	90	na	85	283	na	91
Geysir	IG-19-4	738	48	1.5	11	4.2	3	5.4	219	574
	IG-19-15	4.3	24	8.1	2.6	0.3	1.4	9.3	2.7	3.9
	IG-19-16	21	30	25	13	6.0	12	34	21	26
	IG-19-8	10	6.6	280	25	1.9	20	309	12	108
	IG-19-9	9.1	54	873	179	3.0	110	1433	22	310
	IG-19-10	2.6	130	566	305	1.4	305	577	14	94
	IG-19-13	1.2	139	52	389	0.8	469	7.5	197	3.2
	IG-19-14	91	51	277	158	2.0	134	284	103	85

[a]XRF results reported for these samples (not analyzed using ICP-OES)

5.2.3.1 Ölkelduháls

Five samples were selected from Ölkelduháls for trace metal analysis. The results for altered soils/leached materials were variable overall, but V, Cr, Zr, and Ba were generally somewhat elevated in leached rocks/altered soils compared to Ölkelduháls hyaloclastite. Co, Ni, Cu, Zn, and Ge all generally had quite low concentrations, with the exception of IO-19-7 (Figure 10; an altered soil associated with IO-19-21, a hot spring with pH 2.15), which had slightly elevated Co (82 ppm), Ni (80 ppm), and Cu (106 ppm) values relative to other Ölkelduháls alteration samples. IO-19-13, a native sulfur and Fe-sulfate-bearing precipitate, had quite low concentrations of all trace elements analyzed (all < 100 ppm).

5.2.3.2 Nesjavellir

Only two samples from Nesjavellir were selected for trace metal analysis with ICP-OES, and XRF results for selected samples are reported instead, although in some cases the trace elements analyzed with XRF were below LOD or not analyzed (e.g. Ba, often bdl for XRF, and Ge, not measured using XRF). Nearly all altered soils and precipitates showed elevated levels of V and Cr, and somewhat elevated levels of Zr relative to Nesjavellir basalt, consistent with trends at Ölkelduháls. Zr was highest in altered soils/muds.

5.2.3.3 Geysir

Geysir sinters had low concentrations of the trace elements analyzed, with the exception of IG-19-4, a red-stained sinter collected from the margins of hot spring IG-19-3 (pH = 6.01, T = 92.5°C), which had elevated Zn (219 ppm), Zr (574 ppm), and Ba (738 ppm) relative to other sinters (IG-19-15, IG-19-16). Other elements had negligible concentrations.

43

Consistent with results from Nesjavellir and Ölkelduháls, acid-leached samples from the fumarole transect (IG-19-8, IG-19-9, and IG-19-10) had elevated V, Cr, and Zr relative to presumed substrate, but also had higher concentrations of Ni and Cu than seen in other leached samples.

5.3 Aqueous geochemistry

Major ion compositions for water samples are reported in Table 8, nine of which (collected in the 2019 field season) include total carbonate carbon and total sulfide (not measured in the 2016 and 2017 field seasons), along with trace elements. Most of the waters were found to be relatively dilute. The waters sampled across all field sites include acid-sulfate waters, steam-heated mixed waters, and NaCl waters with pH ranging from 2.15 – 8.7, and temperatures from 61.3 – 95.6°C. In situ measurements made with the Hydrolab sonde are reported in Table 9.

Table 8: *Major element composition of thermal fluids; na = not analyzed, nd = not detected*

Sample	T°C	pH	Major elements (ppm)												
			SiO_2	Na	K	Ca	Mg	Fe	Al	Cl	ΣCO_2	SO_4^{2-}	H_2S	NO_3^-	PO_4^{3-}
IO-19-21	75.4	2.15	186.8	8.4	2.4	39.5	103.7	485.6	160.8	1.2	2209	236.1	1.5	2.2	nd
IO-19-22	54.8	3.54	101.2	4.6	2.0	41.6	102.5	2.1	12.4	2.1	20	405.9	0.7	4.1	4.3
IN-19-1	81.5	5.27	32.7	12.3	0.6	15.8	3.1	3.3	13.8	2.4	14	50.1	1.7	0.7	2.6
IN-19-6	70.2	2.73	96.8	14.5	1.3	32.0	22.3	42.7	40.8	2.9	377	379.0	2.4	1.6	2.5
IN-19-7	61.3	3.35	79.8	22.6	3.5	43.8	19.5	7.1	17.3	2.8	70	203.9	2.2	2.7	2.2
IN-19-11	86.0	6.05	62.5	35.0	5.1	50.4	5.4	0.8	21.0	2.6	38	136.6	3.7	2.7	nd
IG-19-1	84.1	8.34	118.1	158.0	10.9	1.6	0.7	1.6	15.5	104.9	na	100.0	0.7	0.1	nd
IG-19-3	92.5	6.01	155.6	117.0	8.9	3.4	2.4	1.3	17.8	75.5	15	127.4	nd	1.3	2.2
IG-19-5	95.6	8.70	164.4	159.0	20.2	1.5	0.9	1.3	25.2	105.2	274	98.2	2.6	nd	nd

Trace element composition of thermal fluids

Sample	T°C	pH	Trace elements (ppb)												
			As	B	Ba	Cr	Ga	Ge	Mn	Ni	Rb	Sr	Ti	V	Zr
IO-19-21	75.4	2.15	0.1	2.1	102.8	66.6	6.3	1.3	8225.5	79.1	67.6	99.1	534.3	884.3	10.7
IO-19-22	54.8	3.54	nd	7.4	118.7	0.6	nd	2.2	3605.0	0.6	56.0	222.4	0.6	62.7	0.3
IN-19-1	81.5	5.27	nd	2.5	73.2	3.1	nd	nd	24.9	1.8	54.4	71.6	32.2	56.0	0.6
IN-19-6	70.2	2.73	0.2	5.6	89.5	28.2	0.7	0.2	1308.3	12.7	56.5	109.8	125.6	162.9	2.2
IN-19-7	61.3	3.35	nd	7.0	95.7	0.7	nd	0.8	568.4	0.5	62.0	203.5	0.3	61.6	0.2
IN-19-11	86.0	6.05	nd	7.3	84.4	nd	nd	1.0	0.9	0.1	61.4	212.9	nd	37.8	0.2
IG-19-1	84.1	8.34	48.9	642.2	74.5	nd	14.1	23.7	nd	nd	136.8	43.1	0.8	44.9	0.5
IG-19-3	92.5	6.01	61.4	414.6	104.2	nd	nd	9.9	97.0	nd	108.8	55.0	0.3	37.5	0.3
IG-19-5	95.6	8.70	51.0	683.9	70.9	nd	6.2	22.6	nd	0.2	212.5	42.1	0.1	46.1	2.5

Table 9: Selected Hydrolab results. DO = dissolved oxygen, Sp. Con = specific conductivity.

Sample	pH	DO (mg/L)	Salinity (g/L)	pe[a]	Sp. Con (mS/cm)
IO-19-21	2.15	0.96	2.73	8.88	5.065
IO-19-22	3.54	2.33	0.57	10.14	1.132
IN-19-1	5.27	0.39	0.09	2.93	0.181
IN-19-6	2.73	0.79	0.75	9.98	1.483
IN-19-7	3.35	0.07	0.32	4.84	0.645
IN-19-11	6.05	0.74	0.22	3.14	0.439
IG-19-1	8.34	2.23	0.55	4.53	1.117
IG-19-3	6.01	0.16	0.37	7.44	0.738
IG-19-5	8.70	1.11	0.54	3.06	1.074

[a]electron activity determined from in situ measurement of oxidation-reduction potential (ORP) in mV

5.3.1 Ölkelduháls

The two hot springs sampled at Ölkelduháls (IO-19-21 and IO-19-22; Figure 10) were acidic (pH 2.5 and 3.54) and had similar elemental compositions. SO_4^{2-} was the predominant anion, and SiO_2 and Mg^{2+} were the predominant species present in both springs. IO-19-21 (the more acidic of the two) also contained elevated Fe, Al, and elevated trace element concentrations relative to IO-19-22, including Mn, Ti, and V, and was also CO_2-rich (2209 ppm, determined via acidity titration). Other elements/ion complexes had negligible concentrations.

5.3.2 Nesjavellir

The three hot springs at Nesjavellir directly adjacent to one another (IN-19-6, IN-19-7, and IN-19-11) showed a trend of increasing pH with increasing apparent water volume (i.e. hot spring size; Figure 12). Dissolved species including SiO_2, CO_2, Fe, Mg, Mn, Ti, V, were all slightly elevated in the most acidic of the three springs (IN-19-6; relative to other samples), while Na, K, Ca, and Sr followed the opposite trend. IN-19-1 (pH 5.27; Figure 12), a sub-boiling steam-heated spring, had dilute concentrations of all major ions, metals, and trace elements.

45

5.3.3 Geysir

The three sinter-depositing hot springs sampled at Geysir (IG-19-3, IG-19-01, and IG-19-05) had similar compositions and were characterized by ~ 100 ppm SiO_2, Na^+, SO_4^{2-}, and Cl^-, and had elevated B (415 – 684 ppb) and Rb (109 – 213 ppb) concentrations relative to other hot springs sampled throughout the study.

5.4 Saturation Index (SI)

Saturation indices (SI) calculated with PHREEQC are shown in Table 10. SI is described as $SI = Q/K_i$ where Q is the reaction quotient and K_i is the equilibrium constant for element *i* at a specified temperature. SI values of 0 indicate that a fluid has reached saturation with respect to a given species. If $SI > 0$, the fluid is supersaturated, and the dissolved component will tend to precipitate. If $SI < 0$, then the fluid is undersaturated and the compound will tend to dissolve. To account for errors in our analyses and the thermodynamic database, SI values of $-0.4 < SI < 0.4$ for a given mineral/species are considered to represent saturation.

Table 10: Minerals with SI[a] > -0.4 calculated using PHREEQC. Minerals with -0.4 < SI < 0.4 are considered to be at or near equilibrium. Minerals with SI > 0.4 are considered supersaturated

		IO-19-21	IO-19-22	IN-19-1	IN-19-6	IN-19-7	IN-19-11	IG-19-1	IG-19-3	IG-19-5
					SiO_2[b]					
Amorphous silica	SiO_2	-0.14	-0.25	-0.40	-0.43	-0.43	-0.33	-0.69	-0.01	-0.47
Silica gel	SiO_2	0.05	-0.02	-0.20	-0.21	3.00	-0.17	-0.52	0.30	-0.32
Quartz	SiO_2	0.84	0.84	0.61	0.63	0	0.58	0.25	1.26	0.43
Chalcedony	SiO_2	0.55	0.49	0.30	0.30	0.30	0.33	-0.02	0.83	0.18
Cristobalite	SiO_2	0.50	0.48	0.27	0.27	0.27	0.26	0.87	0.87	0.10
				Oxides and hydroxides						
Hematite	Fe_2O_3	11.45	12.30	12.71	12.14	16.83	16.83	16.55	19.85	15.67
Magnetite	Fe_3O_4	6.11	7.80	7.56	8.42	13.93	--	15.19	20.68	18.99
Goethite	α-FeOOH	4.62	5.08	5.26	499.00	7.30	7.28	7.15	8.92	6.70
Diaspore	AlO(OH)	--	0.98	--	1.09	4.74	4.26	4.45	4.16	1.67
Gibbsite	$Al(OH)_3$	--	--	--	--	--	2.77	3.18	2.93	0.18
Boehmite	γ-AlO(OH)	--	--	--	--	3.50	--	--	2.46	0.46
$CO_{2(g)}$		--	2.03	--	--	--	--	--	--	--
				Sulfates						
Barite	$BaSO_4$	0.38	0.34	--	0.24	0.09	-0.07	0.29	0.04	--
Jarosite	$KFe^{3+}_3(OH)_6(SO_4)_2$	4.07	--	2.97	--	--	--	--	--	--
Alunite	$KAl_3(SO_4)_2(OH)_6$	--	--	0.64	3.11	--	3.71	4.15	--	--
Celestine	$SrSO_4$	--	--	--	--	0.12	--	--	--	--
Basaluminite	$Al_4(SO_4)(OH)_{10} \cdot 5(H_2O$	--	--	--	--	--	--	--	1.64	--
				Sulfides						
Greigite	$Fe^{2+}Fe^{3+}_2S_4$	--	8.02	8.68	10.06	13.46	1.03	15.25	16.31	3.60
Pyrite	FeS	3.68	4.82	4.27	5.94	3.85	--	5.14	7.27	1.32
				Phyllosilicates						
Pyrophyllite	$Al_2Si_4O_{10}(OH)_2$	7.16	10.03	8.22	10.13	17.14	19.43	17.89	14.19	13.91
Kaolinite	$Al_2Si_2O_5(OH)_4$	--	1.85	--	1.63	7.64	7.76	7.50	9.21	2.27
Halloysite	$Al_2Si_2O_5(OH)_4$	--	--	--	--	3.12	3.32	3.02	4.15	--
Illite	Variable	--	--	--	--	--	5.79	5.05	9.84	2.21
Smectite Group	Variable	--	--	2.28	4.27	6.23	13.99	12.55	12.32	11.33

[a]$SI = \log(Q/K_{eq})$

[b]Silica SI reported for all SI values

47

6. Discussion

6.1 Secondary mineralogy

Alteration products in subaerial hydrothermal environments are produced through three pathways: (1) in situ precipitation of minerals from hydrothermal fluids (e.g. as sublimates from fumarolic gases, from soil condensates, or from hot spring fluids directly), (2) the removal of mobile elements (e.g. Ca, Mg, K, Na) and residual enrichment of immobile elements (e.g. Si, Ti, Zr) in host rocks subject to acid attack from volcanically-derived volatiles, and (3) in-situ alteration of primary igneous minerals into secondary minerals (e.g. clays) (Stoiber and Rose 1974; Arnórsson et al. 1987; Jercinovic et al. 1990; Papike et al. 1991; Markússon and Stefánsson 2011; Hynek et al. 2013; McCollom et al. 2013a; Carson 2015; McHenry et al. 2017). In each case, the alteration mineral assemblage can be controlled through secondary mineral equilibria with the solid or vapor phase, through biogeochemical cycling of redox-sensitive elements (e.g. sulfur and iron; DesMarais 1996; Jorgensen 1999; Marteinsson et al. 2001; Tobler and Benning 2011; Cockell et al. 2019), or through kinetic barriers to mineral precipitation when hydrothermal fluids are in disequilibrium (Stefánsson et al. 2005; Kaasalainen and Stefánsson 2011; Kaasalainen et al. 2017).

This section provides an overview of the secondary minerals forming in each field site and attempts to explain the assemblage through synthesis of mineral chemistry and field observations. Overall conceptual models for surface hydrothermal alteration at each field site are discussed in Section 6.5.

6.1.1 Ölkelduháls

The mineral assemblages present at Ölkelduháls suggest acid leaching and pyrite/Al-phyllosilicate authigenesis were the two leading processes controlling alteration in a relatively mature hydrothermal system. This was evident in samples collected within a few meters of both hot springs (water samples IO-19-21 and IO-19-22) based on the high concentrations of SiO_2 and TiO_2 and the common occurrence of quartz with anatase (suggesting residual accumulation of silica + TiO_2 e.g., Stoiber and Rose 1974; Papike et al. 1991; Ruff et al. 2011). The co-occurrence of authigenic minerals (e.g. pyrite) with quartz in subaqueous muds scooped from just beneath the water surface (e.g. IO-19-11 and IO-19-5; Table 2) was observed for both hot springs. Quartz and pyrite were oversaturated in our PHREEQC results (Table 10), suggesting that both species could be actively forming in the modern system. However, the possibility that the quartz is detrital sediment entrained in the hot spring fluids and is related to an older (hotter) iteration of the Ölkelduháls hydrothermal system cannot be ruled out. In either case, the observation of 1-2 cm euhedral trigonal quartz crystals (IO-19-14) protruding from altered muds a few meters away from the hot springs suggests long-term alteration and diagenetic maturation at Ölkelduháls.

Al-phyllosilicates (smectite/kaolinite) are prevalent throughout Ölkelduháls and imply advanced argillic alteration. Recent studies indicate that smectite can form from a basaltic precursor under moderately acidic hydrothermal conditions (pH ~ 4), while kaolinite forms under lower pH conditions (as low as 2; Berger and Velde 1992; Ryu et al. 2010; Peretyazhko et al. 2018, 2020). Our observations are mostly consistent with such findings, as kaolinite was associated with IO-19-21, which had the lowest pH of all fluids studied (2.15), and smectite was associated with IO-19-22 (pH 3.54). However, smectite was observed in two samples < 1 m

49

away from IO-19-21, implying that there may have been ephemeral periods of elevated pH or channelized flow of higher pH fluids, or that smectite is forming under lower pH conditions than presently accepted. Peretyazhko et al. (2018, 2020) demonstrated through experimental reaction of simulated Mars basalt with H_2SO_4 that aluminous dioctahedral smectite (montmorillonite) can be produced in fluids with pH as low as ~ 3, though under higher pH regimes Fe- and Mg-rich trioctahedral smectite (saponite) forms instead. Although the XRD techniques used in the present study are not suited to distinguishing phyllosilicates beyond identification of kaolinite and smectite group minerals, elemental abundances of Al, Fe, and Mg in smectite-rich samples could be used as a reasonable proxy to infer clay composition. All of the smectite-rich samples from Ölkelduháls are Al-rich (14.10 – 19.31 wt. %), with MgO concentrations in the ~ 1 – 2.5 wt. % range. This suggests that while Al-smectite is likely the predominant phyllosilicate phase in these samples, minor Mg-smectites may also be forming. Alternatively, some of the Al in these samples may be housed in amorphous or semi-crystalline materials undetectable by XRD. However, it cannot be ruled out that the smectite in our samples may be associated with long-term alteration in the Hengill area and may reflect variability in fluid pH through time.

Pyrite was the predominant sulfur-bearing mineral present at Ölkelduháls and was found floating on the surface of both hot springs as a dark grey foam and in near-surface sediments, reflecting mobilization of Fe from host rocks and locally reducing conditions (from high H_2S supply). The prevalence of pyrite conflicts with the highly oxidizing aqueous conditions noted in the Hydrolab analyses for either spring (Table 9). This inconsistency may be related to the sluggish oxidation of S^{2-} under acidic conditions. Rather than proceeding along the pathway towards sulfate production through intermediate sulfur species (e.g., SO_3^{2-}, $S_2O_3^{2-}$), S^{2-} tends to precipitate metal sulfides at high concentrations (Kaasalainen and Stefánsson 2011; Stefánsson et

al. 2011). This provides an explanation for the high concentration of aqueous SO_4^{2-} in the fluids despite extensive pyrite formation.

Sulfate minerals were observed in two samples from Ölkelduháls. IO-19-13, a surface precipitate in occasional contact with steam emanating from hot springs was collected from a ridge ~ 10 m away from either hot spring and contained three soluble Fe-sulfate salts (copiapite, paracoquimbite, and rhomboclase). These minerals all imply extremely low water/rock ratios and locally acidic conditions in the soil (Robinson 2000; Hurowitz et al. 2005; Farrand et al. 2014; Rodríguez and van Bergen 2015). As Fe-sulfates are all absent in the PHREEQC results, these minerals likely formed through evaporation of highly acidic soil solutions, through the oxidation of pyrite, or through some combination of both processes. The presence of native sulfur in this sample also suggests partial oxidation of H_2S, which is likely present in soil condensates (Kaasalainen and Stefánsson 2011; Hynek et al. 2013; McCollom et al. 2013a; Black 2018). Products and pathways of pyrite oxidation are discussed in section 6.1.4.

6.1.2 Nesjavellir

Samples collected in the vicinity of the three hot springs at Nesjavellir (IN-19-6, IN-19-7, IN-19-11; Figure 12) contained amorphous silica, pyrite, smectites, kaolinite, halotrichite group minerals, and Ca-sulfates (gypsum/anhydrite) (Tables 3 and 4). One sample also contained accessory anatase. Kaolinite and smectite occurred together in two dark-colored subaqueous muds associated with hot springs of different pH (IN-19-10, IN-19-12) along with pyrite, again reflecting alteration and mobilization of Fe from host basalt and input of magmatic sulfur.

The presence of gypsum in sediment floating on the surface of a hot spring (IN-19-11) and anhydrite as a surface crust adjacent to another hot spring (IN-19-6; Table 3) can be attributed to mobilization and precipitation of Ca^{2+}. That gypsum is forming directly as a hot

spring precipitate with subaerial anhydrite a few meters away implies that anhydrite formed through dehydration of authigenic gypsum (Klimchouk 1996). Interestingly, this contrasts with the PHREEQC results (Table 10), which reflect undersaturation with respect to gypsum. Thus, the precipitation of gypsum may be kinetically controlled.

The prevalence of pyrite as opposed to npOx in this area implies high H_2S supply and reducing conditions, yet Hydrolab results again suggest moderately to highly oxidizing conditions (pe = 3.14 – 9.88; Table 9). Such inconsistencies reflect mixed potentials arising from disequilibrium between redox couples (e.g. Fe^{3+}/Fe^{2+}, H_2S/SO^4, O_2/H_2O; Stefánsson et al. 2005; Kaasalainen et al. 2017). Redox measurements made with a standard Pt-electrode thus have limited meaning, making it challenging to assess overall fluid redox states without measuring individual redox couples.

6.1.3 Geysir: sinter-depositing hot springs

Silica sinters associated with active hot springs were predominantly composed of amorphous silica and quartz (Table 3).

The composition of the sinters and active silica precipitation reflect oversaturation of silica in the near-neutral to alkaline boiled aquifer fluids throughout the geothermal field, although PHREEQC results imply that the hot springs there are either at saturation or slightly undersaturated with respect to amorphous silica (Table 10; IG-19-3). This can be explained in two ways.

Firstly, it is worth noting that amorphous silica dissolution is governed by the following reaction (Mountain et al. 2003):

(1) $$SiO_{2(am)} + 2H_2O \leftrightarrow H_4SiO_4^o$$

Thus, if dilute water is in equilibrium with amorphous silica, then its aqueous concentration

should be equivalent to its equilibrium constant (K_{eq}), and can be determined by

(2) $$K_{eq} = a_{H_4SiO_4}$$

However, silicic acid may not be the only species present in solution, as silicic acid will also tend

to deprotonate at higher pH, forming $H_3SiO_4^-$ (Arnórsson 1975; Arnórsson et al. 1985;

Gunnarsson 2000). Additionally, silica tends to form colloidal particles and polymers that are not

measured using standard methods. At slightly acid pH monomeric silica is the predominant form

of silica because polymerization is inhibited (Mountain et al. 2003). At alkaline pH, however,

this is not the case, and the silica concentrations reported for the alkaline fluids sampled at

Geysir (IG-19-01 and IG-19-05; Table 8) therefore may be underestimated, along with their SI

value. The most acidic of the three Geysir hot springs sampled, IG-19-3 (pH 6.01), was found to

be at saturation with respect to amorphous silica (SI = -0.01), strengthening this interpretation.

Another pathway for silica precipitation could be purely mechanical splashing/wave

action. It is notable that the SI values for all siliceous materials (amorphous silica, cristobalite,

chalcedony, quartz, silica gel) are near saturation with respect to the hot springs studied (Table

10). Therefore, even though silica is precipitating from boiling fluids directly in hot spring pools

(as indicated by the extensively silicified inlet tunnels e.g. Figure 13A-C), this process is likely

quite slow. It is therefore probable that silica precipitation is aided by periods of fluid overflow

from hot springs onto adjacent mud flats. This would cause rapid cooling of the thermal fluid,

lowering silica solubility and causing precipitation. Additionally, capillary action through the

porous muds adjacent to each pool could lead to evaporation and subsequent precipitation of

silica at the surface. These mechanisms may contribute to the growth of layered sinter aprons

that form on the margins of each hot spring (e.g. Figure 13A-C) (Mountain et al. 2003; Tobler et al. 2008; Gangidine et al. 2020).

Silica diagenesis begins with amorphous silica or opal-A, continuing through intermediately crystalline phases (opal-CT), and eventually maturing to quartz (Geilert et al. 2016; Gangidine et al. 2019a). Quartz and tridymite can also form through high-temperature ($\sim$ 900°C) hydrothermal processes, though such temperatures are higher than commonly observed from hot spring fluid manifestations at the surface (Morris et al. 2016). It is possible that the quartz and tridymite present in Geysir sinters is related to a much older iteration of the Geysir hydrothermal system, when average temperatures were higher. Alternatively, the tridymite in our samples may be detrital and related to the evolved volcanic activity present in the area. The fact that tridymite and opal-A are only observed in the "fossil" sinter at Geysir and not in samples from the currently active sinters, and that quartz is only classified as a dominant mineral in the fossil sample, suggests diagenetic maturation since initial deposition.

6.1.4 Geysir: fumaroles

The fumarole mound transect at Geysir revealed mineral assemblages consistent with steam-heated hydrothermal activity including native sulfur, amorphous silica, anatase, pyrite, likely npOx, smectite, and kaolinite (Figure 13; Table 3).

Native sulfur was found precipitating directly from volcanic vapors at the vent, where it is deposited through the reaction of SO_2 with water. This reaction also forms H_2SO_4 condensates that lower soil pH and drive host rock leaching, supplying free cations to the system that are incorporated into secondary minerals (Hynek et al. 2013; McCollom et al. 2013b).

A very shallow (~4 cm) redox gradient was noted 20 cm from the fumarole vent, with

pyrite below and inferred npOx above the gradient. Ferrous iron is highly mobile and readily

forms pyrite in sulfide-rich systems (as described in Section 6.1.1), while ferric iron is highly

insoluble and will readily accumulate as sulfate salt, npOx, or hematite, depending on the

conditions. Whether or not the npOx formed through pyrite oxidation or dissolution and re-

precipitation of other precursor phases (e.g. Fe-sulfates) is unclear. Pyrite oxidation is a multi-

step process whereby iron is preferentially lost relative to sulfide during oxidative dissolution,

resulting in the formation of thin layers of native sulfur and aqueous sulfuric acid. Pyrite

oxidation can be described through the following series of reaction steps, as described by

Strumm and Morgan (1995):

(3) $$FeS_{2(s)} + 2.9O_2 + 0.6H_2O \rightarrow Fe^{2+} + 0.4S^0_{(s)} + 1.6SO_4^{2-} + 1.2H^+$$

(4) $$Fe^{2+} + 0.25O_2 + H^+ \rightarrow Fe^{3+} + 0.5H_2O$$

(5) $$Fe^{3+} + 3H_2O \rightarrow Fe(OH)_{3(s)} + 3H^+$$

(6) $$FeS_2 + 14Fe^{3+} + 8H_2O \rightarrow 15Fe^{2+} + 2SO_4^{2-} + 16H^+$$
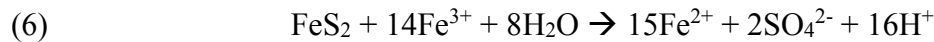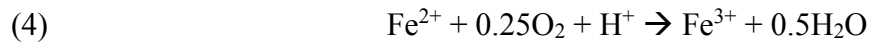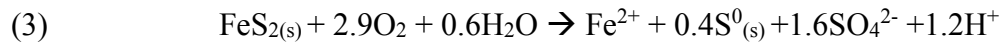
Note that the mobilization of ferrous iron from pyrite releases some acidity, but under

atmospheric conditions oxidation should occur rapidly (*equations 3 and 4*). The ferric iron may

then precipitate as insoluble ferric hydroxide (*equation 5*), or pyrite itself can reduce ferric iron,

resulting in the release of 16 moles of hydrogen per mole of pyrite (*equation 6*; leading to the

deposition of sulfates at low water/rock ratios or release of sulfate, ferrous iron, and acidity, at

high water/rock ratios). According to experimental work by Todd et al. (2003), the resultant iron-

bearing solid that forms is dependent on pH: at pH < 4 ferric hydroxysulfates (e.g. copiapite) are

the main pyrite oxidation products. At pH > 4, ferric oxyhydroxides (e.g. goethite) begin to form

55

as pH continues to increase. However, because Fe-sulfate salts are generally highly soluble, they may easily be dissolved in wet environments and re-precipitated as ferric oxides. Assigning an origin to the npOx therefore requires further study. Nevertheless, the lack of Fe-sulfates and ubiquitous presence of probable npOx at the surface implies a mildly acidic, not hyper-acid fumarole environment.

Accumulation of Si- and Ti-oxides (as amorphous silica and anatase), along with Zr as seen in the Geysir fumarole are characteristic of the removal of more mobile cations from precursor rocks. One sample collected from the fumarole mound contains the highest TiO_2 values observed (IG-19-9, 6.70 wt.% TiO_2; Table 6). Previous investigations of anatase in altered hydrothermal samples support the conclusion that TiO_2 accumulates through the action of acidic hydrothermal fluids as colloidal aggregates rather than homogeneously throughout the precursor rock (Geptner et al. 2007; Smith et al. 2009; Markússon and Stefánsson 2011). The extremely elevated TiO_2 concentrations observed in IG-19-9 relative to altered sediments collected nearby, which ranged from 1.80 – 2.46 wt. % TiO_2, support these interpretations.

6.2 Controls on local variability in alteration products

6.2.1 Parent lithology

Black (2018) and McHenry et al. (2017) note that the bulk composition of the host rock in which a hydrothermal system is located correlates with the resultant secondary mineralogy present on the surface. It follows that in Iceland Fe-bearing phases should be most prevalent (given the elevated iron content of Icelandic basalts relative to most terrestrial basalt), and our observations confirm that this is the case as Fe-sulfates and pyrite are among the most common alteration products observed. However, heterogeneity in host rock composition is evident throughout the region investigated (e.g. this study, Jakobsson 1972; Kaasalainen and Stefánsson

2012; Kaasalainen et al. 2015; Black and Hynek 2018). In the case of Geysir, more evolved magmas have resulted in the accumulation of rhyolite at the surface and near subsurface (Ármannsson 2016). The influence that evolved lavas have on the secondary minerals present at Geysir is unclear. McHenry et al. (2017) observed abundant Al-sulfate minerals as secondary phases forming in the Lassen hydrothermal system, which is hosted in an arc volcanic complex characterized by andesitic to dacitic compositions (which are lower in Fe, Mg, and Ca than basalt, although comparable with respect to Al concentrations). The absence of Al-sulfates and presence of Ca- and Mg-sulfates in the fumaroles sampled at Geysir suggests that rhyolite may not be influencing the mineralogy of the thermal features studied. Nevertheless, the uncertainty regarding host lithology makes it difficult to compare alteration products, particularly when assessing the extent to which acid leaching has accumulated immobile cations (e.g. Si, Ti). Such problems also arise when assessing aqueous alteration histories of Martian sediments, as precursor rock compositions are often poorly constrained, as discussed further in section 7.1.

Ölkelduháls and Nesjavellir are both basalt- or basaltic hyaloclastite-hosted systems, and in spite of local variability, the overall bulk geochemical composition of host rocks is confined to a restricted range (as confirmed to considerable depth based on extensive drilling; Arnason et al. 1969; Gebrehiwot 2005; Natukunda 2005; Jousset et al. 2011; Ármannsson 2016; Nono et al. 2018). This allows for better comparison between alteration products and host rocks with respect to major element composition, as the original composition of the host material can be assumed within a reasonable margin of error. However, the heterogeneity present in host rocks (and subsequent alteration products) is more pronounced for trace elements. Initial concentration of the host lithology, the mineralogical carrier of a particular trace element, hydrothermal fluid composition, and the accessibility of such rocks to the fluids all influence the susceptibility of a

particular trace element to transport and redistribution at the surface. Studies of trace elements in surface hydrothermal systems must therefore consider how the accumulation of trace elements is affected by elemental availability at the source, in addition to intrinsic factors of mobility, pH, etc.

6.1.2 Effect of previous alteration episodes

The age of a geothermal system affects the extent to which modern alteration products and 'original' protoliths can be directly compared. The Hengill volcanic system became active at ~ 400 ka, placing an upper limit on the age of its geothermal system (Gebrehiwot 2005). The volcanic structures associated with Geysir have been dated to ~ 800 ka, also suggesting that geothermal activity has occurred in the region for a long time (Ármannsson 2016). Due to the age of the volcanic deposits in the sites studied, it is possible that the present hydrothermal features are hosted in deposits that have been altered during earlier hydrothermal episodes.

The identification of quartz and tridymite in Geysir sinters and euhedral quartz crystals at Ölkelduháls supports extensive alteration or post-depositional modification at both sites. The degree to which hydrothermal overprinting may have influenced the geochemical composition and mineralogical maturity of our samples, however, is uncertain.

Lynne et al. (2006) note that fumaroles commonly manifest following hot spring systems discharging NaCl waters (and sinters), a result of gradual water table decline that favors volcanic vapor condensation at the near surface. Due to the thermodynamic instability of opal-A in sinters, it has been shown that maturation from opal-A to quartz in silica sinters subjected to acidic fumarolic steam can begin in months. Increasing the crystallinity of silica precipitates also destroys original textures preserved by rapid silicification of microstructures when sinters are deposited. The end result of this process is quartz-rich sinter with etched and pitted dissolution

58

textures, sometimes accompanied by kaolinite (Lynne et al. 2006, 2017; Schinteie et al. 2007). Implications of this process for proposed sinters on Mars are explored in Section 7.1.2.

6.3 Aqueous geochemistry

6.3.1 Steam-heated acid waters

Acid supply (i.e., fluid pH) is a major control on the hydrothermal alteration occurring at the surface. Protons are supplied to hydrothermal fluids through dissociation of H_2SO_4 generated directly through oxidation of magmatic volatiles following this reaction:

(4) $\qquad\qquad 4SO_2 + 4H_2O \rightarrow 3H_2SO_4 + H_2S$ and

(5) $\qquad\qquad\qquad H_2S + 2O_2 \rightarrow H_2SO_4$
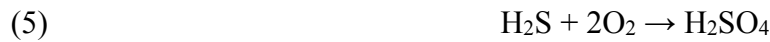
Alternatively, as described in equation (3) (*Section 6.1.4*), pyrite oxidation also supplies a source of H_2SO_4, lowering pH while adding ferrous Fe to the fluid that can rapidly oxidze to Fe_2O_3. Regardless of the source of H^+, lower pH was well-correlated with greater SO_4 concentrations (Figure 15).
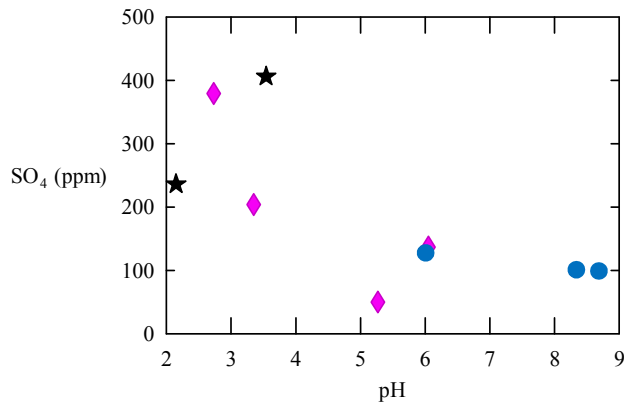
Figure 15: Relationship between SO_4 and pH in hot springs. Higher concentrations of SO_4 are generally correlated with lower pH, indicating the influence of H_2SO_4 dissociation on water pH. Symbols represent each field site. Black stars are Ölkelduháls hot springs, pink diamonds are Nesjavellir hot springs, blue circles are Geysir hot springs.

Many studies indicate that hydrothermal alteration of host rocks at high temperature (in the deeper parts of the hydrothermal system) and low pH (in zones of high steam/water ratios at the surface) is essentially an isochemical process with respect to major rock-forming oxides (Arnórsson et al. 1978; Arnórsson 1995a; Scott et al. 2014; Stefánsson et al. 2016). This can be inferred by measuring the composition of the most acidic hot spring fluids and fumarolic condensates where generally Fe > Al > Ca > Mg. However, fluid compositions are not simply controlled by host rock compositions. Rather, the mobility of a particular element in a thermal pool is foremost related to the secondary fluid-mineral equilibria, with departures from thermodynamic equilibrium explainable through biogeochemical cycling and/or kinetics.

The relationships of various metals with respect to pH are plotted in Figure 16. Most metals, including Mg, Fe, Al, Ca, Cr, Mn, Ni, Ti, V, and Zr, are most highly concentrated in the fluids with lowest pH, consistent with enhanced dissolution of host rocks and elemental mobility when H^+ activity is high. This generalization breaks down somewhat in the neutral to alkaline waters from Geysir (e.g. elevated Al in IG-19-3 and IG-19-5; Table 8). Nevertheless, at pH ≥ ~ 3, the concentration of the elements listed above declines exponenitally compared to the most acidic hot spring waters, indicating signifcantly lower mobility at moderately acidic to near-neutral pH.

As stated previously, elemental mobility is related to the stability of primary minerals under various conditions. In basalt-hosted acid waters, hydrolysis of olivine, pyroxenes, and Ca-plagioclase occurrs spontaneously, releasing ions into solution (Stoiber and Rose 1974; Hynek et al. 2013; McCollom et al. 2013b; Black 2018). If pH is low enough (<< 3), these metals remain dissolved until supersaturation at very low water/rock ratios (seasonally or when water flows

downslope and evaporates). At moderately acidic to near-neutral pH, rock dissolution becomes

incongruent and secondary mineral authigenesis consumes ions, reducing the mobility of most

elements in the thermal waters (Markússon and Stefánsson 2011).
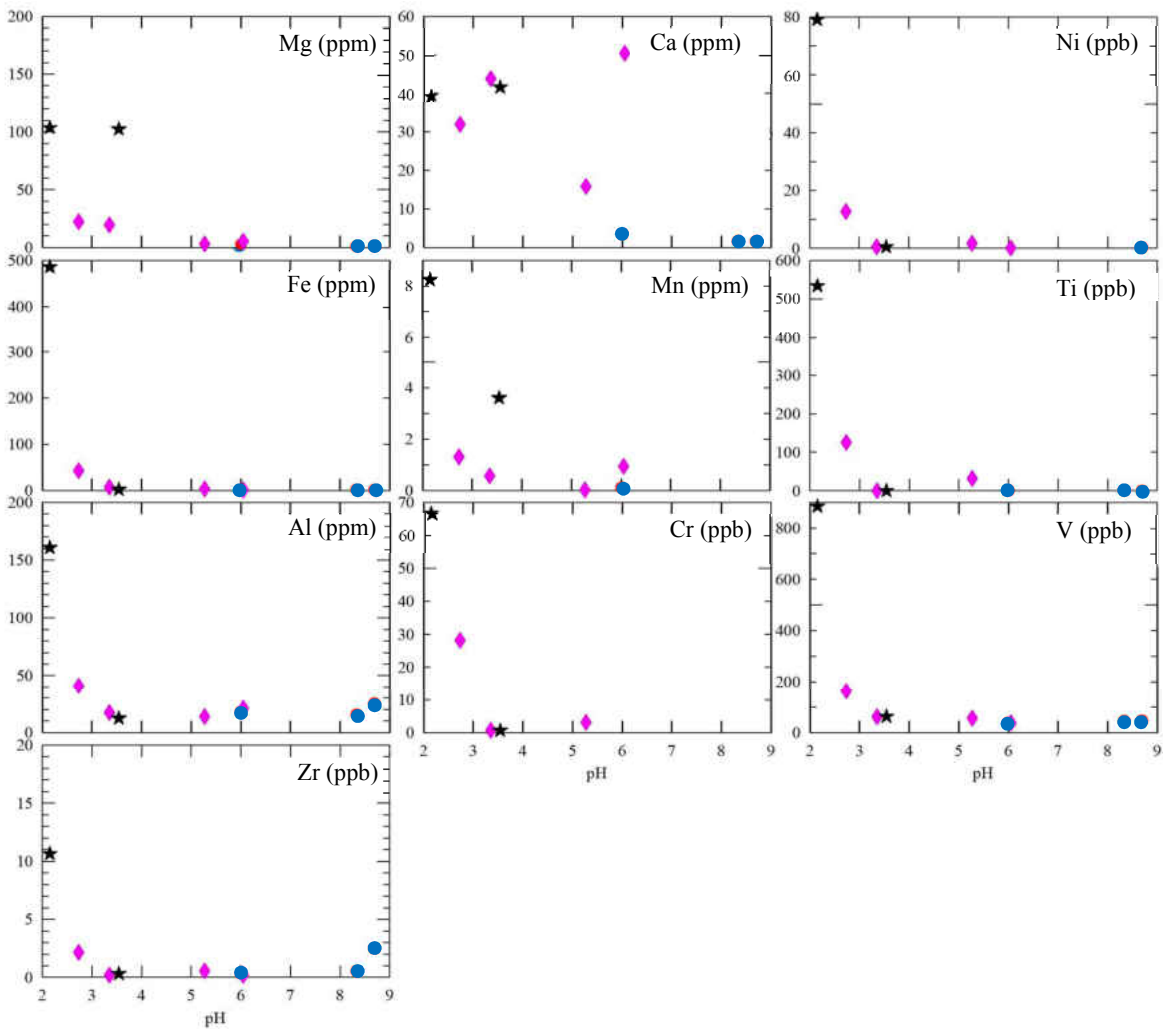
Figure 16: Bivariate plots showing relationship between pH and elemental concentration of Mg, Fe, Al, Ca, Mn, Cr, Ni, Ti, V, and Zr in hot spring waters. These elements follow exponential trends of decreasing concentration with increasing pH. Slight increases in Al, V, and Zr concentrations in alkaline waters suggest slight mobility at higher pH. Cr is below detection (and therefore not plotted) at pH $\geq$ ~5. Symbols represent each field site. Black stars are Ölkelduháls hot springs, pink diamonds are Nesjavellir hot springs, blue circles are Geysir hot springs.

6.3.2 Geysir boiled alkaline waters

Sodium, K, Cl, As, B, Cl, Ga, Ge, and Rb display opposite relationships to those described in Section 6.3.1.1, whereby alkaline fluids at Geysir maintained the highest concentrations. This observation indicates elevated mobility at higher pH and sub-boiling temperatures (Table 8, Figure 17). These elements are likely scavanged from host rocks at depth (where water temperatures exceed 150°C) and carried to the surface where they emerge at hot spring vents. Whether these elements precipitate directly with siliceous sinters/npOx, or become incorporated into their own authigenic minerals, is unclear and requires further trace element characterization of the solids. Given the low concentrations of As, B, Ga, Ge and Rb, however, it is probable that their concentration is primarily controlled through substitution for major ions in secondary minerals. For example, Ge has been shown to follow Si in hydrothermal solutions (Arnorsson 1984; Evans and Derry 2002; Wood and Samson 2006; Lugolobi et al. 2010; Berger et al. 2017), and Ga has been correlated with microbial activity in siliceous sinters from Yellowstone, supporting the hypothesis that Ge and Ga become incorporated into siliceous sinters (Arnorsson 1984; Evans and Derry 2002; Wood and Samson 2006; Lugolobi et al. 2010; Berger et al. 2017; Gangidine et al. 2019). Cl and B are highly mobile and may become incorporated into soluble halides or borates at very low water/rock ratios, neither of which were observed in the present study (Wood and Samson 2006; Kaasalainen and Stefánsson 2012; Kaasalainen et al. 2015, 2017; Pirajno 2020). K and Rb are well-correlated in our water samples (Figure 18), suggesting that Rb may be incorporated into K-bearing secondary minerals. Illite (a K-bearing phyllosilicate), although not observed in our samples (as determined by bulk sample XRD), was found to be oversaturated in four hot spring waters with near-neutral to alkaline pH (Table 10), providing a potential sink for both K and Rb.
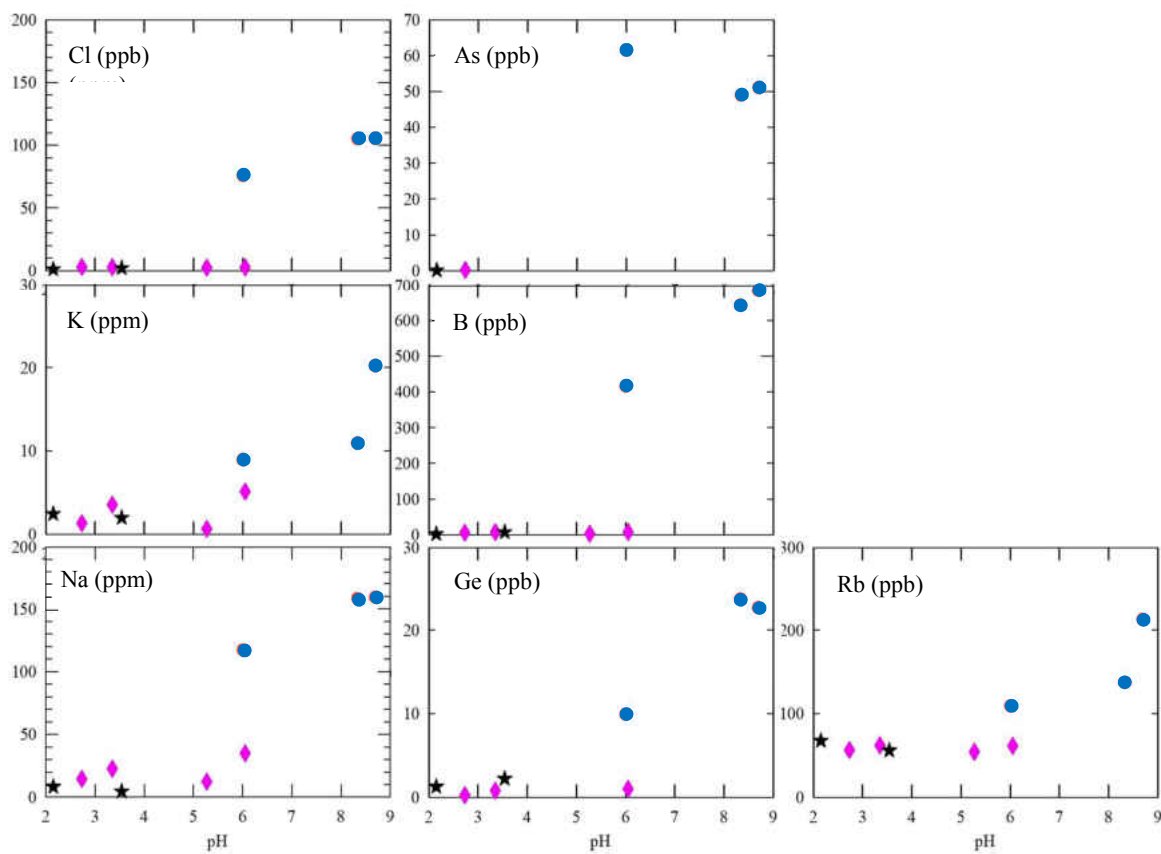
Figure 17: Bivariate plots showing relationship between pH and elemental concentration of Cl, K, Na, Ge, B, As, and Rb in hot spring waters. These elements were generally correlated with alkaline waters, indicating their boiled aquifer water source. Arsenic was below detection in all but the most acidic waters, and the waters sampled at Geysir (see Table S2 for LODs). Symbols follow same pattern as Figure 16.

6.3.3 Alkaline earth metals: Ca, Sr, Ba

Our observations imply that Ca and Sr do not adhere to the general trends described above between pH and concentration across any of the sites studied. Previous studies indicate that Ca has similar mobility to other major rock-forming elements, and its concentration in thermal fluids is controlled by rock leaching (Humphris and Thompson 1978; Arnorsson et al. 1982; Markússon and Stefánsson 2011; Kaasalainen and Stefánsson 2012; Björke et al. 2015; Kaasalainen et al. 2015). The controls on mobility/concentration of Ca in our samples is therefore uncertain. Ca concentrations are surprisingly consistent between all hot springs (31.97 – 50.42 ppm) except the three hot springs sampled at Geysir, where its concentration is low (~1-

3 ppm). This observation indeed suggests that Ca is sourced through acidic leaching of host rocks, though the reason for its divergence from the trend followed by other metals in steam-heated springs is unclear. A possible near-surface source of Ca (e.g., a buried gypsum deposit) for IN-19-11 may explain why this near-neutral spring has the highest Ca concentrations across all samples (Table 8). The observation of gypsum and anhydrite associated with this hot spring supports this hypothesis, although the subsurface was not sampled. However, ignoring IN-19-11 (pink diamond, pH = 6), the rest of the data plotted in Figure 17 shows a strong Ca-pH correlation for the rest of the waters.

We also note strong correlation between Ca and Sr in altered solids and fluids across all field sites (Figure 19), consistent with its probable substitution for Ca in secondary minerals (e.g. carbonates, sulfates, aluminosilicates). Sr was slightly oversaturated in one hot spring (IN-19-7, as celestine [$SrSO_4$]; Table 10), although the concentration of Sr is quite low, suggesting minimal accumulation as a pure mineral phase. Barium can also substitute for Ca in carbonates and sulfates or precipitate directly as barite (Kaasalainen and Stefánsson 2012). Barite was either supersaturated or near saturation in all of our samples indicating its precipitation, although barite is not observed in any of our samples. This may be due to the low availability of Ba in the environment, or barite precipitation may be kinetically impeded. Nevertheless, Ba shows good
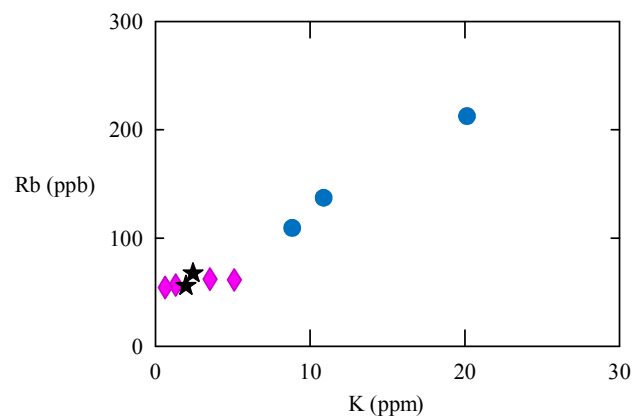
Figure 18: Rb concentrations plotted against K in thermal waters. Symbols are same as in Figure 16.

64

correlation with SO$_4$ (Figure 19), implying that its concentration may be controlled by barite saturation.
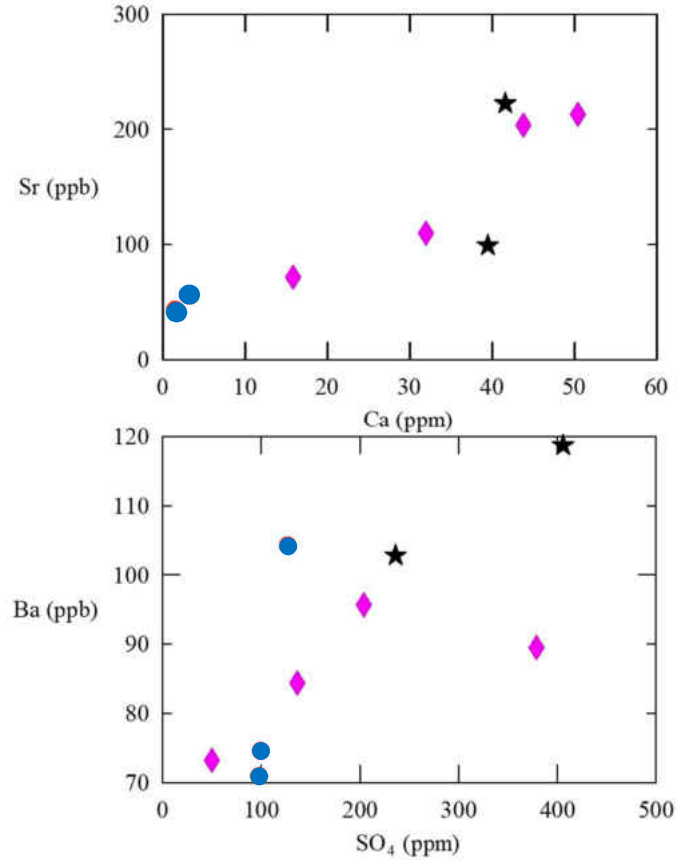
Figure 19: (top) Sr and Ca concentrations in hot spring waters, and (bottom) Ba and SO$_4$. Symbols are same as in Figure 16.

6.3.4 Silica solubility in acid waters

Determining the behavior of silica in acid-sulfate hydrothermal fluids is challenging. Silica is generally considered insoluble at low pH, and is often used in conjunction with anatase, sulfur, etc. as an indicator of acidic hydrothermal conditions (Squyres et al. 2008; Ruff et al. 2011; McCollom et al. 2013a; McCanta et al. 2014; Rodríguez and van Bergen 2015; McHenry et al. 2017a; Flahaut et al. 2019). However, silica concentrations were moderately high across all

pH ranges (Table 8), consistent with its pH-independent solubility. Although often considered to accumulate as residue, it does not correlate well with TiO_2 or Zr in our solid samples (discussed further in *Section 6.4.1*). Furthermore, thin crusts overlying soils adjacent to acidic springs/fumaroles (e.g. IN-19-9, IG-19-8) contained silica as major or accessory phases (quartz or amorphous silica). These surface crusts did not appear to be leached residue associated with host rocks, and were easily separated from the altered soils below, suggesting that they were precipitated crusts of silica. Observations of silica-rich surface crusts associated with acid hot springs and fumaroles, and possibly authigenic quartz forming from acidic waters (e.g. IO-19-21) challenge interpretations that consider SiO_2 as an insoluble oxide at low pH. Experimental studies by (Tosca et al. 2004) determined that hydrolysis of olivine at low pH releases aqueous silica into solution that quickly reaches saturation with respect to amorphous silica. Their results seem consistent with our observations of silica crusts forming on the surface of hot springs/fumaroles where acidity is high, and may indicate that silica is redistributed on small scales at low pH, rather than being carried from depth, as is the case in boiled alkaline waters. Silica phases were often supersaturated in our geochemical calculations (Table 10), supporting accumulation of silica by precipitation and as residue.

It is also worth noting that the mobility of silica at each site may be affected by the composition of the host. For example, basaltic volcanic glass (e.g. sideromelane, common in hyaloclastite) is highly reactive (Bloise et al. 2017) and would readily alter under hydrothermal conditions, presumably releasing dissolved silica (among other metal oxides) to the fluid. This stands in contrast to quartz, which is common in evolved lavas, and is considered stable under most conditions. Rutledge et al. (2018) studied glacial meltwaters associated with volcanic bedrock in the Cascade mountains, finding that waters in contact with mafic substrates had

significantly higher dissolved silica than those associated with felsic rocks. Although Rutledge et al. (2018) studied low-temperature to ambient fluids, these principles should still hold under hydrothermal conditions.

6.4 Geochemical patterns of acid-sulfate alteration

Acid sulfate alteration of host rocks produced the following mineral assemblages (Table**s** 3 and 4):

Group (1)   Mixtures of disseminated leached host rocks and authigenic clays containing a silica phase (quartz or amorphous silica) ± anatase + smectite and/or kaolinite and either pyrite (below a shallow redox gradient) or likely npOx (above a shallow redox gradient).

Group (2)   Grey to black muds floating on the surface or just beneath the water surface of steam-heated hot springs containing pyrite + smectite and/or kaolinite. Accessory phases typically included quartz, amorphous silica, and anatase, though these are likely leached alteration products entrained in the primarily authigenically-derived hot spring mud.

Group (3)   Surface crusts/precipitates in intermittent to constant contact with volcanic vapors, hot spring fluids, or soil solutions, containing mixtures of sulfates (Fe-, Mg-, Ca-) and in some cases intermixed with accessory amorphous silica, native sulfur, anatase, and/or npOx.

The geochemical trends defining each of these solid sample types are described in Sections 6.4.1 – 6.4.2.

6.4.1 Groups 1 and 2: leached soils and altered muds

Groups 1 and 2 are two groups of alteration products defined by the progressive leaching of host rocks and the formation of authigenic minerals. TiO_2 and Zr are considered insoluble under acidic conditions (Humphris and Thompson 1978; Rubin et al. 1993; Markússon and

Stefánsson 2011; McHenry et al. 2017), and the residual accumulation of these elements is characteristic of leaching-dominated alteration regimes. However, this assumption is challenged by the observation of small amounts of Ti and Zr in acid waters (Table 8), indicating partial solubility. Nevertheless, the linear relationship between TiO_2 and Zr in solids is demonstrated in Figure 20, indicating that these elements accumulate as residue under acidic conditions.

If it is assumed that Zr is not removed from host rocks subjected to acidic fluids, its concentration can be plotted against that of other elements to assess the behavior of those elements under acid-sulfate conditions, as seen in Figures 20 and 21. Aluminum shows a loose correlation with Zr, suggesting that is is immobile under all but the most acidic conditions (pH < 2.5, e.g., Markusson & Stefánsson 2011). However, Al can also be sequestered in Al-phyllosilicates (e.g. kaolinite, a common alteration product) or oxyhydroxides, elevating its concentration. Fe_2O_3 may also be added (as pyrite or npOx) or removed, though it has been observed to be more mobile than Al_2O_3. Other oxides including MnO, MgO, CaO, Na_2O, and K_2O were all leached out of host rocks to varying degrees, consistent with their relatively high mobility under acidic conditions. These oxides had generally inverse relationships to Zr concentrations, and are not included in Figure 20 or 21. Magnesium oxide, CaO, and MnO may be incorporated into smectites, if present, although their accumulation is lesser than that of Al_2O_3 or Fe_2O_3 given the relatively acidic conditions across the study areas impeding smectite formation (Berger and Velde 1992).

Spider plots for disseminated, leached soils and subaqueous muds are shown in Figure 22. These plots show relative enrichment and depletion patterns of major oxides (and Zr) normalized to median Icelandic basalt concentrations (Kaasalainen and Stefánsson 2012). The relative enrichments of TiO_2 and Zr are again consistent with their accumulation as residue.

Al$_2$O$_3$ was either largely unchanged compared to basalt or 'enriched' through its incomplete removal or addition into authigenic phases. Fe$_2$O$_3$ followed a similar pattern, but given its higher mobility was more often depleted in the leached sediments, and was 'enriched' in subaqueous muds due to its addition (as pyrite). P$_2$O$_5$ is enriched in all altered samples, but the extreme enrichment shown in these diagrams can be attributed to the very low P$_2$O$_5$ concentrations in the median Icelandic basalt (0.02 wt. %, used as the "unaltered" substrate in these diagrams), compared to the much higher P$_2$O$_5$ concentrations measured in the local substrate samples for Nesjavellir (0.25 wt%) and Ölkelduháls (0.08 wt %). These more modest enrichments (wt. % up to 0.56) can be attributed to the update of P$_2$O$_5$ into secondary minerals, though no P-bearing phases were directly observed.
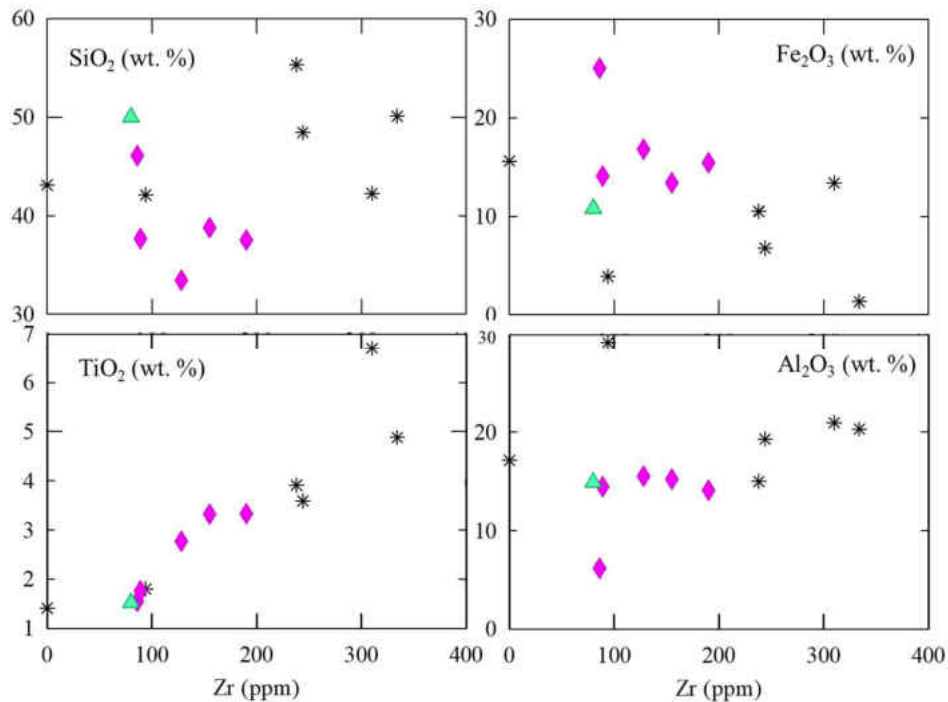
Figure 20: SiO$_2$, TiO$_2$, Fe$_2$O$_3$, and Al$_2$O$_3$ concentrations plotted against Zr in group 1 (black asterisks) and group 2 (pink diamonds) solids, along with median Icelandic basalt values from Kaasalainen & Stefansson (2012) (green triangles).

69
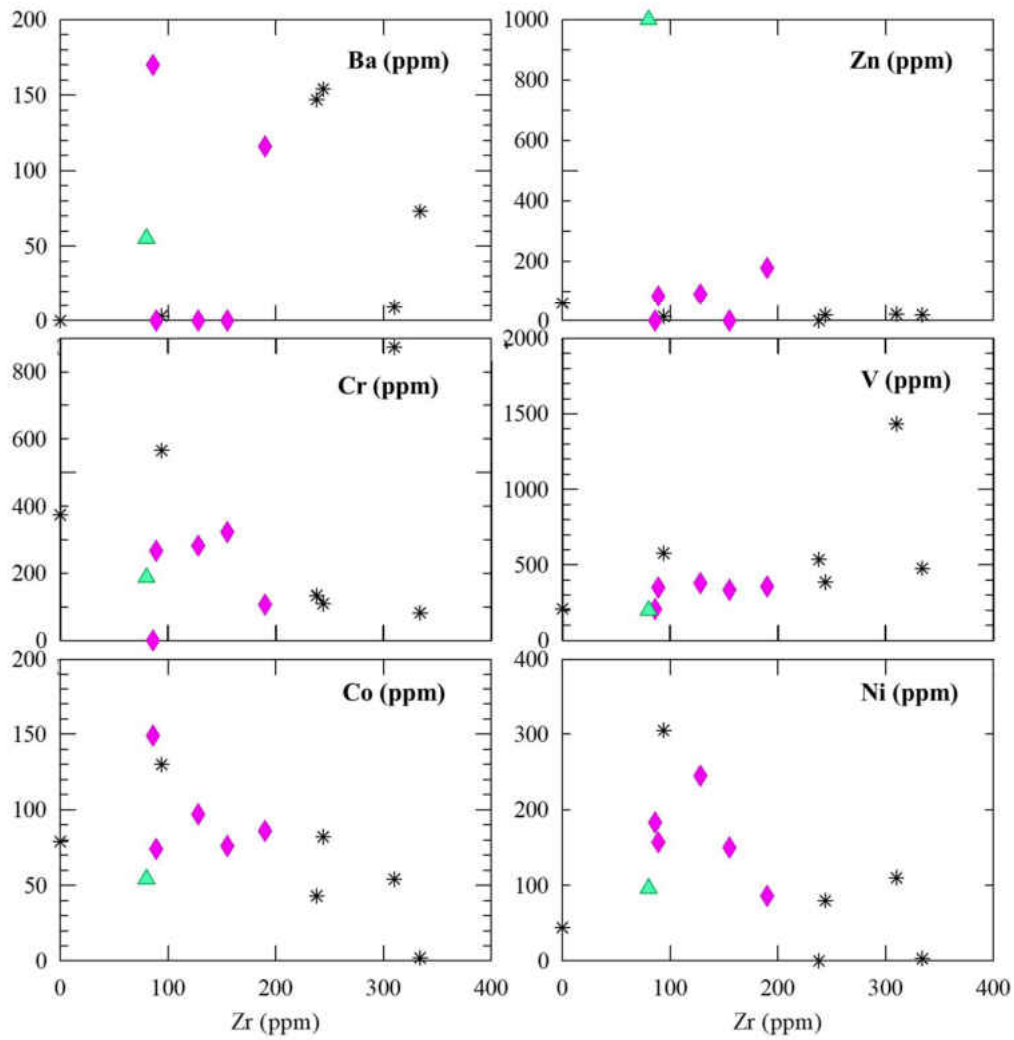
Figure 21: Zirconium concentrations plotted against Ba, Cr, Co, Zn, V, and Ni for solid samples. Symbols are same as in Figure 20.
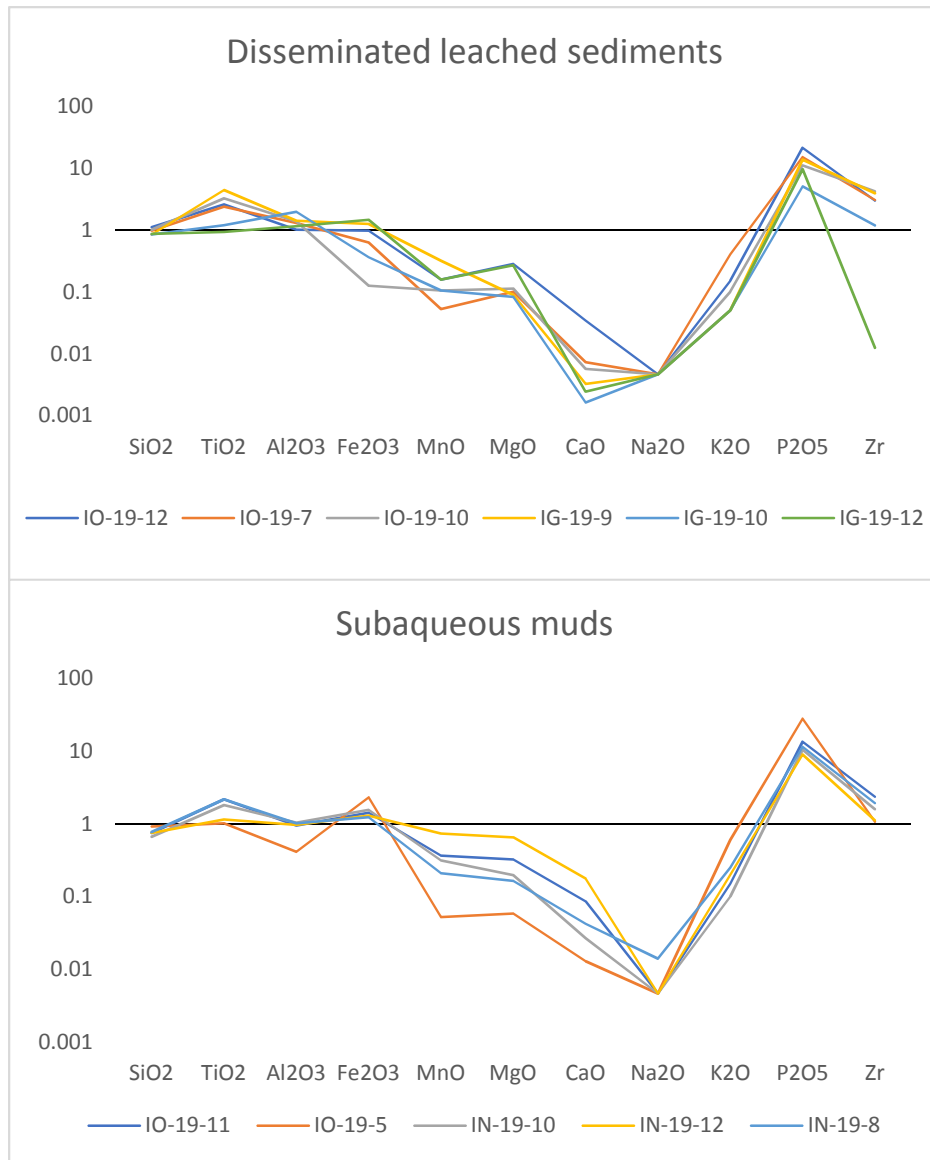
Figure 22: Spider plots for subaqueous muds and leached sediments normalized to median Icelandic basalt values reported in Kaasalainen & Stefánsson (2012) indicating relative enrichment or depletion of major oxides + Zr. Values > 1 indicate higher concentrations relative to basalt, while values < 1 indicate lower concentrations. A value of 1 indicates no difference.

The degree of accumulation or depletion of elements in leached sediments for

Ölkelduháls (IO-19-12, IO-19-7, IO-19-10) and the Geysir fumarole mound (IG-19-9, IG-19-10,

IG-19-12) was not the same. Ölkelduháls leached soils generally had higher SiO_2, TiO_2, and Zr

by weight than those from Geysir, but lower Al_2O_3 and Fe_2O_3 (Table 6). This could be related to

71

the differences in water availability between each site. At Ölkelduháls, high availability of acidic fluids can effectively remove elements, and can entrain and remove authigenic minerals after their formation. In fumarolic settings (such as at Geysir), availability of water is much lower, which slows down leaching of soluble phases despite high acid supply and would prevent post-depositional transport of authigenic minerals. Alternatively, the dominance of clays in the Geysir fumarole mound compared to Ölkelduháls, which had more quartz, could help explain these compositional differences. The kaolinite and smectite from Ölkelduháls would help concentrate Al_2O_3, while higher silica would be expected in quartz-rich samples.

As described in Section 6.3.1, the behavior of metals including Ba, Cr, Co, Ni, V, and Zn is ultimately controlled by host-rock leaching in acidic settings, explaining their higher concentrations in the most acidic waters (Table 8). Their mobilities are all likely greater than that of Zr, and they appear to be removed non-stoichiometrically under all but the most acidic conditions, based on their somewhat scattered relationships seen in Figure 21. Although it appears that the accumulation of many trace elments may be highly source-controlled, some general trends were still observed. V seems to be relatively resistant to acid leaching, and was correlated with higher Zr concentrations. Nickel, Co, Cr, and particularly, Zn, showed the opposite trends, inversely correlated with Zr. Trends with Ba were difficult to discern, and this may be related to its moderate mobility and incorporation into secondary minerals.

The gradual depletion of Ni and Cr is consistent with other studies that have observed these species to be only moderately resistant to acid leaching (Humphris and Thompson 1978; Ming et al. 2006). This suggests that Ni and Cr become readily incorporated into secondary minerals. Ni is commonly known to precipitate with sulfides (Ewers and Keays 1977; Kaasalainen et al. 2015; Libbey and Williams-Jones 2016; Fontboté et al. 2017), and Cr forms

oxides, though no Ni- or Cr-bearing minerals were observed. Again, however, the relative abundance of trace elements in secondary alteration products appears to be directly tied to the composition of the source rock.

6.4.2 Group 3: surface precipitates

Due to the difficulties in developing a sulfur calibration using XRF techniques, the geochemical data on sulfur-rich minerals are limited in this study. IN-19-2 and IO-19-13 were the only two 'pure' sulfate mineral mixtures analyzed for sulfur, and selected trace element concentrations for these samples are reported in Table 7. Vanadium and Zn were both present in small amounts in IN-19-2 (215 and 111 ppm, respectively), which contained halotrichite group minerals, indicating their incorporation into sulfates. IO-19-13 (a mixture of Fe-, Mg- and Al-sulfates) contained negligible amounts of most trace metals. The minor amount of Zr present in IO-19-13 (80 ppm) suggests that a small amount of leached material may be mixed in with this sample, which was collected from the surface of a clay-rich mound. The incorporation of Zr into sulfates cannot be ruled out, however. Other sulfate or native sulfur-containing alteration samples were either not analyzed or else were significantly mixed with altered/leached sediments (from groups 1 and 2). Determining where the trace elements in these samples reside is therefore not possible using this data. More work must be done to characterize how trace metals are substituted into sulfate minerals.

6.5 Overall conceptual models of surface hydrothermal alteration

The overall controls on hydrothermal alteration, as described above, include elemental mobility under variable fluid conditions, host lithology, maturity of the system, extent of mixing between end-member water types, and volatile/heat supply (Markússon and Stefánsson 2011; Björke et al. 2015). Each area hosted unique expressions of such processes, and a summary of

the findings is provided below in Sections 6.5.1 – 6.5.4 along with an overall conceptual model that accounts for the primary observations and interpretations from each site.

6.5.1 Ölkelduháls hydrothermal system

The mineral assemblages and geochemical patterns observed at Ölkelduháls are governed by steam-heating of local CO_2-rich groundwater (observed in previous studies; Natukunda 2005), the mobility of elements under acid to moderately acid (pH ~ 2 – 3.5) conditions, interaction of thermal fluids with both basalt/hyaloclastite and previously altered deposits, and the mixing of volcanic vapors and groundwater. These processes manifest in various ways throughout the area. Input and oxidation of magmatic volatiles (predominantly SO_2/S^{2-}) across the site supply protons in both surface hot springs and soils. Although soil solution composition was not determined, previous studies of soils in Icelandic hydrothermal areas indicate high acidity and sulfate concentrations in near-surface soils (Kaasalainen and Stefánsson 2012). The end result is large areas of hydrothermally altered ground dominated by clays (smectite/kaolinite) and pyrite, with sulfates accumulating at the surface as seen in our XRD results (Tables 3 and 4). Whether or not sulfates have formed through oxidation of pyrite or evaporation of acidic soil solutions is unclear, and a combination of both processes is possible (Robinson 2000; Todd et al. 2003; Liu et al. 2008; Tabelin et al. 2012).

The differences in acidity between the two springs explains the higher concentrations of most metals in IO-19-21 (pH ~ 2) compared to IO-19-22 (pH ~ 3.5) (Table 8), and the accumulation of TiO_2- and Zr-rich residue. Such observations highlight the highly variable flow of heat, volatiles, and fluids in the subsurface that leads to vastly different fluid chemistry in two adjacent hot springs. A simplified conceptual model of the Ölkelduháls hot springs is shown in Figure 23.
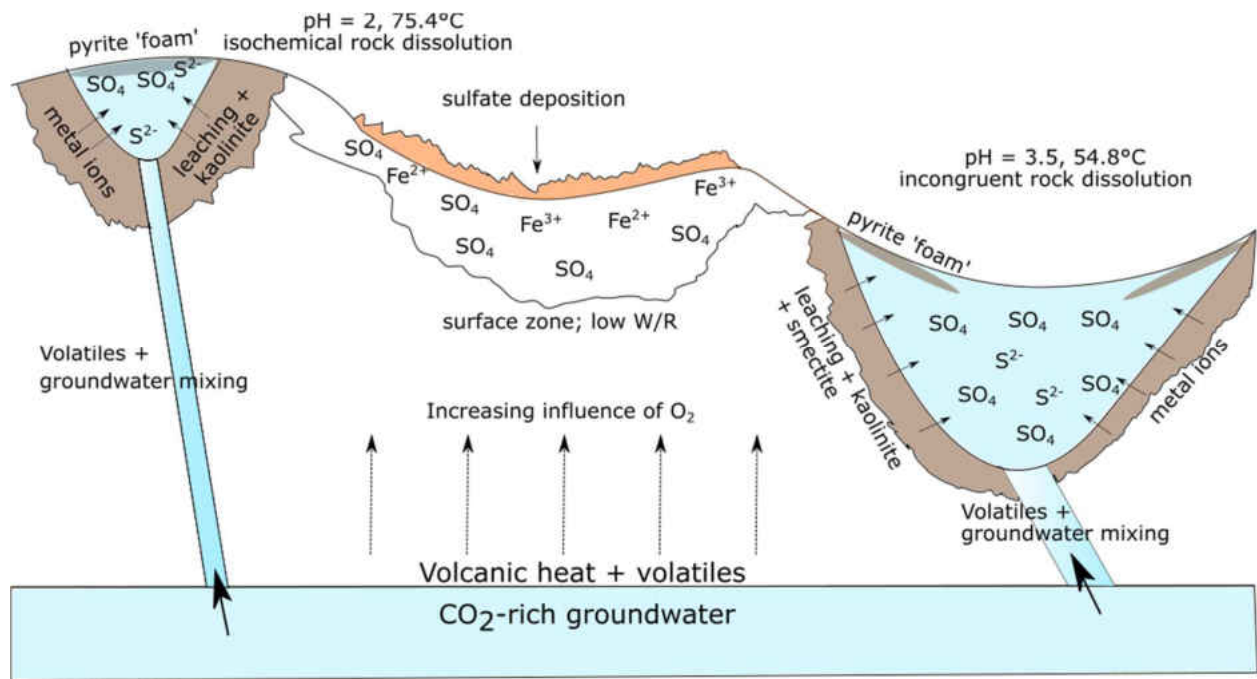
Figure 23: Conceptual model demonstrating formation of two hot springs at Ölkelduháls (IO-19-21, left and IO-19-22, right). Both represent local groundwater mixed with magmatic volatiles. The lower pH of IO-19-21 could be related to the lesser volume of water compared to IO-19-22 (i.e., less dilution of sulfuric acid). This controls the overall chemical conditions of each spring, as most metals are mobile in IO-19-21 and readily leached from host rocks, while the slightly elevated pH of 3.5 in IO-19-22 precludes isochemical rock dissolution. Surface Fe-sulfates (Table 3) on a small mound between the hot springs could reflect evaporation of acidic soil solutions, oxidation of pyrite, or both processes.

6.5.2 Nesjavellir: steam-heated hot springs

The interaction between the three distinct hot spring pools sampled at Nesjavellir (IN-19-6, IN-19-7, and IN-19-11) leads to a unique water chemistry gradient across the area. IN-19-6

was the most acidic of the three hot springs (pH = 2.7), and appeared to flow into and mix with IN-19-7 (pH = 3.35), which in turn appeared to mix with IN-19-11 (pH = 6). Although higher sulfate concentrations correlate with lower pH between these three hot springs, temperature does not, as the near-neutral IN-19-11 was the hottest of the three implying decoupled flow of heat and volatiles in the subsurface.

The elevated metal concentrations seen in IN-19-6 (Table 8) are consistent with its low pH driving rock dissolution, and a TiO_2- and Zr-rich crust was associated with this spring again demonstrating leaching. All three springs are steam-heated hot springs, and their chemical conditions are ultimately driven by dissolution of host rocks resulting from the input of magmatic volatiles to meteoric water. The unique chemical composition of each spring does not suggest that mixing is a dominant process occurring between each spring. One surprising observation was that the apparently largest, near-neutral spring (IN-19-11; pH =6.05) also had the highest temperature of the three (at 86.0°C). This indicates dilution of acidity by meteoric water input, but also decoupled flow of heat and volatiles in the near subsurface. In this case, more heat is partitioned into IN-19-11, but a higher flux of volatiles is partitioned into IN-19-6 and IN-19-7, resulting in their acidic conditions.

As is common in all steam-heated hot springs throughout the study areas, pyrite was detected in 'foamy' mud floating on the surface of each spring despite oxidizing conditions observed in our in-situ measurements (Table 9), along with smectite and/or kaolinite. As discussed in Section 6.3.3, the exact reason for the elevated Ca concentrations in IN-19-11 compared to the other two hot springs is uncertain. A possible near-surface soluble Ca source, such as a buried gypsum deposit, which are commonly observed as products of surface hydrothermal alteration throughout Iceland and elsewhere (Geptner et al. 2007; Hynek et al.

76

2013; Carson 2015; Black 2018), can explain this observation. This can also provide an

explanation for the presence of gypsum in mud floating on the surface of IN-19-11 (solid sample

IN-19-12; Tables 3 and 4) despite it being undersaturated in the SI calculations. A simplified

schematic model demonstrating the manifestation and interaction of all three hot spring is shown

in Figure 24.
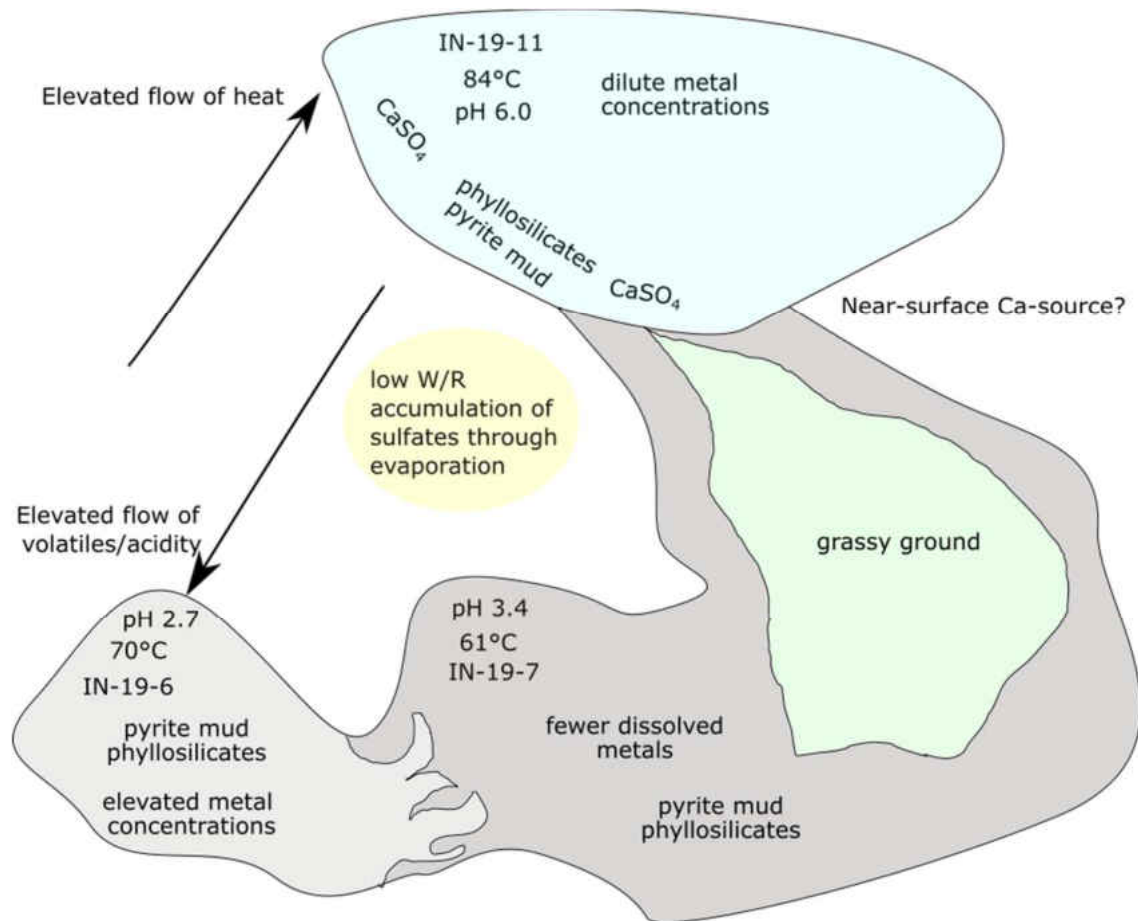
Figure 24: Simplified conceptual model demonstrating relationships between IN-19-6, IN-19-7, and IN-1911. As at Ölkelduháls, the most acidic spring (IN-19-6) is the spring with the least apparent water volume, while the largest hot spring approaches neutral pH (IN-19-11). Each spring appears to flow into the next, although the distinct chemical conditions of each water implies that mixing may be minimal. All three springs are characterized by floating mud containing pyrite and phyllosilicates, and IN-19-11 also has gypsum. Sulfates were observed subaerially on a small ledge in between the three springs, and included halotrichite group minerals and anhydrite. The high temperature and near-neutral pH of IN-19-11 contrasts with the cooler temperature and low pH of IN-19-6, implying decoupled heat/volatile flow in the subsurface.

6.5.3 Geysir: Boiled alkaline hot springs

The alkaline hot springs at Geysir (IG-19-1 and IG-19-5) represent the boiled geothermal aquifer water that has risen to the surface through zones of high permeability mixed with variable amounts of magmatic volatiles. The water is therefore rich in mobile elements partitioned into the boiled aquifer liquid (e.g. Na, Cl) and contains moderate amounts of SO_4 (Table 8). These waters are also relatively SiO_2-rich, a result of host rock dissolution at depth where aquifer temperatures are high (Arnorsson 1975; Arnorsson et al. 1978, 1982). As discussed in Section 6.1.3, deposition of silica sinters at the surface occur at near equilibrium conditions, gradually entombing the inlet tunnels with silica. Rapid deposition can occur where splashing/wave action lowers the temperatures of water droplets, leading to the formation of an apron of siliceous sinter surrounding the spring, as seen in Figure 13A,C (Jones and Renaut 2003; Mountain et al. 2003; Lynne et al. 2017). The sampled silica sinters were found to have low concentrations of all oxides/elements (except silica; Table 6). Silica sinter chips unassociated with active springs are scattered around the thermal area and suggest previous manifestations of alkaline hot spring systems that have migrated through time. One such piece of a broken sinter chip (IG-19-15) was determined to contain quartz and opal-A (Table 3), indicating elevated diagenetic maturity consistent with its association with an older spring. This sample also contained tridymite, however, which forms under high-temperature conditions, whether volcanic or hydrothermal (870 – 1470°C; Morris et al. 2016). The temperatures of formation for tridymite are considered to be far greater than the near-boiling temperatures of the surface hydrothermal conditions at present. However, McHenry et al. (2017) and Wanta (2018) note abundant tridymite in amorphous silica-rich samples at Lassen Volcanic National Park, CA and suggest that tridymite formation through low-temperature (i.e., boiling to sub-boiling)

hydrothermal fluids may be possible. A conceptual model for the formation of silica sinters in

alkaline hot springs at Geysir is provided in Figure 25.
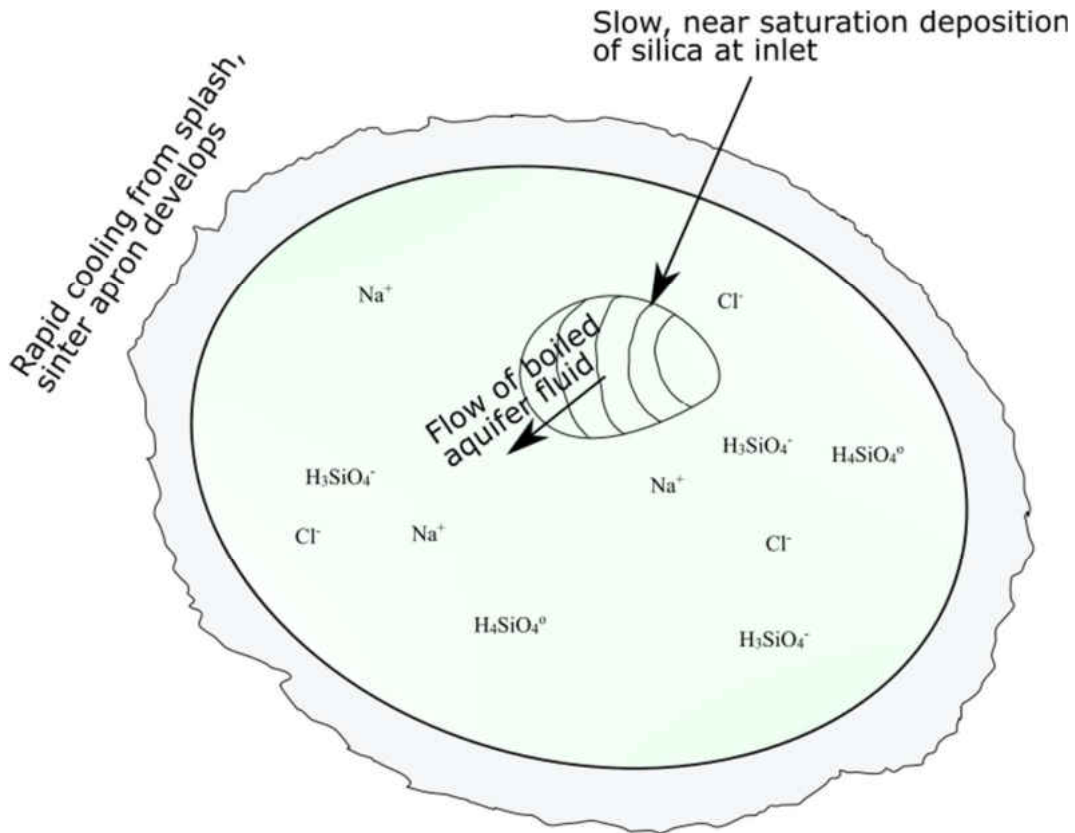
Figure 25: Simplified conceptual model depicting flow of aquifer fluid and formation of sinter aprons in alkaline hot springs (e.g. IG-19-1, IG-19-5). Silica is near saturation with respect to the water, causing slow accumulation under the water surface. Where water splashes along the margins of the spring it cools rapidly and forms layered sinter deposits surrounding its extent.

The sub-neutral (pH = 6) hot spring sampled at Geysir (IG-19-3) presents an interesting

case where signatures of both acidic hot spring fluids and boiled alkaline aquifer fluids are

present. The hot spring was recessed in a ~0.5 m deep cavity in the ground, where it appeared to

have tunneled through the sediment, depositing layered, red-stained silica sinter. Whether its

current subsurface position is related to declining water table through time or entrainment and

removal of near-surface sediment is unclear. However, the sinter itself (IG-19-4) had elevated

concentrations of Ba, Zn, and Zr (all up to a few hundred ppm; Table 7) relative to other sinter samples. The accumulation of these elements can be explained by their relative mobility under different conditions. It is evident that the IG-19-3 spring represents a boiled aquifer fluid given its elevated concentration of the mobile elements Na, Cl, and B and its location near other alkaline thermal features at Geysir. Its slightly acidic pH is caused by a relatively higher ratio of volcanic steam compared to the alkaline springs in the area. Ba, Zn, and Zr are all observed to be somewhat mobile under the hot, alkaline conditions in the deep subsurface (Rubin et al. 1993; Kaasalainen et al. 2015). Their accumulation is noted in downhole well samples prior to boiling and depressurization in Iceland (Hardardóttir et al. 2009), suggesting their accumulation in secondary minerals at depth and transport under alkaline conditions. Since IG-19-3 has maintained its alkaline character until reaching the near-surface (where it mixes with volcanic vapors), these metals may approach saturation upon addition of acid (H_2SO_4) and cooling along with SiO_2, and become incorporated into sinters or secondary minerals. Barite is just oversaturated in our geochemical calculations, supporting this hypothesis, at least with respect to Ba, although determining the source of trace metals in these sinters would require more detailed analysis. A conceptual model demonstrating the formation of the mixed spring at Geysir is provided in Figure 26.
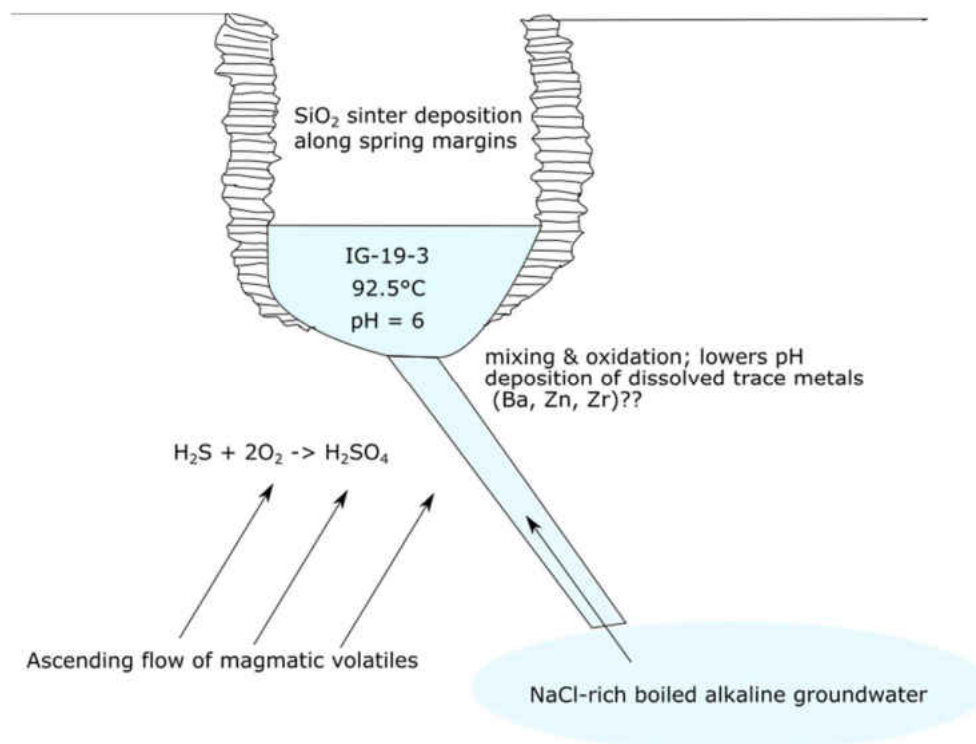
Figure 26: Conceptual model demonstrating hypothesized formation of IG-19-3, a near-neutral hot spring considered to be boiled aquifer fluid mixed with magmatic volatiles.

6.5.4 Geysir: fumarole alteration model

Geochemical and mineralogical trends associated with leaching and precipitation of metals from host rock at low water-rock ratios in the Geysir fumarole are consistent with previous studies of fumarolic alteration (Stoiber and Rose 1974; Papike et al. 1991; Hynek et al. 2013; McCollom et al. 2013a; Carson 2015; McHenry et al. 2017; Black 2018), and reflect similar processes to those occurring in steam-heated hot springs settings albeit with restricted water availability. However, the ambiguity regarding host lithology introduces some complexity, as do the relatively high annual rates of rain/snowfall in Iceland which likely dissolve some of the more soluble alteration products rapidly (Papike et al. 1991). Our bulk analyses are further complicated by the coexistence of authigenic phases with leached residue, making definitive interpretations of elemental gains/losses difficult. Nevertheless, mineral compositions and

81

selected geochemical analyses revealed distinct trends of enrichment of insoluble phases, mobilization of metals, and secondary mineral authigenesis.

The vent of the fumarole defines a zone of high volatile input and partial oxidation of sulfide to native sulfur and sulfuric acid (see Section 6.1.4). The very shallow redox gradient observed 20 cm from the vent defined by the transition of pyrite to npOx near the surface also implies high volatile supply, which mitigates the influence of atmospheric O_2 on the alteration assemblage until near the surface. Above this 4 cm deep oxidation front, npOx appears to form from oxidation of pyrite, which is another source of H_2SO_4 that can lead to additional acid leaching of host rocks (*as described in equations 3 - 6, section 6.1.4*; Liu et al. 2008; Tabelin et al. 2012). The minor presence of sulfur-bearing pyrite oxidation products (e.g. native sulfur/sulfates) indicates that sulfur is being removed from the fumarole mound by runoff attributed to rain or snowfall. Nevertheless, the abundance of smectite, kaolinite, and pyrite and the relative lack of amorphous silica or quartz, along with lower concentrations of Si, Ti, and Zr than in other leached sites sampled, could indicate that conditions at this fumarole, while highly reducing except for at the very surface, are less acidic than at others. That npOx, rather than Fe-sulfates, appear to form directly through pyrite oxidation near the surface implies only mildly acidic conditions in this fumarole ($\geq \sim 4$; Liu et al. 2006), supporting this hypothesis. This stands in contrast to the hyper-acid environments typically associated with fumaroles (e.g. Stoiber and Rose 1974; Papike et al. 1991; Hynek et al. 2013; McCollom et al. 2013a; Flahaut et al. 2019).

The accumulation of kaolinite and smectite in the sediments associated with the fumarole did not seem to follow any trend with or relationship to distance from vent or oxidation front. Thus, it seems that the fumarole mound overlies previously altered ground, and some of the phyllosilicates observed could be associated with previous episodes within the thermal system.

This means that the functional "substrate" for the current episode of hydrothermal alteration may

be clay-rich residue from previous episodes, and that some of these phases may have formed

under conditions different from those observed at present. A model that accounts for these

observations and interpretations is provided in Figure 27.
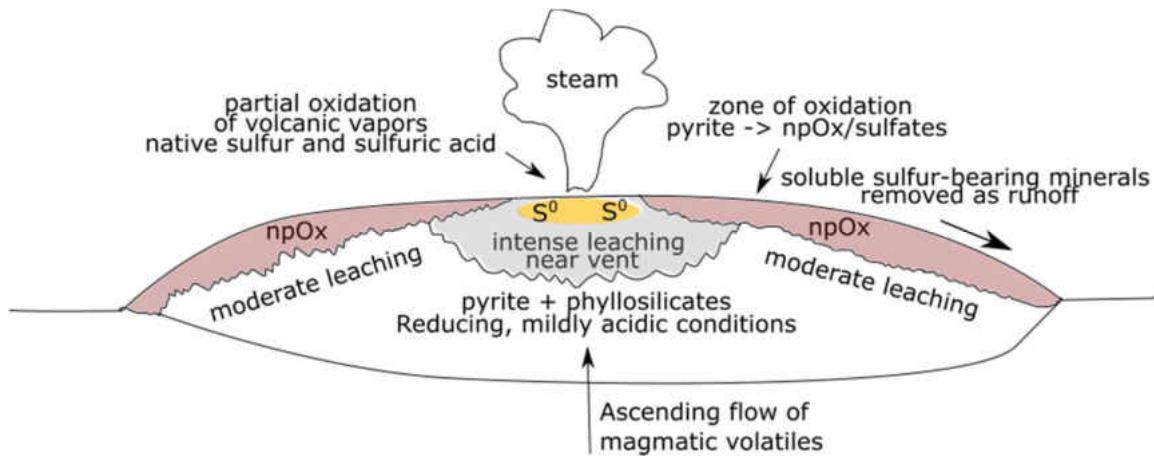
Figure 27: Simplified conceptual model explaining trends in geochemical/mineral composition of altered solids from the fumarole mound at Geysir. Leaching appears to only be intensive nearest the vent, where oxidation of sulfur-rich gases leads to native sulfur deposition and the generation of acidity. The surface zone is characterized by the transition from pyrite to npOx, with open-system removal of sulfur as runoff.

7. Relevance to Mars

Comparison of Icelandic hydrothermal deposits to those inferred to exist on Mars is complicated by several factors. Mars basalt in the area explored by MER Spirit (Gusev crater) often approaches or exceeds 20 wt. % Fe_2O_3 and is lower in Al_2O_3 and CaO than Icelandic basalt (Figure 28). Although hydrothermal alteration products are only partially source-controlled, as discussed in Section 6.2.1, host rock composition affects the availability of elements in the system and in turn the chemical compositions of hot springs and the secondary minerals forming at the surface. However, markers of hydrothermal alteration are still relatively distinct, as sulfates, sulfides, phyllosilicates, npOx, silica-rich residue and sinter, and travertines are all common mineral deposits observed in hydrothermal systems on Earth despite variability in host lithology (Pirajno and van Kranendonk 2005; de Moor et al. 2016; Pirajno 2010, 2020).

Availability of water in a potential Martian hydrothermal system must also be considered. Iceland receives consistent precipitation and has plentiful meteoric water, hastening diagenetic phase transformation of minerals unstable at the surface (e.g. amorphous silica), or dissolving and removing them entirely (e.g. soluble sulfates). The relatively few sulfate/native sulfur deposits observed in our study area suggest that the dissolution and removal of soluble sulfur deposits may be common in Iceland. In contrast, the early Mars climate, though poorly constrained, would have most likely had much more limited water availability. This would slow or prevent diagenetic maturation and preserve soluble minerals.

Finally, differences between the modern Earth and the early Martian atmospheres could affect the mineral assemblage, at least at the surface/near-surface. For example, the 4 cm deep oxidation front observed in the Geysir fumarole reflecting the transition of pyrite (below the oxidation front) to npOx (above the oxidation front) is affected by the availability of atmospheric
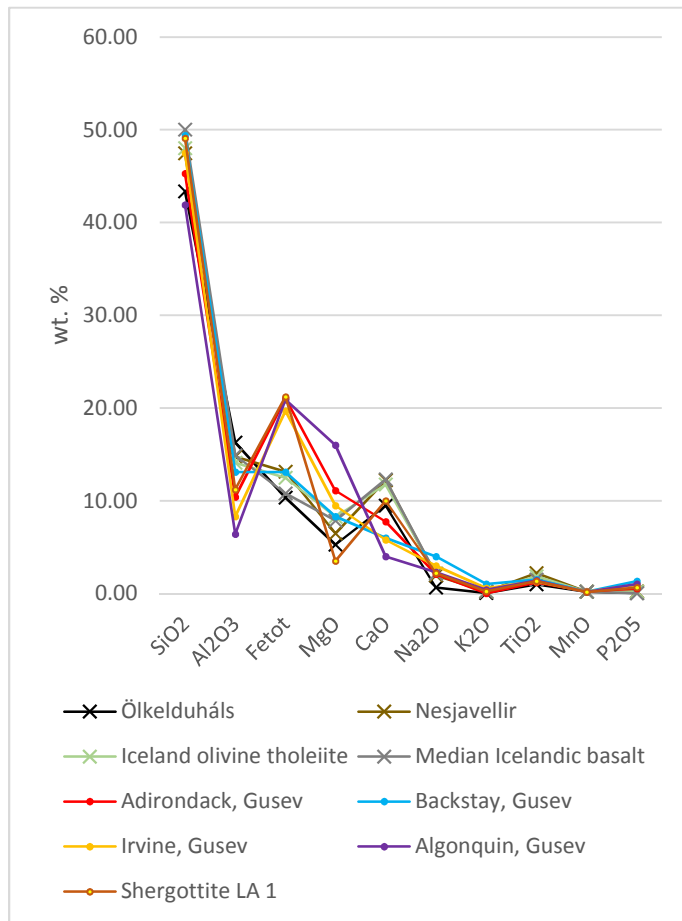
Figure 28: Comparison of major oxides in Icelandic basalts and basalt samples from Gusev crater, Mars, plus Mars meteorite Shergottite LA 1. Icelandic samples are given an X symbol, and are lower in Fe and Ca, and higher in Al than Mars basalt. Mars data from: McSween et al. (2009), Ming et al. (2008), Hurowitz et al. (2006).

O_2. Additionally, deposition of native sulfur at the fumarole vent is controlled by partial oxidation of magmatic volatiles, and the formation of steam-heated acid sulfate springs occurs from the mixing and oxidation of magmatic volatiles with oxygen-rich meteoric water. Limited O_2 in the early Martian atmosphere could result in more reducing conditions throughout a hydrothermal system, in turn preventing (or limiting) oxidation of volatiles at the near-surface (Niles et al. 2013; Kite and Melwani Daswani 2019). These climatic/atmospheric factors, though poorly constrained, would make the expression of hydrothermal processes on Mars distinct from those in Iceland.

7.1 Hydrothermal deposits near Home Plate, Gusev crater

7.1.1 Paso Robles class soils

The case for acid-sulfate hydrothermal alteration is evident in multiple locations surrounding Home Plate and the nearby Columbia Hills region explored by Spirit. The class of sulfate-rich soils known as Paso Robles revealed by Spirit's broken wheel are highly consistent with fumarolic or acid fluid alteration at low water/rock ratios. This is indicated by the presence

of an undetermined mineral assemblage consisting of ferric Fe-sulfates at ~25-29% abundance, with additional Mg-, Ca-, Na- K-, Al-, Mn-, Ni-, and Zn-sulfates also present in some samples, along with minor phosphates and amorphous silica (Ming et al. 2006; Yen et al. 2008). The patchy distribution of Paso Robles soils, which does not correspond to any particular stratigraphic position near Home Plate, also supports discrete alteration, possibly through fumarolic wall rock leaching. Sulfates were relatively uncommon alteration products in our samples, only occurring as major phases in seven samples across all field sites (Table 4). Of those samples, Fe-, Mg-, Al-, and Ca-sulfates were all most common, and they often occurred in areas with apparently limited water availability (e.g. on slopes or rocks several meters away from any surface fluid source). Although the mineral composition of Paso Robles soils is relatively unconstrained, the geochemical similarity and discrete distribution of sulfates observed in this study are a good match to such deposits on the Martian surface, and we favor the interpretation that Paso Robles soils formed through similar processes. Near active thermal features, amorphous silica, phyllosilicates, likely npOx, and pyrite dominated the alteration assemblage. The relative rarity of sulfates in our samples is likely related to the high availability of water in Iceland, where rainfall would cause rapid dissolution of the highly soluble sulfate minerals, leaving behind residual Fe-oxide crusts or patches of altered, clay- and silica-rich soil. Other sites in Iceland (e.g. Namafjall, Carson 2015) have more abundant sulfate minerals, perhaps tied to a higher flux of fumarolic gases that can replenish and maintain ephemeral surface sulfate precipitates. Additionally, the abundance of pyrite at the surface and near-subsurface of steam-heated areas indicates that reducing conditions are prevalent at shallow depths throughout the areas sampled. This limits the control of atmospheric O_2 on the secondary minerals forming and may provide another reason for the relative lack of sulfate minerals in our samples.

7.1.2 Maturity of the inferred Home Plate hydrothermal system

Indicators of hydrothermal processes near Home Plate, Gusev crater are widespread, as discussed in this study and in numerous publications (e.g. Yen et al. 2008; Morris et al. 2008, 2010; Schmidt et al. 2008, 2009; Ruff et al. 2011, 2020; Carson 2015; Rodríguez and van Bergen 2015; Ruff and Farmer 2016; McHenry et al. 2017 *and many others*). The emerging view put forward by Ruff et al. (2020) favors diverse aqueous processes in the area surrounding Home Plate: fumarolic alteration at low water/rock ratios that produced sulfates and leached residues, near-neutral to alkaline hot spring fluids that precipitated silica sinters, and possible post-depositional fumarolic modification of silica sinter outcrops leading to the deposition of additional sulfur and dissolution and reprecipitation of silica (forming pitted, sponge-like textures in some of the proposed sinters as seen in Figure 1D). However, left unconstrained is the length of time hydrothermal processes near Home Plate, or elsewhere on the Martian surface, may have been active. This investigation studied Icelandic hydrothermal systems with upper limits of hydrothermal activity ranging from 400 – 800 k.yrs. (based on the age of volcanic units near Hengill and Geysir, respectively; Demissie 2005; Gebrehiwot 2005; Natukunda 2005; Jones et al. 2007). At our sites, we observed mixtures of kaolinite/smectite, mixtures of amorphous silica and quartz, and aerially extensive swaths of altered ground/cliff faces, all implying long-term alteration and substantial diagenetic maturation. These ages, then, also provide a maximum length of time to produce the degree of diagenetic maturation observed. However, individual surface manifestations of hydrothermal activity are somewhat ephemeral, and it is unlikely that any modern surface feature has survived several hundred thousand years.

Although the age of any of the studied surface features is unconstrained, the upper succession of siliceous sinter deposits at Geysir has been dated to a maximum of 10 ka (Jones et

al. 2007; Geilert et al. 2016), even if the geothermal system itself has been active for ~ 800,000

years. At Geysir, this resulted in the accumulation of 2 – 2.5 m thick layered sinter

deposits (Jones et al. 2007), at an approximate rate of 0.025 cm yr^{-1} for sinter deposition. At

Ölkelduháls, the oldest mapped surface feature in the area is dated to a maximum of 130 ka, and

the features we sampled crosscut basaltic hyaloclastites as young as 12,000 years old (Natukunda

2005). Therefore, our results imply that high-intensity hydrothermal activity can produce

extensively altered, diagenetically mature hydrothermal deposits (including quartz replacement

of amorphous silica), whether through acid-sulfate (e.g. Ölkelduháls) or near-neutral/alkaline

(e.g. Geysir) hydrothermal processes, on relatively short timescales.

Comparing the secondary minerals observed herein to those observed on the Martian

surface by MER Spirit suggests that the inferred hydrothermal system near Home Plate was

short-lived. Spirit observed abundant sulfates (Paso Robles class soils), opaline silica (in the

Eastern Valley adjacent to Home Plate itself; Figure 1A), and minimal evidence of

phyllosilicates (Arvidson et al. 2008; Ming et al. 2008; Yen et al. 2008; Ruff et al. 2011). As

described in Section 7.1.1 and proposed in Yen (2008), the sulfate-rich Paso Robles class soils

likely formed through precipitation from acidic fumarolic vapors/soil solutions with limited

water availability. The long-term preservation of such phases also supports minimal post-

depositional interaction with fluids, as sulfates are generally soluble and would quickly re-

dissolve. Ruff et al. (2020) make a convincing case that the nodular silica outcrops observed near

Home Plate were originally precipitated as silica sinter, and were altered by fumarolic vapors as

the water table declined some time later. However, experimental studies of the diagenetic phase

transformations that occur in terrestrial silica sinters subjected to this process imply that the

transition from amorphous silica to quartz can begin after only weeks of contact with fumarolic

vapors (Lynne et al. 2006, 2008, 2017). Although conditions of modern-day Earth and Noachian Mars are likely much different (leading to ambiguity when discussing the rate at which diagenesis would occur on early Mars), these observations suggest that the inferred Martian silica sinters must not have been exposed to fumarolic vapors for any appreciable length of time. The apparent lack of diagenetic maturity across all deposits near Home Plate is therefore most consistent with highly ephemeral hydrothermal activity, an observation that also has implications for the habitability of the inferred hydrothermal system as a whole.

8. Conclusions

The primary goal of this work was to better understand the formation of secondary minerals in hydrothermal systems in Iceland by integrated investigation of bulk solids and fluids. Hydrothermal systems represent high-priority targets in the search for biosignatures on the Martian surface, and differentiating surface environments long after the fluids that produced them have disappeared relies on investigations of modern-day hydrothermal systems and their comparison to available Mars rover data.

The analyses of hydrothermal alteration products and fluids presented in this research reveal distinct trends associated with fluid pH, water/rock ratio, hydrothermal system maturity, host lithology, and redox conditions. The findings are summarized below:

- The mineral phases observed associated with hot springs and fumaroles across the study area reflect interaction of hydrothermal fluids/volatiles with substrate that has undergone extensive alteration. Abundant pyrite indicated mobilization of iron from host rocks and subsequent interaction with magmatic volatiles in highly reducing near-surface environments.

- Phyllosilicates were pervasive across diverse environments with wide ranges of pH and apparent water/rock ratio, and included smectite and kaolinite. The presence of smectite associated with low pH hot springs suggests that the presence of smectite does not preclude acidic conditions.

- Sulfate minerals were relatively rare, and were only observed in areas where water availability was limited, consistent with their generally high solubility. The sulfates observed appeared to form through evaporation of acidic soil solutions where atmospheric O_2 oxidized magmatic volatiles or soil solutions, generating sulfuric acid that leached metals from the near surface and precipitated sulfates upon evaporation. Alternatively, pyrite oxidation may have also contributed to the formation of sulfates.

- Concentrations of Mg, Fe, Al, Ca, Mn, Cr, Ni, Ti, V, and Zr followed downward exponential trends with respect to their concentration in waters with pH $> \sim 3$, consistent with their reduced mobility under moderately acidic conditions. Cl, K, Na, Ge, Ga, B, As, and Rb concentrations followed the opposite trend and were associated with boiled alkaline hydrothermal fluids, indicating their high mobility and deep aquifer fluid source.

- Patterns of enrichment and depletion in altered rocks indicate that TiO_2 and Zr follow a nearly linear trend of accumulation when subjected to acidic fluids, consistent with their low solubility. This relationship provides a means to compare the relative mobility of other elements in altered rocks.

- The incorporation of trace metals into hydrothermal alteration products appeared significantly more source-controlled than major oxides. However, bulk geochemical and mineralogical analyses do not provide high enough resolution for detailed interpretation of

the behavior of trace elements in solids, especially sulfates. Understanding their behavior more completely requires further study.

- The fumarole investigated at Geysir was clay-dominated (rather than silica or sulfate-rich), unlike other, more acidic fumaroles studied previously, except for a zone of leaching directly adjacent to the vent. Ubiquitous pyrite in the near-subsurface of the fumarole mound suggests reducing conditions throughout. At the surface, pyrite oxidation led to the formation of likely npOx.

- The discrete occurrences of sulfates observed in this study are a good match for the sulfate-rich Paso Robles class soils observed by MER Spirit near Home Plate, Mars. Our results are consistent with previous studies of Paso Robles class soils that indicate that they were formed through acid-sulfate alteration at very limited water/rock ratios.

- At Ölkelduháls we observed extensive surface alteration and quartz authigenesis, and thick deposits of sinter were observed at Geysir. Both surface manifestations may be as young as a few thousand years. The advanced alteration and diagenetic maturity observed across the surface features studied underscores the efficiency with which hydrothermal processes can modify host rocks. These observations imply that the hydrothermal systems inferred to have existed on the Martian surface, such as those near Home Plate, Gusev crater, may have been ephemeral, as they did not develop these features associated with mature hydrothermal systems.

References

Allwood, A., Clark, B., Flannery, D., Hurowitz, J., Wade, L., Elam, T., Foote, M., and Knowles, E. (2015) Texture-specific elemental analysis of rocks and soils with PIXL: The Planetary Instrument for X-ray Lithochemistry on Mars 2020. IEEE Aerospace Conference Proceedings, 2015-June, 1–13.

Ármannsson, H. (2016) The fluid geochemistry of Icelandic high temperature geothermal areas. Applied Geochemistry, 66, 14–64.

Arnason, B., Theodorsson, P., Björnsson, S., and Saemundsson, K. (1969) Hengill, a high temperature thermal area in Iceland. Bulletin Volcanologique, 33, 245–259.

Arnórsson, S. (1975) Application of the Silica Geothermometer in Low Temperature Hydrothermal Areas in Iceland. American Journal of Science.

Arnórsson, S (1984) Germanium in Icelandic geothermal systems. Geochimica et Cosmochimica Acta, 48, 2489–2502.

Arnórsson, S (1995a) Geothermal systems in Iceland: Structure and conceptual models—I. High-temperature areas. Geothermics, 24, 561–602.

Arnórsson, S (1995b) Geothermal systems in Iceland: Structure and conceptual models—II. Low-temperature areas. Geothermics, 24, 603–629.

Arnórsson, S., Gronvold, K., Sigurdsson, S., Arnórsson, S., Grönvold, K., and Sigurdsson, S. (1978) Aquifer chemistry of four high-temperature geothermal systems in Iceland. Geochimica et Cosmochimica Acta, 42, 523–536.

Arnórsson, S., Sigurdsson, S., and Svavarsson, H. (1982) The chemistry of geothermal waters in Iceland. I. Calculation of aqueous speciation from 0 to 370C. Geochimica et Cosmochimica Acta, 46, 1513–1532.

Arnórsson, S., Ivarsson, G., Cuff, K., and Saemundsson, K. (1987) Geothermal activity in the Torfajokull Field, south Iceland; summary of geochemical studies. Jkull, 37, 1–12.

Arnórsson, S., Andresdottir, A., Arnórsson, S., and Andrésdóttir, A. (1995) Processes controlling the distribution of boron and chlorine in natural waters in Iceland. Geochimica et Cosmochimica Acta, 59, 4125–4146.

Arnórsson, S., Bjarnason, J.Ö., Giroud, N., Gunnarsson, I., and Stefánsson, A. (2006) Sampling and analysis of geothermal fluids. Geofluids, 6, 203–216.

Beblo, M., and Bjornsson, A. (1980) A model of electrical resistivity beneath NE- Iceland: correlation with temperature. Journal of Geophysics, 47, 184–190.

Berger, G., and Velde, B. (1992) Chemical parameters controlling the propylitic and argillic alteration process. European Journal of Mineralogy, 4, 1439–1456.

Berger, J.A., Schmidt, M.E., Gellert, R., Boyd, N.I., Desouza, E.D., Flemming, R.L., Izawa, M.R.M., Ming, D.W., Perrett, G.M., Rampe, E.B., and others (2017) Zinc and germanium in the sedimentary rocks of Gale Crater on Mars indicate hydrothermal enrichment followed

by diagenetic fractionation. Journal of Geophysical Research: Planets, 122, 1747–1772.

Bishop, J.L., Loizeau, D., McKeown, N.K., Saper, L., Dyar, M.D., Des Marais, D.J., Parente, M., and Murchie, S.L. (2013) What the ancient phyllosilicates at Mawrth Vallis can tell us about possible habitability on early Mars. Planetary and Space Science, 86, 130–149.

Björke, J.K., Stefánsson, A., and Arnórsson, S. (2015) Surface water chemistry at Torfajökull, Iceland-Quantification of boiling, mixing, oxidation and water-rock interaction and reconstruction of reservoir fluid composition. Geothermics, 58, 75–86.

Black, Sarah R (2018) Identification and Characterization of Martian Acid-Sulfate Hydrothermal Alteration : An Investigation of Instrumentation Techniques and Geochemical Processes Through Laboratory Experiments and Terrestrial Analog Studies. Thesis. Colorado University Boulder.

Black, S.R., and Hynek, B.M. (2018) Characterization of terrestrial hydrothermal alteration products with Mars analog instrumentation: Implications for current and future rover investigations. Icarus, 307, 235–259.

Bloise, A.; Kusiorowski, R.; Lassinantti Gualtieri, M.; Gualtieri, A.F. Thermal behaviour of mineralfibers. InMineral Fibers: Crystal Chemistry, Chemical-Physical Properties, Biological Interaction and Toxicity;Gualtier, A.F., Ed.; European Mineralogical Union: London, UK, 2017; Volume 18, pp. 215–252.

Byers, H.L., McHenry, L.J., and Grundl, T.J. (2016) Forty-Nine Major and Trace Element Concentrations Measured in Soil Reference Materials NIST SRM 2586, 2587, 2709a, 2710a and 2711a Using ICP-MS and Wavelength Dispersive-XRF. Geostandards and Geoanalytical Research, 40, 433–445.

Carson, G.L. (2015) Hydrothermal acid-sulfate alteration at Krafla and Namafjall, NE Iceland: Implications for Gusev Crater and Meridiani Planum, Mars. Thesis. University of Wisconsin - Milwaukee.

Cockell, C.S., Harrison, J.P., Stevens, A.H., Payler, S.J., Hughes, S.S., Kobs Nawotniak, S.E., Brady, A.L., Elphic, R.C., Haberle, C.W., Sehlke, A., and others (2019) A Low-Diversity Microbiota Inhabits Extreme Terrestrial Basaltic Terrains and Their Fumaroles: Implications for the Exploration of Mars. Astrobiology, 19, 284–299.

Craddock, R.A., and Howard, A.D. (2002) The case for rainfall on a warm, wet early Mars. Journal of Geophysical Research E: Planets, 107, 21-1-21–36.

DesMarais, D.J. (1996) Stable light isotope biogeochemistry of hydrothermal systems. In Evolution of Hydrothermal Eco pp. 83–98.

Djokic, T., Van Kranendonk, M.J., Campbel, K.A., Walter, M.R., and Ward, C.R. (2017) Earliest signs of life on land preserved in ca. 3.5 Ga hot spring deposits. Nature Communications, 8, 1–8.

Ehlmann, B.L., and Edwards, C.S. (2014) Mineralogy of the Martian Surface. Annual Review of Earth and Planetary Sciences, 42, 291–315.

Einarsson, P. (2008) Plate boundaries, rifts and transforms in Iceland. Jokull, 58, 35–58.

Evans, M.J., and Derry, L.A. (2002) Quartz control of high germanium/silicon ratios in geothermal waters. Geology, 30, 1019–1022.

Ewers, G.R., and Keays, R.R. (1977) Volatile and precious metal zoning in the Broadlands geothermal field, New Zealand. Economic Geology, 72, 1337–1354.

Farrand, W.H., Glotch, T.D., and Horgan, B. (2014) Detection of copiapite in the northern Mawrth Vallis region of Mars: Evidence of acid sulfate alteration. Icarus, 241, 346–357.

Fassett, C.I., and Head, J.W. (2008) Valley network-fed, open-basin lakes on Mars: Distribution and implications for Noachian surface and subsurface hydrology. Icarus, 198, 37–56.

Flahaut, J., Bishop, J.L.J.L., Silvestro, S., Tedesco, D., Daniel, I., and Loizeau, D. (2019) The Italian Solfatara as an analog for Mars fumarolic alteration. American Mineralogist, 104, 1565–1577.

Fontboté, L., Kouzmanov, K., Chiaradia, M., and Pokrovski, G.S. (2017) Sulfide minerals in hydrothermal deposits. Elements, 13, 97–103.

Gangidine, A., Havig, J.R., Fike, D.A., Jones, C., Hamilton, T.L., and Czaja, A.D. (2019) Trace Element Concentrations in Hydrothermal Silica Deposits as a Potential Biosignature. Astrobiology, 20.

Gangidine, A., Havig, J.R., Hannon, S., and Czaja, A.D. (2020) Silica Precipitation in a Wet – Dry Cycling Hot Spring Simulation Chamber. Life, 10.

Gebrehiwot, K. (2005) Geothermal mapping in western Ölkelduháls field, Hengill area, SW-Iceland, 61–82 p.

Geilert, S., Vroon, P.Z., and van Bergen, M.J. (2016) Effect of diagenetic phase transformation on the silicon isotope composition of opaline sinter deposits of Geysir, Iceland. Chemical Geology, 433, 57–67.

George, L.L., Cook, N.J., and Ciobanu, C.L. (2016) Partitioning of trace elements in co-crystallized sphalerite-galena-chalcopyrite hydrothermal ores. Ore Geology Reviews, 77, 97–116.

Geptner, A.R., Ivanovskaya, T.A., Pokrovskaya, E. V., Lyapunov, S.M., Savichev, A.T., Gorbunov, A. V., and Gor'kova, N. V. (2007) Hydrothermally altered hyaloclastites at the Earth's surface in the rift zone of Iceland: Problem of the biochemogenic accumulation of trace elements. Lithology and Mineral Resources, 42, 453–476.

Glenister, C. (2018). THE GEOCHEMISTRY AND MINERALOGY OF SURFACE HYDROTHERMAL ALTERATION AT NESJAVELLIR, SW ICELAND. Thesis. University of Wisconsin - Milwaukee.

Goudge, T.A., Mustard, J.F., Head, J.W., Fassett, C.I., and Wiseman, S.M. (2015) Assessing the mineralogy of the watershed and fan deposits of the Jezero crater paleolake system, Mars. Journal of Geophysical Research: Planets, 120, 775–808.

Goudge, T.A., Fassett, C.I., Head, J.W., Mustard, J.F., and Aureli, K.L. (2016) Insights into surface runoff on early Mars from paleolake basin morphology and stratigraphy. Geology, 44, 419–422.

Goudge, T.A., Milliken, R.E., Head, J.W., Mustard, J.F., and Fassett, C.I. (2017) Sedimentological evidence for a deltaic origin of the western fan deposit in Jezero crater, Mars and implications for future exploration. Earth and Planetary Science Letters, 458, 357–365.

Grotzinger, J.P., Gupta, S., Malin, M.C., Rubin, D.M., Schieber, J., Siebach, K., Sumner, D.Y., Stack, K.M., Vasavada, A.R., Arvidson, R.E., and others (2015) Deposition, exhumation, and paleoclimate of an ancient lake deposit, Gale crater, Mars. Science, 350, aac7575–aac7575.

Hardardóttir, V., Brown, K.L., Fridriksson, T., Hedenquist, J.W., Hannington, M.D., and Thorhallsson, S. (2009) Metals in deep liquid of the Reykjanes geothermal system, southwest Iceland: Implications for the composition of seafloorblack smoker fluids. Geology, 37, 1103–1106.

Heirweigh, C.M., Elam, W.T., Flannery, D.T., and Allwood, A.C. (2018) An empirical derivation of the x-ray optic transmission profile used in calibrating the Planetary Instrument for X-ray Lithochemistry (PIXL) for Mars 2020. Powder Diffraction, 33, 162–165.

Humphris, S.E., and Thompson, G. (1978) Trace element mobility during hydrothermal alteration of oceanic basalts. Geochimica et Cosmochimica Acta, 42, 127–136.

Hurowitz, J.A., McLennan, S.M., Lindsley, D.H., and Schoonen, M.A.A. (2005) Experimental epithermal alteration of synthetic Los Angeles meteorite: Implications for the origin of Martian soils and identification of hydrothermal sites on Mars. Journal of Geophysical Research E: Planets, 110, 1–22.

Hynek, B. (2016) The great climate paradox of ancient Mars. Geology, 44, 879–880.

Hynek, B., Beach, M., and Hoke, M. (2010) Updated global map of Martian valley networks and implications for climate and hydrologic processes. Journal of Geophysical Research, 115, 1–14.

Hynek, B.M., McCollom, T.M., Marcucci, E.C., Brugman, K., and Rogers, K.L. (2013) Assessment of environmental controls on acid-sulfate alteration at active volcanoes in Nicaragua: Applications to relic hydrothermal systems on Mars. Journal of Geophysical Research E: Planets, 118, 2083–2104.

Ingebritsen, S.E., Geiger, S., and Hurwitz, S. (2010) Numerical simulation of magmatic hydrothermal systems. Reviews of Geophysics, 48, 1–33.

Ingebritsen, S.E., Bergfeld, D., Clor, L.E., and Evans, W.C. (2016) The Lassen hydrothermal system. American Mineralogist, 101, 343–354.

Irwin, R.P., Maxwell, T.A., Howard, A.D., Craddock, R.A., and Leverington, D.W. (2002) A large paleolake basin at the head of Ma'adim Vallis, Mars. Science, 296, 2209–2212.

Jakobsson, S.P. (1972) Chemistry and distribution pattern of recent basaltic rocks in Iceland. Lithos, 5, 365–386.

Jercinovic, M.J., Keil, K., Smith, M.R., and Schmitt, R.A. (1990) Alteration of basaltic glasses from north-central British Columbia, Canada. Geochimica et Cosmochimica Acta, 54, 2679–2696.

Jones, B., and Renaut, R.W. (2003) Hot spring and geyser sinters: The integrated product of precipitation, replacement, and deposition. Canadian Journal of Earth Sciences, 40, 1549–1569.

Jones, B., Renaut, R.W., Torfason, H., and Owen, R.B. (2007) The geological history of Geysir, Iceland: A tephrochronological approach to the dating of sinter. Journal of the Geological Society, 164, 1241–1252.

Jorgensen, B.B. (1999) A Thiosulfate Shunt in the Sulfir Cycle of Marine Sediments. Science, 249, 152–154.

Jousset, P., Haberland, C., Bauer, K., and Arnason, K. (2011) Hengill geothermal volcanic complex (Iceland) characterized by integrated geophysical observations. Geothermics, 40, 1–24.

Kaasalainen, H., and Stefánsson, A. (2011) Sulfur speciation in natural hydrothermal waters, Iceland. Geochimica et Cosmochimica Acta, 75, 2777–2791.

Kaasalainen, H., and Stefánsson, A. (2012) The chemistry of trace elements in surface geothermal waters and steam, Iceland. Chemical Geology, 330–331, 60–85.

Kaasalainen, H., Stefánsson, A., Giroud, N., and Arnórsson, S. (2015) The geochemistry of trace elements in geothermal fluids, Iceland. Applied Geochemistry, 62, 207–223.

Kaasalainen, H., Stefánsson, A., and Druschel, G.K. (2017) Geochemistry and speciation of Fe(II) and Fe(III) in natural geothermal water, Iceland. Applied Geochemistry, 87, 146–157.

Kite, E.S., and Melwani Daswani, M. (2019) Geochemistry constrains global hydrology on Early Mars. Earth and Planetary Science Letters, 524, 115718.

Klimchouk, A. (1996) The dissolution and conversion of gypsum and anhydrite. International Journal of Speleology, 25, 21–36.

Libbey, R.B., and Williams-Jones, A.E. (2016) Relating sulfide mineral zonation and trace element chemistry to subsurface processes in the Reykjanes geothermal system, Iceland. Journal of Volcanology and Geothermal Research, 310, 225–241.

Liu, R., Wolfe, A.L., Dzombak, D.A., Stewart, B.W., and Capo, R.C. (2008) Comparison of dissolution under oxic acid drainage conditions for eight sedimentary and hydrothermal pyrite samples. Environmental Geology, 56, 171–182.

Lugaizi, I. (2011) Borehole geology and hydrothermal mineralisation of well HE-32 Hellisheidi geothermal field, SW- Iceland. United Nations University Geothermal Training Programme.

Lugolobi, F., Kurtz, A.C., and Derry, L.A. (2010) Germanium-silicon fractionation in a tropical, granitic weathering environment. Geochimica et Cosmochimica Acta, 74, 1294–1308.

Lynne, B.Y., Campbell, K.A., Perry, R.S., Browne, P.R.L., and Moore, J.N. (2006) Acceleration of sinter diagenesis in an active fumarole, Taupo volcanic zone, New Zealand. Geology, 34, 749–752.

Lynne, B.Y., Campbell K.A., Moore, J., and Browne, P.R.L. (2008) Origin and evolution of the Steamboat Springs siliceous sinter deposit, Nevada, U.S.A. Sedimentary Geology, 210, 111-131.

Lynne, B.Y., Smith, G.J., Heasler, H., Jaworowski, C., Smith, I.J., Foley, D., and Sahdarani, D. (2017) Post-depositional alteration of siliceous sinter near Old Faithful Geyser, Yellowstone National Park, USA. Transactions - Geothermal Resources Council, 41, 1193–1203.

Markússon, S.H., and Stefánsson, A. (2011) Geothermal surface alteration of basalts, Krysuvik Iceland-Alteration mineralogy, water chemistry and the effects of acid supply on the alteration process. Journal of Volcanology and Geothermal Research, 206, 46–59.

Marteinsson, V.T., Hauksdottir, S., Hobel, C.F., Kristmannsdottir, H., Hreggvidsson, G.O., Kristjansson, J., Hauksdóttir, S., Hobel, C.F., Kristmannsdóttir, H., Hreggvidsson, G.O., and others (2001) Phylogenetic diversity analysis of subterranean hot springs in Iceland. Applied and environmental microbiology, 67, 4242–4248.

Marty, B., Gunnlaugsson, E., Jambon, A., Oskarsson, N., Ozima, M., Pineau, F., and Torssander, P. (1991) Gas geochemistry of geothermal fluids, the Hengill area, southwest rift zone of Iceland. Chemical Geology, 91, 207–225.

McCanta, M.C., Dyar, M.D., and Treiman, A.H. (2014) Alteration of Hawaiian basalts under sulfur-rich conditions: Applications to understanding surface-atmosphere interactions on Mars and Venus. American Mineralogist, 99, 291–302.

McCollom, T.M., Hynek, B.M., Rogers, K., Moskowitz, B., and Berquó, T.S. (2013a) Chemical and mineralogical trends during acid-sulfate alteration of pyroclastic basalt at Cerro Negro volcano and implications for early Mars. Journal of Geophysical Research: Planets, 118, 1719–1751.

McCollom, T.M., Robbins, M., Moskowitz, B., Berquõ, T.S., Jöns, N., and Hynek, B.M. (2013b) Experimental study of acid-sulfate alteration of basalt and implications for sulfate deposits on Mars. Journal of Geophysical Research E: Planets, 118, 577–614.

McHenry, L.J., Carson, G.L., Dixon, D.T., and Vickery, C.L. (2017a) Secondary minerals associated with Lassen fumaroles and hot springs: Implications for martian hydrothermal deposits. American Mineralogist, 102, 1418–1434.

McHenry, L.J., Kodikara, G.R.L., Stanistreet, I.G., Stollhofen, H., Njau, J.K., Schick, K., and Toth, N. (2020) Lake conditions and detrital sources of Paleolake Olduvai, Tanzania, reconstructed using X-ray Diffraction analysis of cores. Palaeogeography, Palaeoclimatology, Palaeoecology, 556, 109855.

McMahon, S., Bosak, T., Grotzinger, J.P., Milliken, R.E., Summons, R.E., Daye, M., Newman, S.A., Fraeman, A., Williford, K.H., and Briggs, D.E.G. (2018) A Field Guide to Finding Fossils on Mars. Journal of Geophysical Research: Planets, 123, 1012–1040.

Ming, D.W., Mittlefehldt, D.W., Morris, R. V., Golden, D.C., Gellert, R., Yen, A., Clark, B.C., Squyres, S.W., Farrand, W.H., Ruff, S.W., and others (2006) Geochemical and mineralogical indicators for aqueous processes in the Columbia Hills of Gusev crater, Mars. Journal of Geophysical Research E: Planets, 111.

Morris, R. V., Klingelhofer, G., Schroer, C., Fleischer, I., Ming, D.W., Yen, A.S., Gellert, R., Arvidson, R.E., Rodionov, D.S., Crumpler, L.S., and others (2008) Iron mineralogy and aqueous alteration from Husband Hill through Home Plate at Gusev Crater, Mars: Results from the Mossbauer instrument on the Spirit Mars Exploration Rover. Journal of Geophysical Research E: Planets, 113.

Morris, R. V., Vaniman, D.T., Blake, D.F., Gellert, R., Chipera, S.J., Rampe, E.B., Ming, D.W., Morrison, S.M., Downs, R.T., Treiman, A.H., and others (2016) Silicic volcanism on Mars evidenced by tridymite in high-SiO$_2$ sedimentary rock at Gale crater. Proceedings of the National Academy of Sciences, 201607098.

Morris, R. V., Rampe, E.B., Vaniman, D.T., Christoffersen, R., Yen, A.S., Morrison, S.M., Ming, D.W., Achilles, C.N., Fraeman, A.A., Le, L., and others (2020) Hydrothermal Precipitation of Sanidine (Adularia) Having Full Al,Si Structural Disorder and Specular Hematite at Maunakea Volcano (Hawai'i) and at Gale Crater (Mars). Journal of Geophysical Research: Planets, 125, 1–22.

Mountain, B.W., Benning, L.G., and Boerema, J.A. (2003) Experimental studies on New Zealand hot spring sinters: Rates of growth and textural development. Canadian Journal of Earth Sciences, 40, 1643–1667.

Natukunda, J.F. (2005) Geothermal Exploration in Eastern Ölkelduháls Field , Hengill Area , Sw-Iceland, 247–264 p.

Niles, P.B., Catling, D.C., Berger, G., Chassefière, E., Ehlmann, B.L., Michalski, J.R., Morris, R., Ruff, S.W., and Sutter, B. (2013) Geochemistry of carbonates on Mars: Implications for climate history and nature of aqueous environments. Space Science Reviews, 174, 301–328.

Nono, F., Gibert, B., Parat, F., Loggia, D., Cichy, S.B., and Violay, M. (2018) Electrical conductivity of Icelandic deep geothermal reservoirs up to supercritical conditions: Insight from laboratory experiments. Journal of Volcanology and Geothermal Research.

Parkhurst, D.L., Appelo, C.A.J., 1999. User's guide to PHREEQC (Version 2)—a computer program for speciation, batch-reaction, one-dimensional transport, and inverse geochemical calculations. U.S. Geological Survey Water-Resources Investigations Report, pp. 99–4259. 310 pp.

Papike, J.J., Keith, T.E.C., Spilde, M.N., Galbreath, K.C., Shearer, C.K., and Laul, J.C. (1991) Geochemistry and mineralogy of fumarolic deposits, Valley of Ten Thousand Smokes, Alaska: Bulk chemical and mineralogical evolution of dacite-rich protolith. American Mineralogist, 76, 1662–1673.

Pirajno, F. (2010) Hydrothermal processes and mineral systems. Springer.

Pirajno, F. (2020) Subaerial hot springs and near-surface hydrothermal mineral systems past and present, and possible extraterrestrial analogues. Geoscience Frontiers.

Rice, M.S., Gupta, S., Treiman, A.H., Stack, K.M., Calef, F., Siebach, K.L., Vasavada, A., Wiens, R.C., and Williams, J. (2016) Geologic overview of the Mars Science Laboratory rover mission at the Kimberley, Gale crater, Mars. Journal of Geophysical Research: Planets, 122, 2–20.

Robbins, S.J., Di Achille, G., and Hynek, B.M. (2011) The volcanic history of Mars: High-resolution crater-based studies of the calderas of 20 volcanoes. Icarus, 211, 1179–1203.

Robinson, C. (2000) THE ROLE OF JAROSITE AND COPIAPITE IN THE CHEMICAL EVOLUTION OF ACID DRAINAGE WATERS, RICHMOND MINE, IRON MOUNTAIN, CALIFORNIA. Thesis. Queen's University.

Rodríguez, A., and van Bergen, M.J. (2015) Volcanic hydrothermal systems as potential analogues of Martian sulphate-rich terrains. Netherlands Journal of Geosciences, 2015, 1–17.

Rubin, J.N., Henry, C.D., and Price, J.G. (1993) The mobility of zirconium and other "immobile" elements during hydrothermal alteration. Chemical Geology, 110, 29–47.

Ruff, S.W., and Farmer, J.D. (2016) Silica deposits on Mars with features resembling hot spring biosignatures at El Tatio in Chile. Nature Communications, 7, 1–10.

Ruff, S.W., Farmer, J.D., Calvin, W.M., Herkenhoff, K.E., Johnson, J.R., Morris, R. V., Rice, M.S., Arvidson, R.E., Bell, J.F., Christensen, P.R., and others (2011) Characteristics, distribution, origin, and significance of opaline silica observed by the Spirit rover in Gusev crater, Mars. Journal of Geophysical Research E: Planets, 116.

Rutledge, A.M., Horgan, B.H.N., Havig, J.R., Rampe, E.B., Scudder, N.A., and Hamilton, T.L. (2018) Silica Dissolution and Precipitation in Glaciated Volcanic Environments and Implications for Mars. Geophysical Research Letters, 45, 7371–7381.

Schinteie, R., Campbell, K.A., and Browne, P.R.L. (2007) Microfacies of stromatolitic sinter from acid-sulphate-chloride springs at Parariki Stream, Rotokawa Geothermal Field, New Zealand. Palaeontologia Electronica, 10, 1–33.

Schulze-Makuch, D., Dohm, J.M., Fan, C., Fair??n, A.G., Rodriguez, J.A.P., Baker, V.R., and Fink, W. (2007) Exploration of hydrothermal targets on Mars. Icarus, 189, 308–324.

Scott, S., Gunnarsson, I., Arnórsson, S., and Stefánsson, A. (2014) Gas chemistry, boiling and phase segregation in a geothermal system, Hellisheidi, Iceland. Geochimica et Cosmochimica Acta, 124, 170–189.

Singh, P., Sarkar, R., and Porwal, A. (2019) Orbital remote sensing of impact-induced hydrothermal systems on Mars. Ore Geology Reviews, 108, 101–111.

Skok, J.R., Mustard, J.F., Ehlmann, B.L., Milliken, R.E., and Murchie, S.L. (2010) Silica deposits in the Nili Patera caldera on the Syrtis Major volcanic complex on Mars. Nature Geoscience, 3, 838–841.

Smith, S.J., Stevens, R., Liu, S., Li, G., Navrotsky, A., Boerio-Goates, J., and Woodfield, B.F. (2009) Heat capacities and thermodynamic functions of TiO2 anatase and rutile: Analysis of phase stability. American Mineralogist, 94, 236–243.

Squyres, S., Deblinger, R.D., Wickham, J.D., Alexander, L.E., Belnap, J., Martin, J.R., Wright, R.G., Methods, L.S., Marching, F., Mechanics, F., and others (2007) Pyroclastic Activity at Home Plate in Gusev Crater, Mars. Science, 316, 738–742.

Squyres, S.W., Arvidson, R.E., Ruff, S.W., Farmer, J.D., Morris, R.V., Lieber, C.M., Wang, Z.L., Morales, A.M., Lieber, C.M., Wagner, R.S., and others (2008) Detection of Silica-Rich Deposits on Mars. Science, 320, 1063–1067.

Stefánsson, A. (2017) Gas chemistry of Icelandic thermal fluids. Journal of Volcanology and Geothermal Research, 346, 81–94.

Stefánsson, A., Arnórsson, S., and Sveinbjornsdottir, A. (2005) Redox reactions and potentials in natural waters at disequilibrium. Chemical Geology, 221, 289–311.

Stefánsson, A., Keller, N.S., Robin, J.G., Kaasalainen, H., Björnsdóttir, S., Pétursdóttir, S., Jóhannesson, H., and Hreggvidsson, G.Ó. (2016) Quantifying mixing, boiling, degassing, oxidation and reactivity of thermal waters at Vonarskard, Iceland. Journal of Volcanology and Geothermal Research, 309, 53–62.

Stoiber, R.E., and Rose, W.I. (1974) Fumarole incrustations at active central american volcanoes. Geochimica et Cosmochimica Acta, 38, 495–516.

Strumm, W. and Morgan, J. (1995) Aquatic Chemistry: Chemical Equilibria and Rates in Natural Waters, 3rd Edition. Wiley & Sons.

Tabelin, C.B., Igarashi, T., Tamoto, S., and Takahashi, R. (2012) The roles of pyrite and calcite in the mobilization of arsenic and lead from hydrothermally altered rocks excavated in Hokkaido, Japan. Journal of Geochemical Exploration, 119–120, 17–31.

Tobler, D.J., and Benning, L.G. (2011) Bacterial diversity in five Icelandic geothermal waters: Temperature and sinter growth rate effects. Extremophiles, 15, 473–485.

Tobler, D.J., Stefánsson, A., and Benning, L.G. (2008) In-situ grown silica sinters in Icelandic geothermal areas. Geobiology, 6, 481–502.

Todd, E.C., Sherman, D.M., and Purton, J.A. (2003) Surface oxidation of pyrite under ambient atmospheric and aqueous (pH = 2 to 10) conditions: electronic structure and mineralogy from X-ray absorption spectroscopy. Geochimica et Cosmochimica, 67, 881–893.

Tosca, N.J., McLennan, S.M., Lindsley, D.H., and Schoonen, M.A.A. (2004) Acid-sulfate weathering of synthetic Martian basalt: The acid fog model revisited. Journal of Geophysical Research E: Planets, 109.

Veneranda, M., Lopez-Reyes, G., Manrique, J.A., Medina, J., Ruiz-Galende, P., Torre-Fdez, I., Castro, K., Lantz, C., Poulet, F., Dypvik, H., and others (2020) ExoMars raman laser spectrometer: A tool for the potential recognition of wet-target craters on mars. Astrobiology, 20, 349–363.

Wanta, A. (2018) Hydrothermal Alteration at Devil's Kitchen in the Lassen Volcanic National Park: a Mars Analogue. Thesis. University of Wisconsin - Milwaukee.

Weitz, C.M., Bishop, J.L., Baker, L.L., and Berman, D.C. (2014) Fresh exposures of hydrous Fe-

bearing amorphous silicates on Mars. Geophysical Research Letters, 41, 8744–8751.

Wolfe, C.J., Bjarnason, I.T., VanDecar, J.C., and Solomon, S.C. (1997) Seismic structure of the Iceland mantle plume. Letters to Nature, 385, 245–247.

Wood, S.A., and Samson, I.M. (2006) The aqueous geochemistry of gallium, germanium, indium and scandium. Ore Geology Reviews, 28, 57–102.

Yang, S., Humayun, M., Righter, K., Jefferson, G., Fields, D., and Irving, A.J. (2015) Siderophile and chalcophile element abundances in shergottites: Implications for Martian core formation. Meteoritics and Planetary Science, 50, 691–714.

Yen, A.S., Morris, R. V., Clark, B.C., Gellert, R., Knudson, A.T., Squyres, S., Mittlefehldt, D.W., Ming, D.W., Arvidson, R., McCoy, T., and others (2008) Hydrothermal processes at Gusev Crater: An evaluation of Paso Robles class soils. Journal of Geophysical Research E: Planets, 113, 1–19.

Yen, A.S., Ming, D.W., Vaniman, D.T., Gellert, R., Blake, D.F., Morris, R. V., Morrison, S.M., Bristow, T.F., Chipera, S.J., Edgett, K.S., and others (2017) Multiple stages of aqueous alteration along fractures in mudstone and sandstone strata in Gale Crater, Mars. Earth and Planetary Science Letters, 471, 186–198.

Yen, A.S., Gellert, R., Morris, R. V., Ashley, J.W., Berger, J.A., Clark, B.C., Cohen, B.A., Ming, D.W., Mittlefehldt, D.W., O'Connell-Cooper, C.D., and others (2019) Understanding martian alteration processes by comparing in-situ chemical measurements from multiple landing sites. In Ninth International Conference on Mars 2019 [abstract 2089]. Pasadena, CA.

Zakharova, O.K., and Spichak, V. V. (2012) Geothermal fields of Hengill Volcano, Iceland. Journal of Volcanology and Seismology, 6, 1–14.

Appendix A
GPS coordinates of samples and brief descriptions

Table S1: Field photo references and GPS coordinates for each sample

Site	Sample	Field photo	Location	Description & associated water sample
Ölkelduháls	IO-19-5			dark-colored, subaqueous mud; associated with IO-19-21
	IO-19-6			surface crust; on margin of IO-19-21
	IO-19-7		N64.05716, W21.23689	altered soil; associated with IO-19-21
	IO-19-8	Figure 8		tan/orange precipitate; on margins of IO-19-21
	IO-19-9			crenulated surface crust; ~1 m from IO-19-21
	IO-19-10			buff/tan clay directly underlying IO-19-9
	IO-19-11			grey subaqueous mud; associated with IO-19-22
	IO-19-12			colorful beige sediment/mud; associated with IO-19-22
	IO-19-13	Not pictured	N64.05694, W21.23696	yellow surface crystals atop altered soil; in occasional contact with steam
	IO-19-14			euhedral trigonal quartz crystals protruding from altered soil
Nesjavellir	IN-19-2	Figure 9		surface crust coating altered boulders adjacent to IN-19-1
	IN-19-8	Figure 10A, B	N64.09724, W21.27439	light grey subaqueous mud; associated with IN-19-6
	IN-19-9			white surface crust on margins of IN-19-6
	IN-19-10	Figure 10C	N64.09724, W21.27439	dark-colored subaqueous mud; associated with IN-19-7
	IN-19-12	Figure 10D	N64.09717, W21.27465	dark-colored subaqueous mud; associated with IN-19-11
	IN-19-14			friable, altered boulder
	IN-19-15	Figure 10A	N64.09717, W21.27457	crenulated surface crust; in drainage between IN-19-6, IN-19-7, and IN-19-11
Geysir	IG-19-2	Figure 12A	N64.31091, W20.30212	sinter from margins of IG-19-1
	IG-19-4	Figure 12B	N64.31071, W20.30261	red-stained sinter from margins of IG-19-3
	IG-19-15	Not pictured	N64.31423, W20.29975	sinter associated with extinct hot spring
	IG-19-16	Figure 12C	N64.31349, W20.30163	sinter from margins of Blessi hot spring (IG-19-5)
	IG-19-7			fumarole - vent; yellow/brown altered dirt
	IG-19-8			fumarole - white/beige surface crust 20 cm from vent
	IG-19-9	Figure 12E	N64.31469, W20.29966	fumarole - light grey mud directly beneath IG-19-8
	IG-19-10			fumarole - dark grey mud 4 cm below IG-19-9
	IG-19-11			fumarole - dark red/maroon coating mixed with light grey mud; 90 cm from vent
	IG-19-12			fumarole - red soil with flecks of beige clay; 110 cm from vent
	IG-19-13	Figure 12D	N64.31465, W20.29968	white dendritic precipitate in steaming gully
	IG-19-14			Soft, wet, white precipitate in steaming gully

Appendix B
Analytical lower limits of detection

Table S2: Analytical lower limits of detection (LOD) for instruments used to determine geochemical composition of solids and fluids.

				Solids					

				Major oxides (XRF); PPM					
SiO$_2$	**TiO$_2$**	**Al$_2$O$_3$**	**Fe$_2$O$_3$**	**MnO**	**MgO**	**CaO**	**Na$_2$O**	**K$_2$O**	**P$_2$O$_5$**
142.5	214.7	84.7	167	137.5	104.4	21.2	169.9	14	63.6

				Minor/trace elements (XRF); PPM					
Ba	**Co**	**Cr**	**Ni**	**V**	**Zn**	**Zr**			
52.7	3.4	20.9	14	21.8	19.1	8.8			

Minor/trace elements (ICP-OES/ICP-MS); ng/L

Ti	**S**	**Ba**	**Co**	**Cr**	**Cu**	**Ge**	**Ni**	**V**	**Zn**	**Zr**
0.3058	24.8	0.0012	0.0008	0.0161	0.0117	0.0046	0.1656	0.0061	0.0848	0.0003

				Fluids					

ICP-MS (PPB)

Al	**As**	**B**	**Ba**	**Cr**	**Fe**	**Ga**	**Mn**	**Ni**	**Rb**	**Sr**
1.174	0.058	0.356	0.049	0.079	0.761	0.053	0.158	0.079	0.061	0.039

V	**Ge**	**Ti**
0.051	unknown	unknown